UNIVERSIDADE FEDERAL DO PARÁ
INSTITUTO DE CIÊNCIAS EXATAS E NATURAIS
PROGRAMA DE PÓS-GRADUAÇÃO EM FÍSICA

Probing black hole spacetimes through quasinormal modes, light rings and shadow images

Zeus Sales Moreira

Advisor: Prof. Dr. Carlos Alberto Ruivo Herdeiro

Belém-Pará

2025

Probing black hole spacetimes through quasinormal modes, light rings and shadow images

Zeus Sales Moreira

Thesis submitted to the Programa de Pós-Graduação em Física da Universidade Federal do Pará (PPGF-UFPA), in partial fulfillment of the requirements for the degree of Doctor in Physics.

Advisor: Prof. Dr. Carlos Alberto Ruivo Herdeiro

Examiners

Prof. Dr. Carlos Alberto Ruivo Herdeiro (Advisor - PPGF/UFPA)

Prof. Dr. Alberto Saa (External member - University of Campinas, Brazil)

Prof. Dr. Dario Nunez (External member - National University of Mexico, Mexico)

Prof. Dr. Eugen Radu (External member - Aveiro University, Portugal)

Prof. Dr. Gonzalo Jesus Olmo Alba (Internal member - PPGF/UFPA)

Belém-Pará

2025

"it is the glory of geometry that from those few principles,
brought from without, it is able to produce so many things."

Isaac Newton, Newton's Principia, 1687

Acknowledgments

The first time I entered university as a freshman had a great meaning to me. It marked the beginning of my dream to become a physicist. Right in the middle of the first semester, a university strike interrupted classes for over four months. It was during this pause that I grew closer to a group of guys, namely: João Paulo, Marco Aurélio, Mateus Malato, Renan Batalha, and Sérgio Vinícius, who just wanted to keep studying. During that time, we started a linear algebra study club, which, in many ways, never really ended. What began as simple discussions of proving whether certain spaces were vector spaces, soon evolved into debates on black hole calculations and intriguing papers just published on arXiv. I owe my deepest gratitude to this group. The growth, the exchange of ideas and the countless hours spent learning and having fun together were truly special. Without them, I would not be where I am today. Thank you all! Now, João, Renan, Marco, and Sérgio have already earned their doctorates. It is just me and Malato left, but we are catching up!

I am deeply grateful to my advisor, Carlos Alberto Ruivo Herdeiro, for his supervision and excellent guidance. The time I spent in Aveiro under his mentorship profoundly shaped me as a researcher. It is really remarkable how just 15 minutes in his office could illuminate ideas that might have taken me weeks (or even months) to figure out on my own. I would also like to express my gratitude to professor Luís Carlos Bassalo Crispino, for the insightful discussions in physics and for his personal and professional advice. Being part of Grav@Zon – Gravity @ Amazonia – the gravity research group at Universidade Federal do Pará (UFPA), is a privilege. Professor Crispino leadership continuously elevate the standards of our group, making it a place I am proud to be a part of.

In my first PhD project, I had the pleasure to work with professor Haroldo Cilas Duarte Lima Junior, a researcher that I really respect and a true friend. I am grateful for our collaboration and discussions. His contributions always makes me learn a lot.

I must thank the gravity group of Universidade de Aveiro (UA) for kindly welcoming me into their group activities during my stay in Portugal, and for the lasting friendships we formed. A special thank you to Etevaldo Costa, Ivo Sengo and Lorenzo Annulli. As I look back, I feel a big sense of nostalgia, also because of the amazing friendships I made outside the professional context. Ana, Fernanda, Gabi, Giselle, Bell, Paco, Tamara and Victoria,

and all the forró comunity of Aveiro, thank you so much for all the happy moments we shared.

I would also like to express my gratitude to my dear friends in Belém: 500, Gabriel, Gabrielly, Julia, Marco, Raquel, and Zé. A special thought also goes to João Marcelo and Marcos. Thank you for always being there for me and offering support throughout the years. A special thanks also goes to the friends and members of Cia. Cabanos, specially Lua. Cabanos is a place who helped me maintain both my physical and mental well-being after countless hours of hard work.

Pursuing a PhD in physics is an intense journey, filled with challenges, moments of doubt, and with several calculations that don't always add up. That's why having someone who stands by you, even when you question yourself, is so important. For that, I will be forever grateful to my girlfriend, Alice, for her kind support, patience, and love. You made my most difficult moments easier to bear. *Te amo tanto tanto tanto.*

I have a big source of professional inspiration right at home, namely my parents, Germana and Sanclayton. Both are professors at UFPA, and they each have such beautiful stories about how they reached where they are today. Both have a kind heart and have always shown great care for me. For their love, affection and inspiration, thank you, I am incredibly lucky to have you.

The research presented in this thesis has been made possible through the support of various sponsoring agencies, particularly the Conselho Nacional de Desenvolvimento Científico e Tecnológico (CNPq) and the Coordenação de Aperfeiçoamento de Pessoal de Nível Superior (CAPES).

Abstract

Probing black hole spacetimes through quasinormal modes, light rings and shadow images

Zeus Sales Moreira

Advisor: Prof. Dr. Carlos Alberto Ruivo Herdeiro

We begin by analyzing the quasinormal modes of a Schwarzschild black hole modified by Loop Quantum Gravity, which exhibits a regular global structure. We study massless scalar field perturbations in this quantum corrected spacetime and compute quasinormal modes using the three methods (WKB, Leaver, and Prony) to ensure consistency. We discuss patterns emerging from the overtone analysis and obtain the time profile of a scalar Gaussian wave packet. Next, we investigate a Schwarzschild black hole embedded in a rotating background, known as the swirling universe, which can be obtained through the Ernst formalism. We analyze the null geodesic flow, the existence of light rings, and shadows. Our findings reveal that the swirling background displaces the Schwarzschild black hole's light rings outside the equatorial plane, causing them to counter-rotate relative to each other while co-rotating with the swirling universe. Using backward ray-tracing, we obtain the black hole's shadow and lensing effects. Notably, for equatorial observers, the shadow exhibits an unusual $\mathbb{Z}_2$ (north-south) asymmetry, inherited from the background. Finally, we study a spinning generalization the Majumdar-Papapetrou multi-black hole spacetime. By analyzing the dynamics of null geodesics, we identify various light ring configurations, yielding cases with 4, 6, and 8 light rings. Using the backward ray-tracing method, we simulate images of this binary system, showing that its shadow closely resembles that of the double-Kerr metric.

Keywords: black holes, quasinormal modes, light-rings, shadows

Knowledge areas:1.05.01.03-7, 1.05.03.01-3.

Belém-Pará

2025

Resumo

Sondando espaços-tempos de buracos negros com modos quasinormais e sombras

Zeus Sales Moreira

Orientador: Prof. Dr. Carlos Alberto Ruivo Herdeiro

Começamos analisando os modos quasinormais de um buraco negro de Schwarzschild modificado pela Gravidade Quântica em Loop, que exibe uma estrutura global regular. Estudamos perturbações de campos escalares massivos nesse espaço-tempo corrigido quanticamente e calculamos os modos quasinormais utilizando três métodos (WKB, Leaver e Prony) para garantir a consistência. Discutimos padrões emergentes da análise de sobretons e obtemos o perfil temporal de um pacote de onda Gaussiano escalar. Em seguida, investigamos um buraco negro de Schwarzschild imerso em um fundo rotacional, conhecido como swirling universe, que pode ser obtido por meio do formalismo de Ernst. Analisamos o fluxo das geodésicas nulas, a existência de anéis de luz e as sombras. Nossos resultados revelam que o fundo rotacional desloca os anéis de luz do buraco negro de Schwarzschild para fora do plano equatorial, fazendo com que eles sejam contra-girantes entre si e co-girantes com o swirling universe. Utilizando o método de backward ray-tracing, obtemos a sombra do buraco negro e seus efeitos de lente gravitacional. Notavelmente, para observadores equatoriais, a sombra exibe uma incomum assimetria $\mathbb{Z}_2$ (norte-sul), herdada do espaço de fundo. Por fim, estudamos uma generalização girante do espaço-tempo de múltiplos buracos negros de Majumdar-Papapetrou. Ao analisar a dinâmica das geodésicas nulas, identificamos várias configurações de anéis de luz, resultando em casos com 4, 6 e 8 anéis. Usando o método de backward ray-tracing, simulamos imagens desse sistema binário, mostrando que sua sombra se assemelha fortemente à da métrica de double-Kerr.

Palavras-chave: buracos negros, modos quasinormais, anéis de luz, sombras

Áreas de Conhecimento: *1.05.01.03-7, 1.05.03.01-3.*

Belém-Pará

2025

To my parents

Contents

Part I

Introduction

Chapter 1

The path to General Relativity and black holes

1.1 Geometry: the language of space(time)

> "What can be said at all can be said clearly; and whereof one cannot speak thereof one must be silent."
>
> Ludwig Wittgenstein, Tractatus logico-philosophicus, 1921

This quote from Wittgenstein resonates deeply with the essence of theoretical physics. At its core, theoretical physics seeks to represent our understanding of the physical world through a precise and logically consistent formalism. To describe the natural world accurately, one must use a language that conveys its phenomena properly. Mathematics is that language, providing a universal and objective framework for expressing the fundamental laws of physics.

Geometry originated as a practical science for measuring distances and angles in ancient civilizations, serving various purposes, and gradually evolving into an abstract mathematical field—a language to talk about space. Euclid's Elements, a compilation of 13 books, represents one of the earliest axiomatic treatments of geometry, deriving a chain of propositions from five axioms[1]. While the first four postulates appeared self-evident, the fifth

[1] While Euclid's first four postulates lack full compatibility with modern mathematical axiomatizations,

postulate—often called the parallel postulate—stood out as less intuitive[2]. For centuries, mathematicians questioned whether it was truly fundamental or could be derived from the other axioms. These efforts, however, ultimately revealed the limitations of Euclidean geometry's universality and led to the discovery of entirely new geometries, later referred to by Gauss as non-Euclidean geometries.

The conceptualization of geometry has undergone profound transformations since Euclid's contributions. In the axiomatic structure of Euclidean and non-Euclidean geometries, the very notion of space is left undefined, with its characteristics emerging solely through the axioms. A major shift occurred with the study of curves and surfaces *embedded* is some particular pre-defined space (*e.g.*, $\mathbb{R}^2$ or $\mathbb{R}^3$). Newton, in his famous *The Method of Fluxions and Infinite Series*, was the first[3] to propose a definition of curvature[4] of curves on $\mathbb{R}^2$. Later, Gauss in his paper *General Investigations of Curved Surfaces*, applied this notion to define the intrinsic curvature[5] of surfaces embedded in $\mathbb{R}^3$.Furthermore, *Gauss's Theorema Egregium* demonstrated that this defined surface curvature is a geometric invariant, meaning it is determined entirely by the intrinsic metric properties [5].

Riemann took an important step toward the abstraction of the underlying space where geometry takes place. At the faculty of Göttingen University, he delivered his habilitation lecture titled *On the Hypotheses Which Lie at the Foundations of Geometry*, one of the most influential works in the entire history of differential geometry. Building on Gauss's ideas, Riemann introduced the concept of *manifolds*[6] as a n-dimensional generalization of smooth

they can be reformulated with greater precision, as demonstrated by Hilbert [1].

[2]In Playfair's axiom form, the fifth postulates reads: given a line l_0 and a point p not on it, there exists *exactly one* line l parallel to l_0 passing through the point p.

[3]The first published discussion of the curvature of a curve came from Huygens in 1673. In contrast, Newton's work on the subject, completed in 1671, remained unpublished during his lifetime and only appeared posthumously in 1736, several years after his death [2].

[4]The curvature of plane curves may be defined as the reciprocal of the radius of the osculating circle at that point [3]

[5]Given the curvatures of all plane curves on the surface passing through a given point, the *Gaussian curvature* is defined as the product of the maximum and minimum curvatures at that point [4]

[6]Although the formal notion of topological spaces, which is essential for a rigorous definition of manifolds, was developed later in the 19th century, Riemann's work anticipated many of these ideas while not addressing the full global nature of manifolds [2].

surfaces, endowed with its own intrinsically defined *metric*. This innovative framework allowed Riemann to generalize the Gauss curvature to higher dimensions through the *Riemann curvature tensor* [6]. His pioneering ideas were later expanded and formalized by Ricci, Levi-Civita, and Christoffel, who developed proper notions of tensors and connections [2, 7].

"Geometry and Experience" is a paper written by the german physicist Albert Einstein, based on a lecture he delivered at the Prussian Academy of Sciences in 1921 [8]. The work discusses the epistemological nature of geometry, exploring the relationship between mathematics and physical reality. Einstein highlights a fundamental question in this debate: Why does mathematics, a creation of human thought independent of experience, apply so effectively to reality? Einstein addresses this question with a very clever answer: *"As far as the laws of mathematics refer to reality, they are not certain; and as far as they are certain, they do not refer to reality"*.

According to Ref. [8], in classical geometry, axioms were seen as self-evident truths, derived from human intuition about space. Nevertheless, in modern axiomatic geometry, axioms are no longer considered self-evident, but rather arbitrary definitions. For example, consider the Euclidean axiom: *"Through two points, there is exactly one straight line"*. Traditionally, this statement was considered a simple fact about space, because we intuitively "know" what a "point" and a "straight line" are. However, in the modern axiomatic approach, the terms "point" and "straight line" have no inherent meaning outside the logical system defined by axioms. The Euclidean axiom serves as an implicit definition of "point" and "straight line". This shift in perspective, influenced by modern mathematical logic, helps clarify that mathematics, by itself, does not describe reality, until its content is associated with physical objects, *e.g.* solid bodies behave as objects in Euclidean geometry.

Hence, according to these ideas, all these elegant geometric constructions of manifolds with arbitrary dimensions, metric structures, connections and so on, are devoid of empirical value. Even so, motivated by the equivalence principle (which will be discussed in the next section), Einstein connected geometry with physical reality. Geometry rather than being merely a language of space, becomes the language of spacetime and forms the mathematical backbone of General Relativity (GR).

1.2 General Relativity

> "The equations are smarter than we are. Albert Einstein was pretty smart... but he never knew about black holes, he never fully understood gravitational waves, and he was always somewhat uncomfortable with the idea of the Big Bang. The equations just sat back smugly and said, 'You'll figure it out eventually.' "
>
> —Sean Carroll, *The Secrets of Einstein's Unknown Equation*, Royal Institution Lecture

Newton's *Philosophiae Naturalis Principia Mathematica* is widely regarded as one of the most important works in the history of science, laying the theoretical groundwork for classical mechanics. The preface to Principia reflects about the relation between mechanics and geometry, revealing the profound influence of earlier geometers on his ideas [9]. In fact, the concept of Euclidean space $\mathbb{E}^3$ (*i.e.* $\mathbb{R}^3$ equipped with the Euclidean distance $ds^2 = dx^2+dy^2+dz^2$) mathematically formalized his own idea of *absolute space*—a fixed, immutable background that neither influences the motion of matter nor is influenced by it. Alongside absolute space, Newton also postulated *absolute time*, a structure that defines an observer-independent notion of simultaneity[7]. Hence, in Newtonian mechanics, measurements of length and time intervals do not depend on the observer.

One of the greatest triumphs of Newtonian mechanics came with Newtonian gravity. This theory is governed by an elliptic equation. Hence, any change in the position of one mass is instantaneously reflected in the gravitational force experienced by another. For example, in the two-body problem, the gravitational force acting on each mass depends directly on the instantaneous position of the other.

While Newtonian mechanics is symmetric under the action of the Galilean group, electrodynamics is invariant under Lorentz transformations, a fundamental conflict related to the invariance of the speed of light. However, Einstein proposed modifying mechanics to

[7] The Newtonian concepts of space and time can made more precise in Newton-Cartan theory. See for instance [10]

accommodate the Lorentz group as its symmetry group, giving birth to his theory of Special Relativity (SR). The key to this theory is the relativity of simultaneity, which makes the invariance of the speed of light possible. As a result, measurements of length and time intervals are observer-dependent. SR can be elegantly formulated using Minkowski spacetime, a 4-dimensional manifold equipped with a flat metric. The Lorentz invariant interval between events ds in Minkowski spacetime, in rectangular coordinates $(x^\mu) = (t, x, y, z)$, reads[8]

$$ds^2 = \eta_{\mu\nu} dx^\mu dx^\nu = -dt^2 + dx^2 + dy^2 + dz^2, \tag{1.1}$$

where $\eta_{\mu\nu} = \text{diag}(-1, 1, 1, 1)$ are the components of the Minkowski metric. This interval is fundamentally different from the Euclidean distance, as it can take zero or negative values, even when the coordinate displacements are nonzero. In particular, lightlike, or null, worldlines are characterized by a vanishing spacetime interval, while timelike and spacelike intervals correspond to negative and positive values, respectively. Causally connected events are either lightlike or timelike separated, *i.e.* causal influences are constrained to travel at or below the speed of light.

Hence, Newtonian gravity is not compatible with SR, as was acknowledged by Poincaré in Ref. [11], who suggested that it should be modified to produce finite speed interactions (foreshadowing aspects of GR)[9]. Initially, even Einstein considered the possibility of modifying Newton's theory to align with SR [14]. A natural approach, then, is to explore field theories formulated within Minkowski spacetime. As a pedagogical exercise, Ref. [15] proposes some field theories using scalar, vector, and tensor potentials to model the gravitational field, but all three fail to provide a satisfactory description of gravity[10]. More solid field-theoretic formulations to gravity may be seen in Refs. [16–22].

Einstein adopted a radically different approach by relating gravitational universal features to the geometry of spacetime. A central component of this idea is the Weak Equivalence Principle (WEP), also known as the universality of the free-fall, which states that test particles, in a gravitational field, behave identically regardless of their internal properties. This

[8] In this thesis we will be mainly interested in 4-dimensional manifolds and we adopt the signature $(-,+,+,+)$. We also adopt units such that $c = G = 1$.

[9] The idea that gravity should be causally compatible with SR was also conjectured by Lorentz [12, 13].

[10] No bending of light in scalar and vector theories and wrong perihelion precession in all three models.

principle is reflected in Newtonian mechanics when one assumes that gravitational and inertial masses are equal. It implies that a gravitational field defines a set of preferred worldlines in spacetime, which can be understood as the autoparallel trajectories of a connection. In the absence of gravity, these worldlines reduce to straight-line motion in Minkowski spacetime, while in the presence of gravity, the connection becomes curved.

A stronger principle is the *(Einstein) Equivalence Principle (EEP)*: It is impossible to detect the existence of a gravitational field by means of local experiments. Thus, gravity is not a force like the others fundamental interactions, as it vanishes in certain reference frames, much like fictitious forces appear in non-inertial frames, but vanish in inertial ones. Since the gravitational field can disappear in certain frames, it must be described by a non-tensorial quantity, namely a connection (since a tensor that vanishes in one frame would vanish in all others), which is consistent with WEP. However, the EEP goes further, as Minkowski spacetime models physical phenomena in the absence of gravity, the EEP establishes that spacetime must have a local structure of a Minkowski spacetime. This principle, therefore, aligns well with the smooth manifold property of being locally Euclidean. As a result, this requirement imposes a metric structure $g_{\mu\nu}$ on spacetime, locally trivializable to the Minkowski metric. In the standard formulation of GR, the connection must be the Levi-Civita connection of the metric $g_{\mu\nu}$. This metric must be a solution of the Einstein field equations (EFE)

$$R_{\mu\nu} - \frac{1}{2} g_{\mu\nu} R = 8\pi T_{\mu\nu}, \tag{1.2}$$

where $R_{\mu\nu}$ is the Ricci tensor, R is the Ricci scalar, $g_{\mu\nu}$ is the spacetime metric and $T_{\mu\nu}$ is the energy-momentum tensor. The left-hand side of the equations describes geometric aspects of spacetime, while the right-hand side is related to the distribution of mass and energy. This implies that curvature influences the distribution and motion of matter in the universe, while matter, in turn, determines the geometry of spacetime, in stark contrast to Newtonian mechanics.

The EFE are nonlinear, 10 coupled partial differential equations for the metric. To obtain specific solutions, certain assumptions are necessary, such as imposing higher symmetries and constraining the matter fields. One of the most important classes of solutions of GR is the so-called black holes (BHs) (*e.g.* Schwarzschild [23], Reissner-Nordström (RN) [24, 25],

Kerr [26], Kerr-Newman [27, 28],...). By definition, BHs are regions in spacetime where the gravitational field is so intense that not even light can escape. Astronomical observations, such as the trajectories of stars showing strong deviations due to an extremely massive and compact object, provide evidence for the presence of a supermassive BH at the center of our galaxy [29].

1.3 Gravitational waves and black hole imaging

1.3.1 "Hearing" black holes

The mathematician Mark Kac in 1966 published a paper called "Can one hear the shape of a drum?" [30]. This problem aims to understand whether the eigenvalues of the Laplacian operator on a given two-dimensional boundary problem uniquely determine the boundary. In just one dimension with domain length l, this problem is trivial, since the eigenvalues λ_n are given by $\lambda_n = n^2\pi^2/l^2$, which can be solved for l. Carrying this idea into two dimensions greatly increases the difficulty of the problem. Nonetheless, Kac's question was answered in 1992 when mathematicians found two boundaries that produce identical eigenvalues [31], which physically means that a drum is not always uniquely identifiable by sound alone. However, later it was shown that if one restricts the boundary to be smooth and the domain to have some symmetries, Kac's question is answered positively [32–35].

Notably, there is a great mathematical similarity between the equations describing the ripples in a drum with perturbed BHs [36]. If we think of perturbed BHs as analogues of drums, then gravitational waves (GWs) must be the analogues of sound waves. Einstein was the first to use the *linearized GR* approximation to show that GWs are related with small perturbations $h_{\mu\nu}$ to the Minkowski metric $\eta_{\mu\nu}$, where the full metric is expressed as $g_{\mu\nu} = \eta_{\mu\nu} + h_{\mu\nu}, \quad |h_{\mu\nu}| \ll 1$ [13, 37]. However, for many decades there was no consensus if such waves could be indeed detected. In an interview on the Mindscape podcast, hosted by the physicist Sean Carroll, Kip Thorne discusses how the uncertainty surrounding the detectability of GWs was resolved [38]:

Sean Carroll: *"Wasn't there a famous thought experiment by Feynman that was trying to*

show that GWs were physically real?"

Kip Thorne: *"That's right. And so that's one of the compelling things, in which he said, 'Let's take a stick and we'll put some beads on the stick, and there's a little bit of friction between the beads and the stick. And when the GWs go by, they move the beads back and forth because they can slide. The stick is stiff and it resists being stretched and squeezed, so it doesn't move hardly at all, because of its resistance. The beads don't resist, so the beads go back and forth, and they rub on the stick, they heat the stick up. And if you have a strongly enough wave, they might even start a fire.' "*

Sean Carroll (laughs): *"I just loved that example for so many reasons. I mean, everyone else is sitting there with equations, trying to figure out what the symmetries are and what's going on, and he has this stick and beads."*

Kip Thorne: *"He's relying on a particular equation called the equation of geodesic deviation. So another physicist, a mathematical physicist, Felix Pirani, who first said 'Hey, this is the equation we should be using to discuss GWs'. So Feynman's remark about this was at a conference in Chapel Hill, north Carolina, 1956... or 7 (...). Anyway, Felix Pirani was almost that same time, just within a year or so."*

Any orbiting pair of astrophysical objects produces GWs, but only those sufficiently compact and moving very rapidly can produce detectable signals for the current generation of GWs detectors. This makes binary BH (BBH) ideal systems for detecting GWs. The collision of BHs can be divided in three stages: *(i) inspiral:* The BHs orbit around each other, getting closer due to loss of energy through GWs; *(ii) merger:* the actual collision of the two BHs and *(iii) ringdown:* The merged BH relaxes to its equilibrium form (widely believed to be a Kerr BH [26]). The GW signal produced by the binary carries a very characteristic signature [39–41], which in turn can reveal properties of the BH itself [42–44]. Identifying objects through their characteristic response to perturbations places BHs (and other compact objects) in a striking parallel with Kac's question about eigenvalues of the Laplace operator [45].

Various gravitational-wave detectors have been built and improved, culminating in the current generation of instruments that have reached a sensitivity where there GW signals may be measured. Recent breakthroughs in this area have been marked by several detections

of compact binary mergers, made by the LIGO/Virgo/KAGRA collaboration [46–48]. These observations provide crucial insights into the final moments before the coalescence of BBHs, as well as the properties of the resulting remnant.

In a perturbed physical system, the modes of vibration associated with energy dissipation are called quasinormal modes (QNMs). Thus, the ringdown phase of the coalescence of a BBH is essentially characterized by the corresponding QNMs [44, 49]. The BH QNMs program is fundamentally based on linearized pertubation of fields on a given BH spacetime. Due to the energy loss in the form of GWs through the event horizon and infinity, we lose the nice properties of self-adjoint problems, such as completeness and normalizability of the eigenfunctions and the spectrum becomes complex [50, 51]. The real part of the eigenfrequencies are the standard oscillation frequency, whereas the imaginary part is related to the wave damping.

The study of BH perturbations began with the work of Regge and Wheeler [36] and was further developed by Zerilli [52, 53]. The problem of finding the QNM frequencies was investigated for the first time in a famous paper written by Chandrasekhar and Detweiler as a (non self-adjoint) boundary problem [54]. Later on, Leaver developed a simple, but very powerful approach to this problem [55]. Since then, the calculation of (scalar, vector, gravitational and spinorial) QNMs for the main BHs in asymptotically flat spacetime, namely: RN [56–62], Kerr [55, 63, 64] and Kerr-Newman [65–67], has been carried out and cataloged in tables with great precision.

1.3.2 "Seeing" black holes

> "There are no shadows in the dark. Shadows are the servants of light"
>
> George R. R. Martin, A Clash of Kings

The Scottish physicist James Clerk Maxwell, beyond his fundamental contributions to Electrodynamics and Statistical Mechanics, was also deeply interested in the study of color vision [68]. In his work *"Experiments on Colour, as Perceived by the Eye, with Remarks on Colour-Blindness"*, Maxwell analyzed how different colors could be combined and perceived

by the human eye. Among his key findings, he identified three primary colors—red, green, and blue—as the fundamental basis of human color vision, a concept that would later become essential in modern RGB (red-green-blue) color models [69].

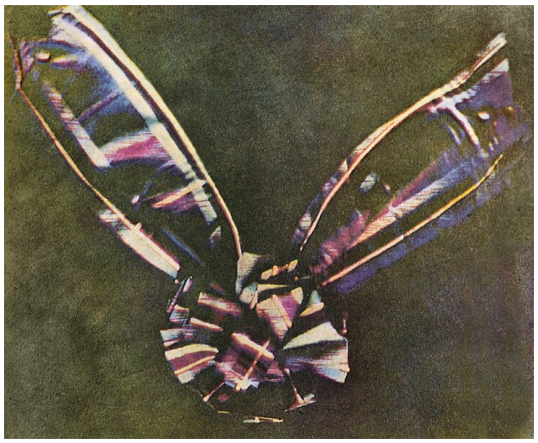

Figure 1.1: Image of a tartan ribbon, presented by Maxwell in his 1861 lecture to the Royal Institution [70].

In May 1861, Maxwell was invited to lecture at the Royal Institution on color vision [71]. Seeking a visual demonstration, he produced the first color photograph ever made. Using a method based on three black-and-white photographs, each taken with red, green, and blue filters. By projecting these filtered images with white light, and again using the respective filters, he reconstructed a full-color image. The photograph presented in the lecture can be visualized in Fig. 1.1.

Maxwell's experiment provides valuable insights into the process of generating images. To take a picture we need three key components: (i) The object to be imaged, which reflects, absorbs, or emits light to create visual information; (ii) A light source, allowing the object to be visible; and (iii) An observer, represented by the projecting camera in Maxwell's lecture. In Fig. 1.2, we present a schematic illustration depicting the interplay between these four components. For instance, the image observed by a camera positioned inside a sphere (also called a celestial sphere), emitting radiation isotropically and marked with grid lines, playing the role of the object, is displayed in Fig. 1.3. We also, for later reference, displayed an image with the celestial sphere partitioned into four quadrants, each designated by a distinct color: red, green, blue, and yellow. In addition to dividing the celestial sphere into four colors, we

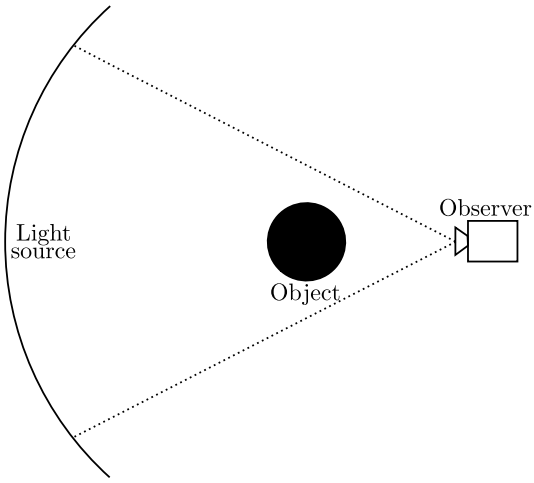

Figure 1.2: Schematic representation of the needed components to produce an image.

also insert a white filled circle on the celestial sphere, right in front of the observer, which will be behind the BH.

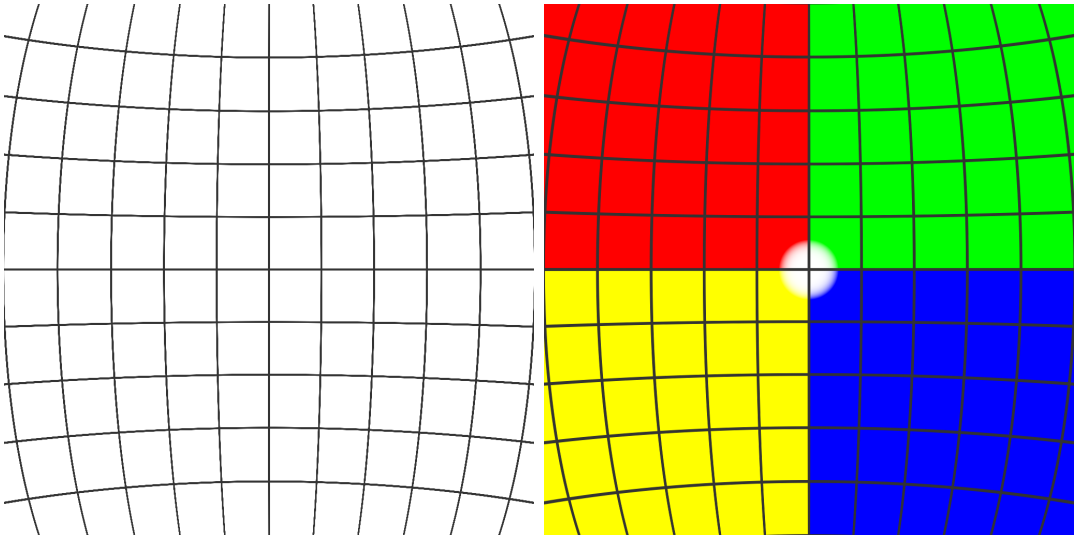

Figure 1.3: Observed pattern of inside a white sphere with grid lines.

In this Thesis, we are particularly interested in images of BHs. Although (classical) BHs do not emit any form of radiation, surrounding light sources make them observable. As a result, the 2-dimensional image of a BH illuminated from the back appears as a dark silhouette against a luminous background. The region in the image plane where no light is detected, resembling a black disk, is known as the BH's shadow [72].

Technological advancements have enabled us to locate and capture photographs of BHs.

These images, reported by the Event Horizon Telescope (EHT)[11], are of the supermassive BHs Sgr A* and M87* [73, 74]. A remarkable consequence of the EEP is that light bends in the presence of a gravitational field. Exploring how light bends around compact objects is a crucial aspect of Einstein's theory. The first experimental confirmation of GR was the observation of the gravitational deflection of light during a solar eclipse in 1919 [75, 76]. The phenomenon of gravitational lensing was investigated by Einstein himself. He studied the case when there is an alignment of the light source, the compact object and the observer, causing the appearance of a ring-like structure, now called Einstein ring [77]. With the landmark observations of the EHT [73, 74], the study of the gravitational lensing and the observational aspects of ultracompact objects, not only BHs but also BH foils such as boson stars, has become a very active area of research - see *e.g.* Refs. [78–103]

Near a BH, light can undergo substantial bending, creating circular trajectories called light rings (LRs). In Refs. [104,105], two theorems concerning the presence of LRs in generic contexts were established. The first of them demonstrates the existence of pairs of LRs around horizonless ultracompact objects, while the second establishes the existence of LRs specifically for BHs. These theorems do not rely on the Einstein (or other field) equations, but only on appropriate boundary conditions together with a topological technique. Both proofs were formulated based on a set of assumptions that encompass a broad range of spacetimes with physical relevance. An essential assumption is that the spacetime is asymptotically flat. Subsequently, extensions of the LR theorems for different asymptotics were put forward, covering cases such as Schwarzschild de Sitter and anti de Sitter [106], Schwarzschild-Melvin [107], Schwarzschild-dilatonic-Melvin [108] and Kerr-Newman Taub-NUT [109] spacetimes.

The idea of bound orbits that neither falls into the BHs nor escape to infinity encompasses more than just LRs. While LRs are a prominent example, they belong to a broader class of null trajectories known as fundamental photon orbits (FPOs) [110]. This set of orbits are associated with points on the shadow edge of a BH. The BH shadow can serve as an

[11] One of the telescopes used by the EHT collaboration is named the James Clerk Maxwell Telescope. We may interpret that this name honors not only Maxwell's contributions to electrodynamics, but also his pioneering work in image generation.

important signature of its underlying spacetime, potentially enabling the identification of the specific type of BH being observed. The shadow of the Schwarzschild BH observed by a static observer was obtained by Synge [111]. The shadow of the Kerr BH was first investigated by Bardeen [112]. However, there are cases where the shadows of totally different objects may exhibit similar patterns or even appear identical [113].

Liouville integrable spacetimes allow separation of variables and analytic expressions for the shadow's boundary. This is the case of Kerr BHs, which includes a Carter constant in addition to the conserved energy, angular momentum and particle's mass [114]. In spacetimes where the geodesic equations cannot be separated, the shadows and gravitational lensing phenomena can only be analyzed by numerical integration methods. A more computationally expensive method is based on evolving the light rays from the light sources to the camera. A more efficient approach to achieving the same result involves numerically evolving null geodesics backward in time, starting from the observer's position. This process continues until the light rays are either absorbed by the BH or scattered toward surrounding light sources. This method is known as the backward ray-tracing technique [107, 108, 115–117]. In this thesis, we only consider the previous described setup of a illuminated celestial sphere. As an example, we display in Fig. 1.4 an image of a Kerr BH. The observer is chosen to be the ZAMO frame. By comparing the two images of Fig. 1.4, we conclude that the use of colors in the celestial sphere greatly enhances the understanding of gravitational lensing effects. For more details on the backward ray-tracing method we refer the reader to [115].

1.4 A brief overview of the thesis

Starting in the 1960s, due to several astronomical discoveries related with pulsar, quasars and cosmic background radiation, Einstein's theory of GR experienced a new series of experimental confirmations [118, 119]. More recently, we had the detection of GWs and the caption of shadow images of M87* and Sgr A*, as discussed in Sec. 1.3. So GR is an exceptionally well-tested theory that establishes a big paradigm in physics. As a result, much of phenomenological research in gravitation naturally *gravitates* around GR—either reinforcing its paradigm or seeking deviations from it, motivated by various theoretical considerations.

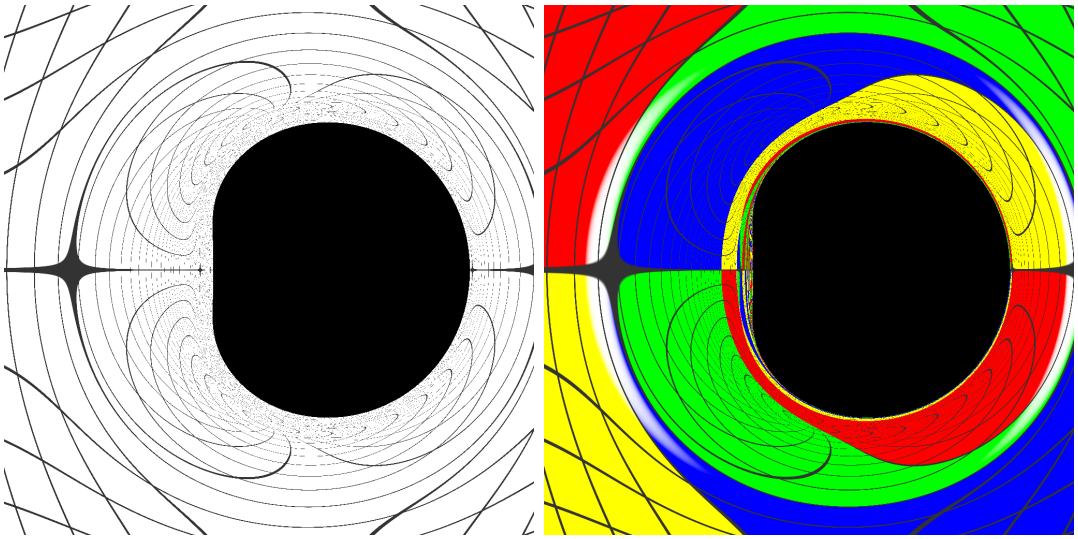

Figure 1.4: Shadow of an extremal Kerr BH using the backward ray-tracing method.

This thesis explores BH models within GR and beyond, with specific motivations detailed at the beginning of each chapter. Our analysis primarily examines QNMs, LRs, and shadows, each of which provides an indirect signature of the spacetime in examination. The rest of this Thesis is divided into more 2 parts. Each part has one or more chapters, based on the results of one or more scientific works published, accepted or submitted.

- **Part II: Quasinormal modes**

  – Zeus S. Moreira, Haroldo C. D. Lima Junior, and Luís C. B. Crispino, Quasinormal modes of a holonomy corrected Schwarzschild black hole, Phys. Rev. D **107**, 104016 (2023).

  In Chap. 2 we analyze the QNMs of a Schwarzschild BH with Loop Quantum Gravity (LQG) corrections, where a regular black bounce structure replaces the singularity. Using the WKB, Leaver, and Prony methods, we compute the frequencies and investigate deviations in high overtones from the Schwarzschild case. The time profile of a Gaussian scalar perturbation reveals that, at late times, the power-law behavior remains indistinguishable from that of Schwarzschild.

- **Part III: Black hole imaging**

- Zeus S. Moreira, Carlos A. R. Herdeiro, and Luís C. B. Crispino, Twisting shadows: Light rings, lensing, and shadows of black holes in swirling universes, Phys. Rev. D **109**, 104020 (2024).
- Zeus S. Moreira, Carlos A. R. Herdeiro, and Luís C. B. Crispino, Spinning generalizations of Majumdar-Papapetrou multi-black hole spacetimes: light rings, lensing and shadows, arXiv:2502.01759 [gr-qc] (2025). (Submitted to Phys. Rev. D)

In Chap. 3 we investigate the null geodesic flow and, in particular, the existence of light rings in this vacuum geometry. By evaluating the total topological charge w, we show that there exists one unstable light ring ($w = -1$) for each rotation sense of the background. We observe that the swirling background drives the Schwarzschild BH light rings *outside* the equatorial plane, displaying counter-rotating motion with respect to each other, while (both) co-rotating with respect to the swirling universe. Using backwards ray-tracing, we obtain the shadow and gravitational lensing effects, revealing a novel feature for observers on the equatorial plane: the BH shadow displays an *odd* $\mathbb{Z}_2$ (north-south) symmetry, inherited from the same type of symmetry of the spacetime itself: a twisted shadow.

In Chap. 4 we explore the dynamics of null geodesics on this geometry, focusing on the two-center solution. Using the topological charge formalism, we show that various light ring arrangements arise from different choices of individual angular momenta: light rings with opposite topological charges can merge and annihilate each other, resulting in configurations with a total of 4, 6, or 8 light rings. Using backward ray-tracing, we obtained the shadow and lensing of these spacetimes. The former, in particular, closely resembles those for the double-Kerr metric.

Part II

Quasinormal modes

Chapter 2

Quasinormal modes of a loop quantum corrected black hole

2.1 Effective models of quantum black holes

One of the most fundamental and longstanding issues in GR is the inevitability of spacetime singularities in physically relevant solutions of the EFE. Most relativists believe that GR is not the final theory of gravity and should be replaced by some quantum theory. It is widely belived that in a final quantum gravity theory, spacetime will not be plagued with singularities. The very early universe [120], the interior of BHs [121] and the last stages of BH evaporation [121] are examples of physical scenarios where quantum effects play a fundamental role, and GR can no longer give a precise description of the gravitational field. While all available observational data remain in strong agreement with the predictions of GR, these unresolved theoretical challenges strongly indicate the presence of new physics. However, despite substantial efforts and progress over the past few decades, a definitive theory of quantum gravity does not yet exist. This is one of the biggest open questions in theoretical physics to date, i.e. how to reconcile gravity with quantum mechanics.

The idea of canonically quantizing gravity, considering the spatial metric and its conjugate momentum as canonical variables, led to some problems [122]. Since the constraint equations are non-polynomial functions of the canonical variables, their corresponding operator equations in the quantum formulation are not well-defined [123]. Due to Sen, Ashtekar

and Barbero, a new set of coordinates was found, the Ashtekar-Barbero connection variables, such that the constraints equations were reduced to polynomial expressions [124–126]. By writing GR in terms of the Ashtekar-Barbero variables, it is possible to put the theory in a framework very similar to other quantum field theories, where quantization techniques have already been developed [127]. The early construction of Loop Quantum Gravity (LQG) was based on the quantization of GR, in terms of a smeared version of the connection variables in a background independent fashion. As some of the important results of LQG, we can mention the construction of singular-free cosmological models [128], the quantization of spherically symmetric vacuum spacetime [129], as well as the derivation of the Hawking-Bekenstein entropy [130].

Working within the full machinery of LQG is very challenging and some effective models have proven to be useful in understanding how quantum gravity effects might look like. There are several works applying modifications to GR for cosmological models [131,132] and also for spherically symmetric spacetimes, such as Schwarzschild [133–135] and RN solutions [136].

In Refs. [137,138] an effective spherically symmetric spacetime is proposed, which is non-singular and presents a global structure of a black bounce whose radius is hidden by an event horizon. Here we calculate the scalar QNMs of this quantum corrected BH, investigating how its spectrum deviates from the well-known Schwarzschild case.

The remainder of this chapter is organized as follows. In Sec. 2.2 we review some aspects of the solution obtained in Refs. [137, 138], highlighting its main properties. In Sec. 2.3 we investigate the dynamics of a massless scalar field over the quantum corrected spacetime and review the corresponding boundary problem of QNMs. In Sec. 2.4 we revisit two methods for calculating QNM frequencies, namely the third order Wentzel-Kramers-Brillouin (WKB) approximation, as well as the Leaver's continued fraction method. In Sec. 2.5 we exhibit a selection of our numerical results. We first compare, as a consistency check, the third order WKB results and the ones obtained via continued fraction calculations. We also compute, with the Leaver method, the first 30 overtones for the modes $l = 0$ and $l = 1$. We present some remarks regarding this chapter in Sec. 2.6.

2.2 Effective quantum corrected Schwarzschild spacetime

The authors of Ref. [137, 138] reported the following line element:

$$ds^2 = -f(r)dt^2 + \left[\left(1 - \frac{r_0}{r}\right) f(r)\right]^{-1} dr^2 + r^2 d\Omega^2, \tag{2.1}$$

where $r_0 < 2M$ is a LQG parameter, also called the holonomy parameter, $f(r) \equiv 1 - 2M/r$ and $d\Omega^2$ is the line element of the 2-sphere. This metric represents a static, spherically symmetric and asymptotically flat spacetime. The horizon is located at the hypersurface $r = r_h = 2M$, similarly to what we have in Schwarzschild spacetime. Nonetheless, the quantity M cannot be simply interpreted as the mass of the BH. As pointed out in Ref. [138], the different geometric definitions of mass, namely, the Komar, ADM and Misner-Sharp masses, need to be taken into account. These quantities are given by

$$M_{\rm K} = M\sqrt{1 - \frac{r_0}{r}}, \tag{2.2a}$$

$$M_{\rm ADM} = M + \frac{r_0}{2}, \tag{2.2b}$$

$$M_{\rm MS} = M + \frac{r_0}{2} - \frac{Mr_0}{r}, \tag{2.2c}$$

where $M_{\rm K}$, $M_{\rm ADM}$ and $M_{\rm MS}$ are the Komar, ADM and Misner-Sharp mass, respectively. The Komar and Misner-Sharp masses do not need to coincide, since the quantum corrected spacetime is not a solution of the EFE [139]. However, in the limit that r goes to infinity, for spherically symmetric and asymptotically flat spacetimes, the ADM and Misner-Sharp masses must be equal [140], what is indeed the case. The BH parameters, M and r_0 can be redefined in a geometric invariant way, according to

$$M = \lim_{r\to\infty} M_{\rm K}, \tag{2.3a}$$

$$r_0 = 2\lim_{r\to\infty}(M_{\rm MS} - M_{\rm K}). \tag{2.3b}$$

In FIG.2.1 we display the Penrose diagram of the spacetime maximal extension [138]. Region I stands for the asymptotically flat region in which $r \in (r_h, \infty)$. This patch have the usual conformal infinities, namely, the timelike infinities, i^- and i^+, the null infinities, $\mathcal{J}^-$ and $\mathcal{J}^+$ and the spatial infinity i^0. Region II stands for the BH region and corresponds to $r \in (r_0, r_h)$. The remaining regions III and IV, which cannot be covered by the coordinate system

(t, r, θ, φ), are the white hole region and another asymptotically flat region, respectively. The bottom and upper regions in blank with dashed contour are copies of the middle structure [138].

The hypersurface $r = r_0$ is not a wormhole throat, since r is a time-like coordinate in the region $r_0 < r < r_h$. In fact, it corresponds to a bounce surface, analogous to the ones studied, for instance, in Refs. [141, 142]. Hence, this spacetime has a global structure of a black bounce (see FIG. 2.1). The authors of Refs. [137, 138] reported that the bounce radius r_0 arises from the procedure called polymerization procedure

$$r_0 = 2M\frac{\lambda^2}{\lambda^2 + 1}, \tag{2.4}$$

where λ is a positive dimensionless parameter. From Eq. (2.4) we note that the bounce is hidden by the event horizon ($r_0 < r_h$). Therefore, as shown in Sec. 2.5, the bounce does not reveal itself in the QNMs, except for the fact that the metric tensor components depend on r_0. This is a particular feature of the loop quantum corrected Schwarzschild spacetime. In other models of black bounce, the surface $r = r_0$ can be located outside the event horizon [141, 142]. In such cases, there is a transition to a wormhole spacetime and echoes appear in the QNM spectrum (for instance, Refs. [143–145]). The effective quantum Schwarzschild spacetime, differently from the Schwarzschild BH, is regular everywhere, as can be verified by computing the curvature scalar of this spacetime.

2.3 Scalar perturbations

The dynamics of a massless scalar field Φ is determined by the Klein-Gordon equation

$$\nabla_\mu \nabla^\mu \Phi = \frac{1}{\sqrt{-g}}\partial_\mu \left(\sqrt{-g} g^{\mu\nu}\partial_\nu \Phi\right) = 0, \tag{2.5}$$

where g is the metric determinant and $g^{\mu\nu}$ are the contravariant components of the metric tensor. Due to spherical and time translation symmetries, the scalar field admits the product decomposition given by

$$\Phi(x^\mu) = \frac{\psi_{\omega l}(r)}{r} Y_{lm}(\theta, \varphi) e^{-i\omega t}, \tag{2.6}$$

where $Y_{lm}(\theta, \varphi)$ are the spherical harmonics.

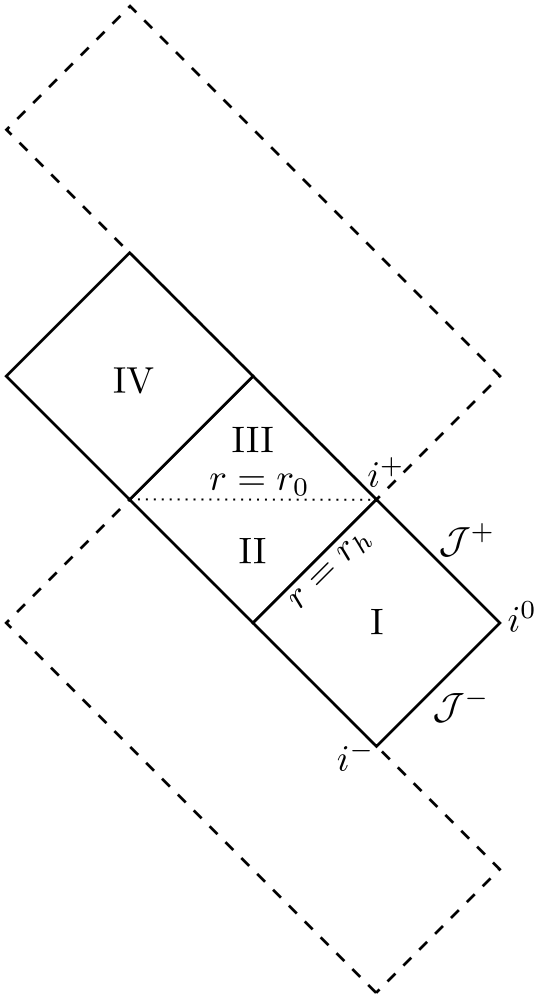

Figure 2.1: Penrose diagram representing the global structure of the spacetime proposed in Refs. [137, 138], which corresponds to a black bounce solution with radius r_0.

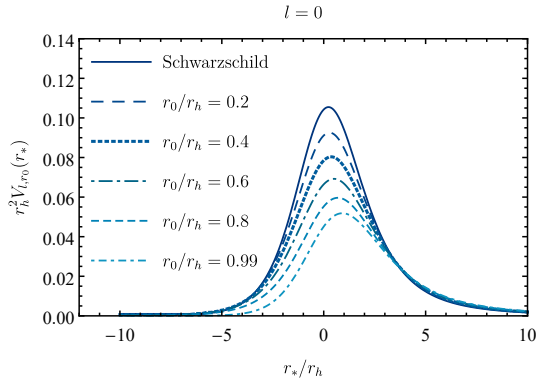

Figure 2.2: Effective potential given in Eq. (2.8) as a function of the tortoise coordinate for various values of r_0 and $l = 0$.

Inserting the metric components given in Eq. (2.1), as well as the field decomposition given in Eq. (2.6), into Eq. (2.5), we obtain a Schrödinger-like equation for the radial part, which is given by

$$\frac{d^2\psi_{\omega l}}{dr_*^2} + \left(\omega^2 - V_{l,r_0}[r(r_*)]\right)\psi_{\omega l} = 0, \tag{2.7}$$

where the effective potential $V_{l,r_0}(r)$ is defined by

$$V_{l,r_0}(r) = f(r)\left(\frac{l(l+1)}{r^2} + \frac{4M + r_0}{2r^3} - \frac{3Mr_0}{r^4}\right), \tag{2.8}$$

and r_* is the tortoise coordinate:

$$dr_* = \frac{dr}{f(r)\sqrt{1 - r_0/r}}. \tag{2.9}$$

The effective potential is illustrated in FIG. 2.2, where we see that the maximum value of the potential decreases as we increase the LQG parameter r_0.

To calculate the scalar QNMs of the loop quantum corrected Schwarzschild spacetime we have to solve Eq. (2.7), imposing the boundary conditions

$$\psi_{\omega l}(r_*) \approx \begin{cases} e^{-i\omega r_*} \approx (r - 2M)^{\frac{-2i\omega M}{\sqrt{1-\frac{r_0}{2M}}}} & r_* \to -\infty \\ e^{+i\omega r_*} \approx e^{i\omega r} r^{2i\omega M + \frac{i\omega r_0}{2}} & r_* \to +\infty \end{cases}. \tag{2.10}$$

Eqs. (2.7) and (2.10) define an eigenvalue problem for $\psi_{\omega l}$ with eigenvalue ω in the domain $r \in (2M, \infty)$. We expect that the spectrum is a countable infinite set $\{\omega_n |\ n = 0, 1, ...\}$, where n enumerates the eigenfrequencies in increasing imaginary part magnitude order, the so-called overtones.

In general, an expression for the spectrum cannot be written in a closed analytical form, not even for Schwarzschild. Thus, it is common to implement approximate and numerical methods to treat the problem of QNMs. In the next session, we implement the third order WKB, continued fraction and the Prony methods to compute the scalar eigenfrequencies of the loop quantum corrected Schwarzschild spacetime.

2.4 scalar QNMs calculations

2.4.1 WKB approximation

The first method we implemented for the calculation of scalar QNMs is the third order WKB approximation. The WKB method is a semianalytic technique, first applied to BH scattering problems by Schutz and Will [146] and then improved by Iyer and Will [147]. For any barrier-type potential whose extremities are fixed (which is our case, see FIG. 2.2), this method can be applied and yields an analytic formula that approximates the QNM frequencies.

The third order WKB approximation is given by [147]:

$$\omega^2_{l,r_0,n} \approx V_0 + \sqrt{-2V_0''}\Lambda - i\left(n+\frac{1}{2}\right)\sqrt{-2V_0''}(1+\Omega), \tag{2.11}$$

with

$$\Lambda = \frac{1}{\sqrt{-2V_0''}}\left[\frac{1}{8}\left(\frac{V_0^{(4)}}{V_0''}\right)\left(\frac{1}{4}+\kappa^2\right) - \frac{1}{288}\left(\frac{V_0'''}{V_0''}\right)^2\left(7+60\kappa^2\right)\right], \tag{2.12a}$$

where V_0 is the maximum value of V_{l,r_0}, $\kappa = n+1/2$, the primes corresponds to first, second and third order derivatives, while the superscript in round brackets (i) denotes derivative of fourth and higher orders with respect to the tortoise coordinate. We note that there is an alternative but equivalent method to the third order WKB approximation, proposed in Ref. [148], based on an analogy between the BH QNM problem and a quantum anharmonic oscillator. (The third order WKB corrections given in Eq. (2.12) can be interpreted as the

anharmonicity corrections to the potential [148].) In this work, such approximations will be used mainly as a consistency check for the continued fraction method.

2.4.2 Continued fraction method

One of the most accurate methods to calculate QNMs was implemented in BH physics by Leaver [55] and it is called the continued fraction method. This method is based on finding an analytical solution of the radial equation as a power series satisfying the QNM boundary conditions. Thus, the QNM spectrum is determined by those values of the frequencies which make the series convergent on the entire domain.

In order to apply the power series method, we first need to investigate the regular/irregular singular points of the ordinary differential equation (2.7) (see Ref. [149] for further details). The singularities of Eq. (2.7) are $\{0, r_0, 2M, \infty\}$, where the singularity at infinity is irregular and all the others are regular. The power series solutions around some singularity has a convergence radius which cannot be greater than the distance to the next neighboring singular point. Since the domain of the QNM eigenvalue problem is $(2M, \infty)$, we cannot find a well defined solution in the entire domain using a power series of r. Therefore, we consider the map

$$r \mapsto \frac{r-2M}{r-r_0}. \tag{2.13}$$

Let $(0, r_0, 2M, \infty)$ be the ordered 4-tuple formed by the singularities of Eq. (2.7). This 4-tuple, according to Eq. (2.13), is mapped to $(2M/r_0, \infty, 0, 1)$ (see FIG. 2.3). Moreover, the domain $(2M, \infty)$ is compactified into $(0, 1)$. The singular point $2M/r_0$ is always greater than 1, since $0 < r_0 < 2M$. Hence, in this new coordinate defined by Eq. (2.13), we can find a well defined analytical solution of Eq. (2.7) in the domain $(0, 1)$, which correspond to the entire domain of interest.

We, therefore, may consider the solution of Eq. (2.7) to be

$$\psi_{\omega l} = r(r-r_0)^{2i\omega M + \frac{i\omega r_0}{2} - 1} e^{i\omega r} \sum_{n=0}^{\infty} a_n \left(\frac{r-2M}{r-r_0}\right)^{\zeta+n}, \tag{2.14}$$

where

$$\zeta = \frac{-2i\omega M}{\sqrt{1-\frac{r_0}{2M}}} \tag{2.15}$$

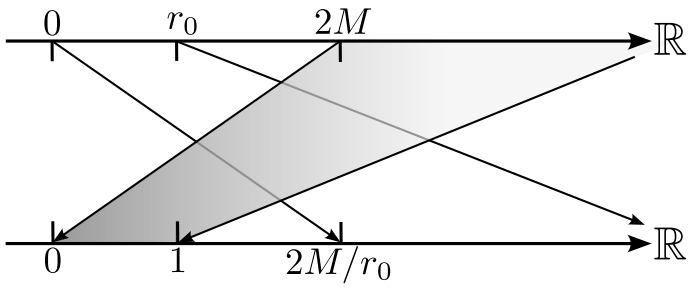

Figure 2.3: Schematic representation of the map defined by Eq. (2.13). We assign the values taken by singularities $(0, r_0, 2M, \infty) \mapsto (2M/r_0, \infty, 0, 1)$ and show how the domain $(2M, \infty)$ is mapped to $(0, 1)$.

is the characteristic exponent obtained from the indicial equation [149] corresponding to the ingoing solution at the horizon. The functions multiplying the summation are chosen to satisfy the boundary conditions at infinity, as well as to simplify the recurrence relation.

The sequence $(a_n)_{n\in\mathbb{N}}$ is determined by a four-term recurrence relation defined by

$$\alpha_0 a_1 + \beta_0 a_0 = 0 \tag{2.16a}$$

$$\alpha_1 a_2 + \beta_1 a_1 + \gamma_1 a_0 = 0 \tag{2.16b}$$

$$\alpha_n a_{n+1} + \beta_n a_n + \gamma_n a_{n-1} + \delta_n a_{n-2} = 0, \qquad n = 2, 3, ..., \tag{2.16c}$$

where the recurrence coefficients are given by

$$\alpha_n = -32i\sqrt{2}M^{5/2}(n+1)\omega(2M - r_0) + 8M(n+1)^2(2M - r_0)^{3/2}, \tag{2.17a}$$

$$\begin{aligned}\beta_n = {} & 64M^4\omega^2(2M - r_0)^{1/2} + 8\sqrt{2}M^{5/2}\omega(12M\omega + 12in + 5i)(2M - r_0) + \\ & 4M\left(-2l(l+1) + 24M^2\omega^2 + 6iM(2n+1)\omega - n(6n+5) - 2\right)(2M - r_0)^{3/2} \\ & + 4\sqrt{2}M^{3/2}\omega(4M\omega - 4in - i)(2M - r_0)^2 \\ & + 2(2n+1)(n + 2iM\omega)(2M - r_0)^{5/2},\end{aligned} \tag{2.17b}$$

$$\begin{aligned}\gamma_n =& -128M^4\omega^2(2M-r_0)^{1/2} - 16\sqrt{2}M^{5/2}\omega(12M\omega+6in-i)(2M-r_0)\\ &+4M\left(2l(l+1)+n(-2-24iM\omega)+M\omega(-34M\omega+3i)+6n^2+1\right)(2M-r_0)^{3/2}\\ &+8\sqrt{2}M^{3/2}\omega(6M\omega+4in-i)(2M-r_0)^2\\ &+\left(-4l(l+1)+72M^2\omega^2+4iM(6n-1)\omega-8n^2+4n-2\right)(2M-r_0)^{5/2}\\ &+8\sqrt{2}M^{3/2}\omega^2(2M-r_0)^3\\ &+\omega(-2M\omega+4in-i)(2M-r_0)^{7/2},\end{aligned} \tag{2.17c}$$

$$\begin{aligned}\delta_n =& \,64M^4\omega^2(2M-r_0)^{1/2}+8\sqrt{2}M^{5/2}\omega(12M\omega+4in-3i)(2M-r_0)\\ &+4M\left(3n(1+4iM\omega)+M\omega(10M\omega-9i)-2n^2-1\right)(2M-r_0)^{3/2}\\ &+\left(-4\sqrt{2}M^{3/2}\omega(16M\omega+4in-3i)\right)(2M-r_0)^2\\ &+\left(n(-6-32iM\omega)+12M\omega(-5M\omega+2i)+4n^2+2\right)(2M-r_0)^{5/2}\\ &+8\sqrt{2}M^{3/2}\omega^2(2M-r_0)^3+\omega(14M\omega+4in-3i)(2M-r_0)^{7/2}-\omega^2(2M-r_0)^{9/2}.\end{aligned} \tag{2.17d}$$

This recurrence relation is in agreement with Leaver's hypothesis, which says that a radial equation with a confluent singularity and three regular singularities generates a solution whose expansion coefficients obey a 4-term recurrence relation [58].

To calculate the QNM from a 4-term recurrence relation we first have to apply the Gaussian elimination scheme, defined by

$$\tilde{\alpha}_n \equiv \alpha_n, \quad \tilde{\beta}_n \equiv \beta_n, \quad \tilde{\gamma}_n \equiv \gamma_n, \quad \text{for } n = 0, 1\ , \tag{2.18}$$

and

$$\tilde{\delta}_n \equiv 0, \quad \tilde{\alpha}_n \equiv \alpha_n, \tag{2.19a}$$

$$\tilde{\beta}_n \equiv \beta_n - \frac{\tilde{\alpha}_{n-1}\delta_n}{\tilde{\gamma}_{n-1}}, \quad \tilde{\gamma}_n \equiv \gamma_n - \frac{\tilde{\beta}_{n-1}\delta_n}{\tilde{\gamma}_{n-1}} \quad \text{for } n \geq 2. \tag{2.19b}$$

The new recurrence coefficients now obey a 3-term recurrence relation given by

$$\tilde{\alpha}_0 a_1 + \tilde{\beta}_0 a_0 = 0, \tag{2.20a}$$

$$\tilde{\alpha}_n a_{n+1} + \tilde{\beta}_n a_n + \tilde{\gamma}_n a_{n-1} = 0, \quad n = 1, 2, \ldots\ . \tag{2.20b}$$

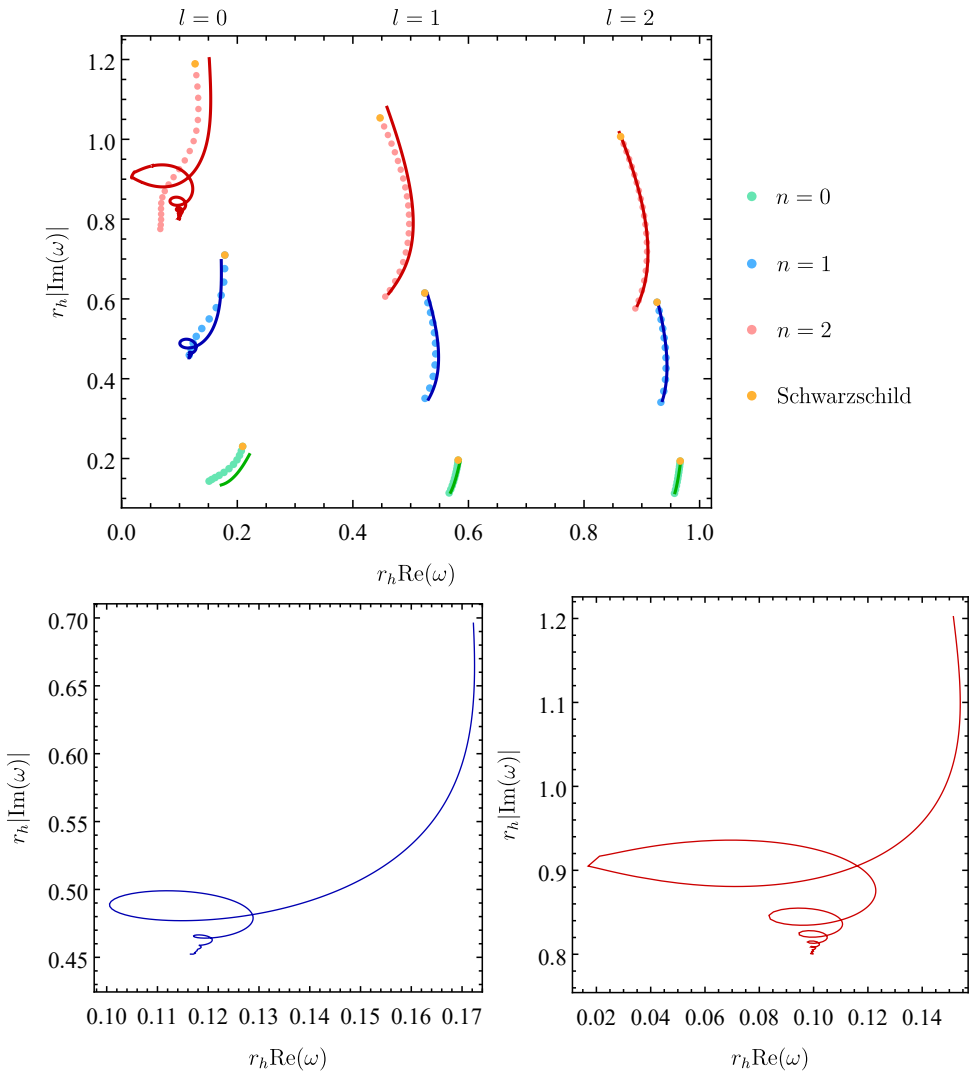

Figure 2.4: *Top*: First three ($n = 0, 1, 2$) QNM-frequencies of the scalar field on the quantum corrected Schwarzschild spacetime. The green plots correspond to $n = 0$, blue to $n = 1$ and red to $n = 2$. Circles represent the WKB calculations, for several values of the LQG parameter r_0, beginning at $r_0/r_h = 0$ (yellow circles representing the Schwarzschild case) and ending at $r_0/r_h = 0.99$. The solid line shows the continued fraction calculation in the same range of parameters. *Bottom*: Computation of QNM frequencies for $n = 1$, $l = 0$ (bottom left panel) and $n = 2$, $l = 0$ (bottom right panel) for r_0/r_h ranging from 0 to 0.99, obtained using the continued fraction method with Nollert improvement [150]. All the frequencies become less damped as r_0/r_h increases.

The condition that the series defined in Eq. (2.14) converges uniformly is given by [55]

$$\begin{aligned} 0 &= \tilde{\beta}_0 - \cfrac{\tilde{\alpha}_0\tilde{\gamma}_1}{\tilde{\beta}_1 - \cfrac{\tilde{\alpha}_1\tilde{\gamma}_2}{\tilde{\beta}_2 - \cfrac{\tilde{\alpha}_2\tilde{\gamma}_3}{\tilde{\beta}_3 - \ldots}}}, \\ &\equiv \tilde{\beta}_0 - \frac{\tilde{\alpha}_0\tilde{\gamma}_1}{\tilde{\beta}_1-}\frac{\tilde{\alpha}_1\tilde{\gamma}_2}{\tilde{\beta}_2-}\frac{\tilde{\alpha}_2\tilde{\gamma}_3}{\tilde{\beta}_3-}\ldots \end{aligned} \tag{2.21}$$

Thus, the set of frequencies that makes Eq. (2.21) true are, precisely, the QNM frequencies.

The roots of Eq. (2.21) can be found numerically. The most stable root of the continued fraction defined in Eq. (2.21) is the fundamental mode. The n-th inversion of Eq. (2.21) is defined by

$$\tilde{\beta}_n - \frac{\tilde{\alpha}_{n-1}\tilde{\gamma}_n}{\tilde{\beta}_{n-1}-}\ldots - \frac{\tilde{\alpha}_0\tilde{\gamma}_1}{\tilde{\beta}_0} = \frac{\tilde{\alpha}_n\tilde{\gamma}_{n+1}}{\tilde{\beta}_{n+1}-}\frac{\tilde{\alpha}_{n+1}\tilde{\gamma}_{n+2}}{\tilde{\beta}_{n+2}-}\ldots, \tag{2.22}$$

and its most stable root is the n-th eigenfrequency.

2.4.3 Prony method

We can also solve Eq. (2.5) without assuming the time dependence $e^{-i\omega t}$ in Eq. (2.6). This lead to the partial differential equation (PDE):

$$\frac{\partial^2\Psi_l}{\partial r_*^2} - \frac{\partial^2\Psi_l}{\partial t^2} - V_{l,r_0}[r(r_*)]\Psi_l = 0, \tag{2.23}$$

where now Ψ_l is a function of the variables (t, r_*). We may solve Eq. (2.23) numerically, setting a Gaussian wave package centered at $r_* = 0$ as our initial configuration for the field. The time evolution of the solution is characterized by three stages: (i): a prompt response at early times, which is strongly determined by the chosen initial conditions of the field, *(ii):* exponential decay at intermediate times, determined by the QNMs and *(iii):* power-law fall-off at late times, due to backscattering of the field in tail of the potential.

Once the Eq. (2.23) is solved for some initial data configuration, by means of estimating methods, one is able to construct an analytic approximation that fits the original solution. Here we use the Prony method to find an approximate Fourier decomposition, which allows us to calculate the fundamental mode. A detailed description of the Prony method can be found in Ref. [151].

2.5 Results

In this section we exhibit a selection of our results, obtained from the methods described in the previous sections.

As a consistency check that the continued fraction method leads to the correct values of the eigenfrequencies, we first compare the QNMs calculated with Leaver's method and the WKB approximation.

We compute the QNMs $n = 0, 1, 2$ for different numbers of the azimuthal number $l = 0, 1, 2$. The results are exhibited in the top panel of FIG. 2.4. We define a color code for each value of n, namely: green $\leftrightarrow n = 0$, blue $\leftrightarrow n = 1$ and red $\leftrightarrow n = 2$. The (green, blue and red) circles represent the QNMs calculated with the WKB method, while the solid lines were obtained by the continued fraction method. Both, WKB and the continued fraction calculations, were computed for r_0/r_h ranging from 0 (Schwarzschild) to 0.99. The yellow circles, located at the top of each continuous line, represents the quasinormal frequencies of the Schwarzschild BH calculated using the WKB approximation.

FIG. 2.4 shows that, as we increase the values of l, the results obtained from WKB and continued fraction methods converge to the same value, which was already expected. Nonetheless, even for $l = 0$, both, WKB and continued fraction methods, results are in very good agreement.

From the continued fraction computations we also note that the curves in the complex plane, parametrized by r_0/r_h, for $n > 0$ and $l = 0$, have a spiral-like shape. We display the curves for $n = 1$, $l = 0$ and $n = 2$, $l = 0$ in the left and right bottom panels of FIG. 2.4, respectively. We note that, in order to obtain the results shown in the bottom panel of FIG. 2.4, we applied the continued fraction method with the improvement proposed by Nollert [150]. The Nollert improvement is suitable to compute QNM frequencies with large imaginary part, hence it gives accurate numerical results when the LQG parameter is close to the extreme value. While the LQG parameter varies in the indicated range, the trajectory described in the complex plane moves away from the Schwarzschild QNMs and spirals towards some fixed complex value, which corresponds to the QNMs associated with the extremal case. A similar behavior was also found for the RN BH [62]. We also note that

that these curves are self-intersecting. The existence of self-intersecting curves in the orbits of the QNM frequencies is related to the fact that, for different values of the LQG parameter r_0, the BH may present the same frequency for some given n.

2.5.1 $l = 0$ Modes

We can fix $l = 0$ and compute the first 30 modes for several values of r_0/r_h. The results, calculated with the continued fraction method, are displayed in FIG. 2.5. The small deviation from Schwarzschild regime ($r_0/r_h = 0,\ 0.05,\ 0.1$) is displayed in the top left panel of FIG. 2.5, where we obtain the famous Schwarzschild's scalar spectrum, formed by two non-intersecting branches of QNM frequencies, with slight disturbances. There is a decrease in the damping, in accordance with FIG. 2.4.

Nonetheless, the QNM frequencies for higher values of r_0/r_h are completely different from the Schwarzschild case. In the remaining panels of FIG. 2.5 we exhibit the spectrum near $r_0/r_h = 0.2,\ 0.3,\ 0.4,\ 0.5$. As the LQG parameter varies, the real part of the frequencies oscillates. We obtained frequencies with $\mathrm{Re}(\omega) = 0$, e.g. the mode $n = 4$ for $r_0/r_h = 0.48$. However, the continued fraction method does not converge for $\mathrm{Re}(\omega) \to 0$, hence the existence of purely damped modes cannot be indeed stated.

We remark that the existence of frequencies with real part almost equal to zero can be found in Schwarzschild's QNM spectrum for the gravitational field. The algebraically special frequency $2M\omega \approx -i(l-1)(l+1)(l+2)/6$ is almost a pure imaginary number [152]. In the Schwarzschild case the algebraically special frequency does not exist for fields other than the gravitational field. Thus, qualitatively, in the weakly damped regime, the spectrum of the quantum corrected Schwarzschild BH for the scalar field resembles the spectrum of the Schwarzschild BH for the gravitational field.

2.5.2 $l = 1$ Modes

We may now fix $l = 1$ and compute the first 30 modes for the same values of the LQG parameter of Sec. 2.5.1. The QNMs were calculated using the continued fraction method and are displayed in FIG. 2.6. Once more, small holonomy corrections $r_0/r_h = 0,\ 0.05,\ 0.1$

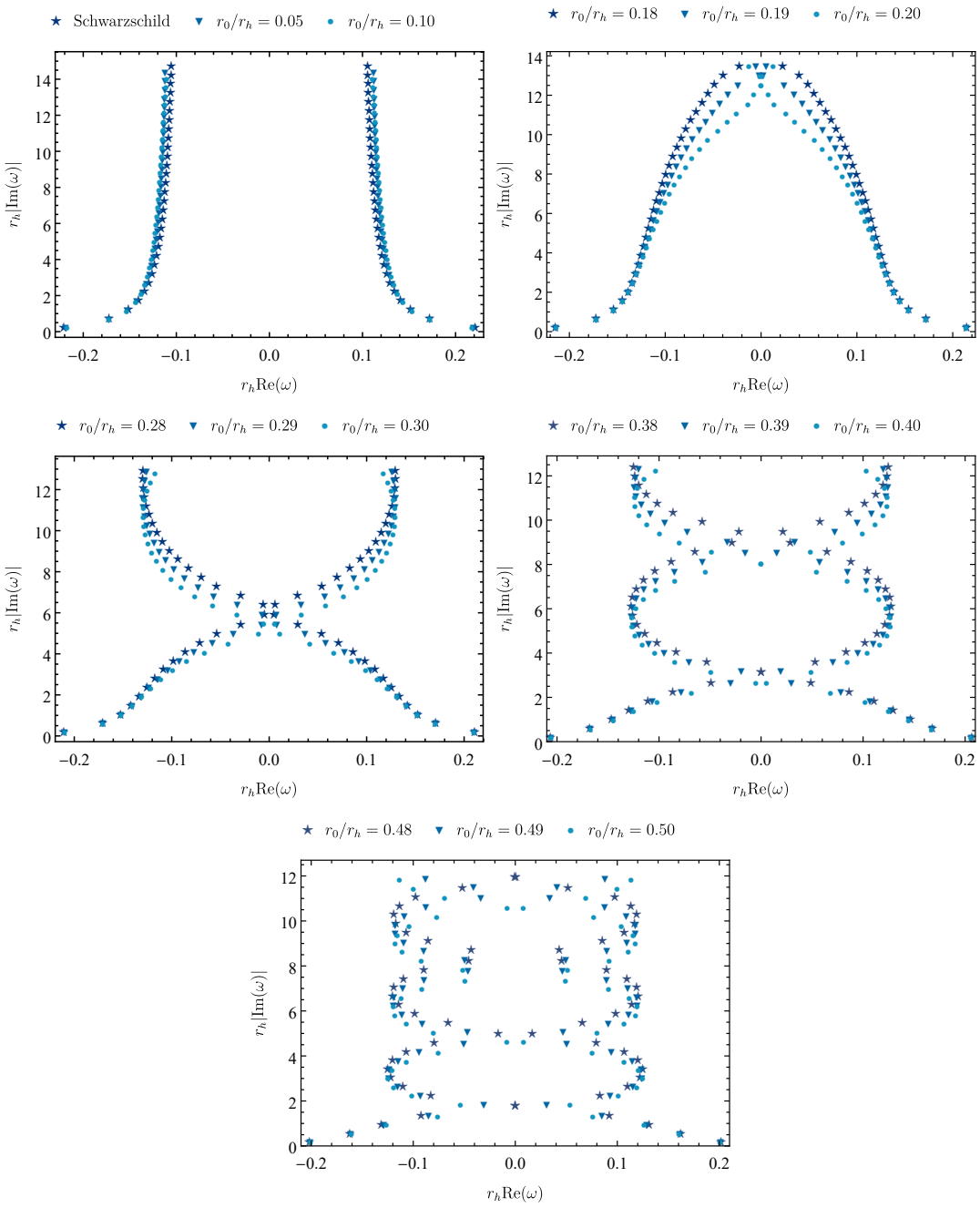

Figure 2.5: First 30 QNM frequencies ($n = 0, 1, ..., 29$) of the scalar field on the quantum corrected Schwarzschild spacetime for $l = 0$. The top left panel shows the modes for $r_0/r_h = 0,\ 0.05,\ 0.1$, whereas the remaining panels exhibit the spectrum of the quantum corrected BH for values of the LQG parameter near $r_0/r_h = 0.2,\ 0.3,\ 0.4,\ 0.5$. All the spectra were calculated with the continued fraction method.

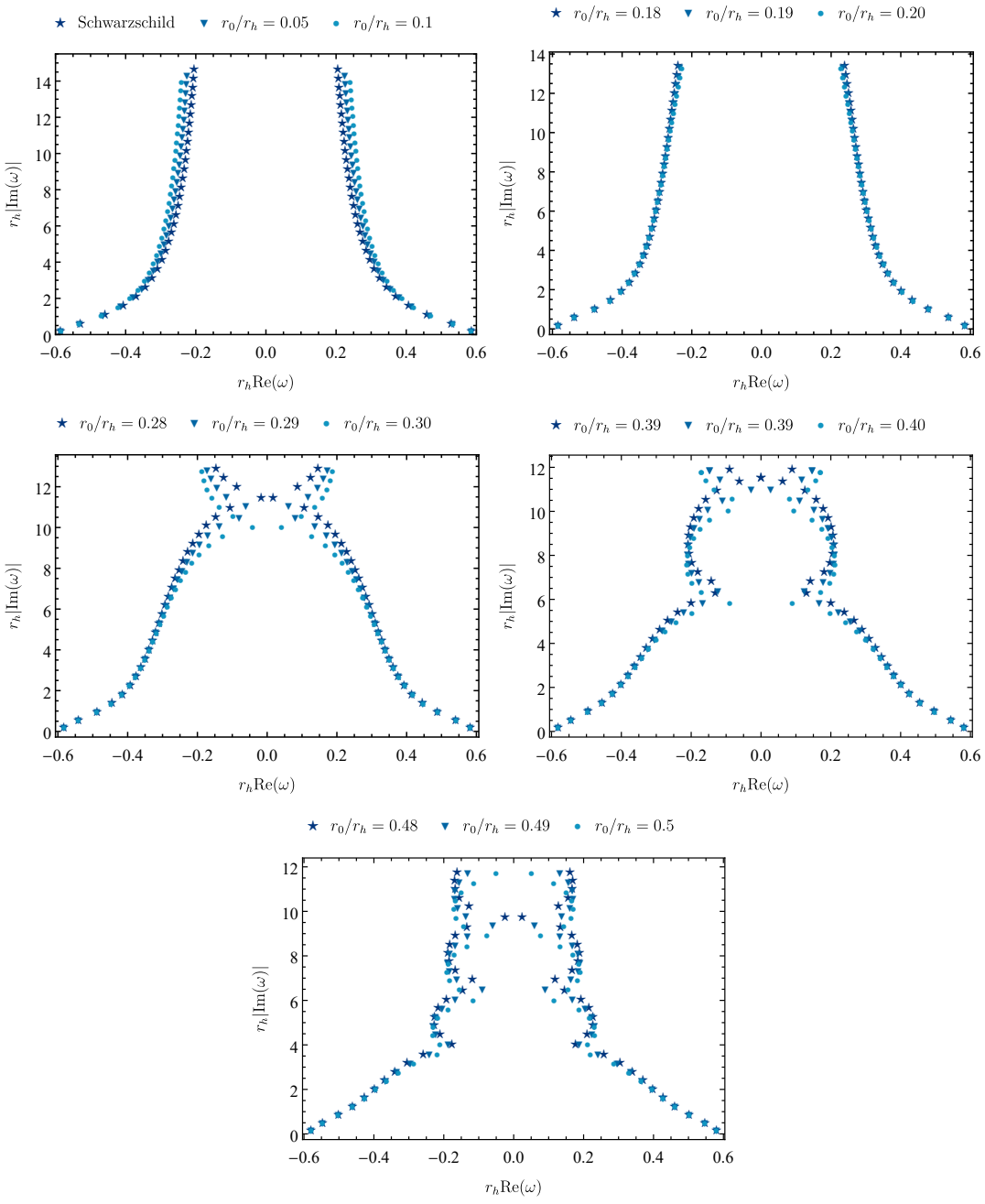

Figure 2.6: First 30 QNM frequencies ($n = 0, 1, ..., 29$) of the scalar field on the quantum corrected Schwarzschild spacetime for $l = 1$. We display in the top left panel the modes $r_0/r_h = 0,\ 0.05,\ 0.1$, whereas in the remaining panels we show the spectrum for higher values of the LQG parameter, namely near $r_0/r_h = 0.2,\ 0.3,\ 0.4,\ 0.5$. All spectra were calculated with the continued fraction method.

$l = 0$ (Leaver)		
n	Schwarzschild	$r_0/r_h = 0.3$
0	$0.2209 - 0.2097i$	$0.2099 - 0.1828i$
1	$0.1722 - 0.6961i$	$0.1705 - 0.5996i$
2	$0.1514 - 1.2021i$	$0.1518 - 1.0329i$
3	$0.1408 - 1.7073i$	$0.1403 - 1.4657i$
4	$0.1341 - 2.2112i$	$0.1307 - 1.8974i$

Table 2.1: First five overtones of scalar perturbations, expressed in r_h^{-1} units, calculated by the continued fraction method for $l = 0$. We consider the Schwarzschild BH, as well as the holonomy corrected Schwarzschild BH with $r_0/r_h = 0.3$.

lead to small disturbances in the Schwarzschild spectrum, leading to an overall decrease in the imaginary part of the QNM frequencies.

The QNMs for higher values of the LQG parameter, namely, near $r_0/r_h = 0.2,\ 0.3,\ 0.4,\ 0.5$, are displayed in the remaining panels of FIG. 2.6. As we increase the value of r_0/r_h, again the oscillatory pattern appears in the spectrum of the quantum corrected BH. The first five overtones are also exhibited in Table 2.2.

$l = 1$ (Leaver)		
n	Schwarzschild	$r_0/r_h = 0.3$
0	$0.5858 - 0.1953i$	$0.5824 - 0.1738i$
1	$0.5288 - 0.6125i$	$0.5416 - 0.5395i$
2	$0.4590 - 1.0802i$	$0.4892 - 0.9406i$
3	$0.4065 - 1.5766i$	$0.4473 - 1.3640i$
4	$0.3702 - 2.0815i$	$0.4172 - 1.7952i$

Table 2.2: First five overtones of scalar perturbations, expressed in r_h^{-1} units, calculated by the continued fraction method for $l = 1$. We considered the Schwarzschild BH, as well as the holonomy corrected Schwarzschild BH with $r_0/r_h = 0.3$.

The pattern exhibited in both FIGs. 2.5 and 2.6 may go on forever as n increases. However such analysis requires an asymptotic study of QNMs that is beyond the scope of

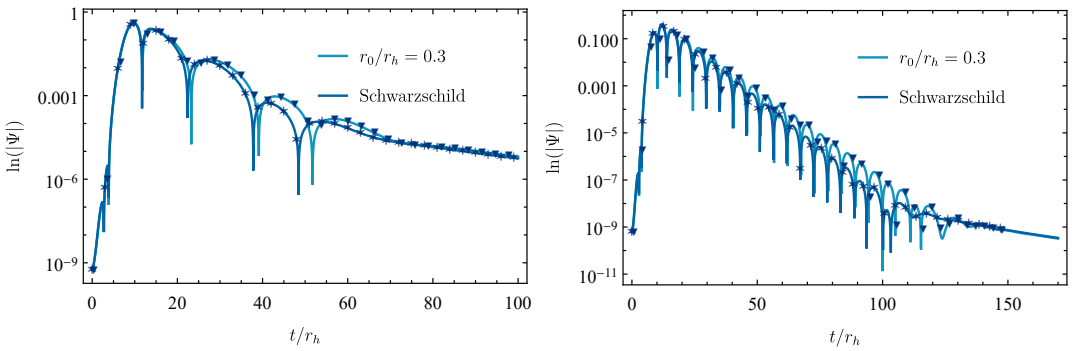

Figure 2.7: Plots of $\ln|\Psi_l(t, r_* = 10)|$ for $l = 0$ (left panel) and $l = 1$ (right panel). In both plots, we include the Schwarzschild case (darker blue), the quantum corrected Schwarzschild case with $r_0/r_h = 0.3$ (lighter blue) and also the associated fittings obtained from the Prony method (stars and inverted triangles, respectively).

our work. If this assertion is true, then the limit $\lim_{n\to\infty} \Re(\omega)$ does not exist, what would differ from the Schwarzschild's case, which is known to be $2M \lim_{n\to\infty} \Re(\omega) = \ln 3/4\pi$ [153].

2.5.3 Time domain profile

We may solve numerically the time-dependent wave equation given by Eq. (2.23), and for that, we need to specify an initial condition. We consider the initial data as a Gaussian, according to

$$\Psi_l(0, r_*) = e^{-r_*^2/4};\ \partial_t \Psi_l(t, r_*)|_{t=0} = 0. \tag{2.24}$$

The chosen initial data do not play a significant role in the time profile of the wave function from intermediate times onwards. After a transient initial stage (highly dependent on initial conditions), the time profile is dominated by the QNMs and then by the late time tail decay.

In FIG. 2.7 we exhibit the logarithmic plot for the absolute value of the solution as a function of time. The tortoise coordinate is fixed at $r_*/r_h = 10$. We consider the cases $l = 0$ (left panel) and $l = 1$ (right panel). The logarithmic wave-form is calculated for the cases of Schwarzschild (darker blue) and holonomy corrected Schwarzschild with $r_0/r_h = 0.3$ (lighter blue). We also include the respective Prony's fittings (stars for Schwarzschild and inverted triangles for quantum corrected Schwarzschild).

The three phases described in the Sec. 2.4.3 are clearly distinguished in FIG. 2.7. We

highlight that the power-law tail developed at late times seems to be independent of the loop quantum correction.

$l = 0$ (Prony)			$l = 1$ (Prony)		
n	Schwarzschild	$r_0/r_h = 0.3$	n	Schwarzschild	$r_0/r_h = 0.3$
0	$0.2209 - 0.2098i$	$0.2098 - 0.1828i$	0	$0.5858 - 0.1953i$	$0.5823 - 0.1737i$

Table 2.3: Fundamental frequency of scalar perturbations, expressed in $(2M)^{-1}$ units, calculated by the Prony method for $l = 0, 1$. We considered the Schwarzschild BH, as well as the holonomy corrected Schwarzschild BH with $r_0/r_h = 0.3$.

The fundamental modes, obtained from the Prony method, for $l = 0, 1$ are showed in TABLE 2.3. These results can be compared with those of TABLES 2.1 and 2.2. As we can see, both results are in excellent agreement.

2.6 Remarks

Simultaneously with the progress of the BH perturbation theory, the search for a quantum theory of gravity was strongly active. Among several possibilities, the theory of LQG has had many interesting results, namely, the construction of singular-free cosmological and BH solutions [128, 129] and the derivation of the Hawking-Bekenstein entropy [130]. These results might be the smoking guns to a complete and consistent theory of quantum gravity. Nevertheless, there is still a lot of work to be done until we can interpret all LQG results properly. Thus, many effective models have been studied, aiming to obtain effects that one would expect to observe in the complete LQG theory.

We investigated the scalar QNMs of a quantum corrected Schwarzschild BH. We used standard methods of BH perturbation theory, namely, the third order WKB approximation, the continued fraction method (also named as Leaver's method) and the Prony method. In order to perform a consistency check, we compared the numerical results, computed through the three different methods, and obtained an excellent agreement, in the regime of applicability of each method.

We computed the QNMs for different values of the multipole number l and the overtones

n. In particular, we obtained the first 30 overtones for the fundamental mode $l = 0$ and the first 30 overtones for the mode $l = 1$, using the Leaver's method. Our numerical results show that, for a fixed l and n, the quantum corrected Schwarzschild BH perturbations become less damped as we increase the LQG parameter r_0. Moreover, for $l = 0$ and $n > 0$, the QNMs frequencies curves in the complex plane are self intersecting, meaning that two different quantum corrected Schwarzschild BH configurations may have the same QNMs.

Furthermore, we obtained that for middle-to-high values of r_0/r_h, the scalar QNMs of the quantum corrected Schwarzschild BH may have vanishing real part, i.e. it admits purely decaying modes. We remark that purely decaying modes in a classical Schwarzschild BH exist solely for gravitational perturbations [55, 152].

Part III

Black hole imaging

Chapter 3

Light rings, shadows and lensing of a black hole immersed in a swirling universe

3.1 Introduction

The first non-trivial exact solution of the vacuum EFE, published in 1916 by Schwarzschild, describes a spherically symmetric, static and asymptotically flat BH spacetime [23]. Nearly five decades later, its rotating generalization was derived by Kerr [26]. The Kerr solution stands as a cornerstone in BH physics, hypothesized as the metric describing all BHs in equilibrium - see Ref. [154] for a discussion. Moreover, it is also the quintessential solution to learn about rotational effects in GR. Other textbook solutions presenting rotational effects are considered more exotic, such as the Gödel rotating universe [155, 156] and the Taub-NUT spacetime [156–158], which contain, for instance, closed timelike curves that are not cloaked by any horizon. By contrast, the Schwarzschild and Kerr metrics are well behaved outside the event horizon, allowing a well defined initial value problem in the outer domain of communication.

A whole landscape of other exact solutions of the EFE has been derived and cataloged, see *e.g.* Ref. [159], some containing rotational effects. However, imposing *vacuum* is quite restrictive, making Ricci flat geometries of particular interest. The goal of this chapter

is to discuss the behavior of light in a class of vacuum solutions of the EFE describing a Schwarzschild BH immersed in a rotating background with the peculiarity that the north and the south hemispheres spin in opposite directions. This *swirling universe* (SU) [160] introduces no closed time-like curves; in this sense it is less exotic than the Gödel or the Taub-NUT spacetime. Similarly to those, on the other hand, the SU is not asymptotically flat.

The SU was first mentioned in a work by Gibbons, Mujtaba and Pope [161], although its properties were only thoroughly examined in Ref. [160], wherein the Schwarzschild BH in the SU (SBHSU), as well as its Kerr generalization, was constructed by exploiting the Ernst formalism[1].

Here we study the LRs, shadow and gravitational lensing of the SBHSU. As we shall see, the peculiar properties of the SU yield peculiar properties for light propagation, most notably non-equatorial LRs for a single BH spacetime and a BH shadow that is $\mathbb{Z}_2$-odd, rather than the usual $\mathbb{Z}_2$ even, *i.e.* north-south symmetric, when observed from the equatorial plane of the BH spacetime. The remainder of this chapter is organized as follows: In Sec. 3.2 we review some general aspects of the Ernst formalism, which is used to obtain the SBHSU solution. We also revisit the main properties of the SBHSU spacetime. In Sec. 3.3 we study the motion of null geodesics of the SBHSU and define the 2-dimensional effective potentials $H_{\pm}$. We also analyze the LRs structure of the SBHSU, using the techniques developed in Ref. [105]. We note that the SBHSU is not included in the results presented in [104, 105], or any of the other above, due to its peculiar asymptotics. Other related works can be found in Refs. [165, 166]. In Sec. 3.4 we present our results regarding the shadow and gravitational lensing produced by the SBHSU. Finally, in Sec. 3.5 we present some remarks of this chapter.

3.2 The SBHSU spacetime

3.2.1 The Ernst formalism

The Ernst formalism, developed in the 1960s [167, 168], has emerged as a powerful mathematical tool for generating stationary and axisymmetric solutions of GR. This methodology

[1] More recently, new exact solutions involving the SU have been obtained in Refs. [162–164].

proves to be especially valuable when the matter content is solely characterized by the electromagnetic field[2]. The central idea of this formalism lies in rewriting the Einstein-Maxwell (EM) system of equations in terms of the Ernst potentials. The resulting equations, referred to as the Ernst equations, allow for a clearer exploration of the theory's symmetries, thereby facilitating a structured examination of group theoretical aspects of the EM system.

For the stationary vacuum case, Geroch showed that $SU(1,1)$ is the underlying group of symmetries of the Ernst equations [170]. Subsequently, Kinnersley demonstrated that, when generalized for electrovacuum, the corresponding symmetry group linked to the Ernst equations is isomorphic to $SU(2,1)$ [171, 172]. Furthermore, this symmetry group can be explicitly represented through five general transformations. Starting from one known solution, it is possible, through Kinnersley transformations, to generate non-trivial new solutions of the EM theory.

Considering the Schwarzschild BH as a starting point (seed), using the Kinnersley transformations and the conjugation discrete transformation (see Eq. (3.15) below), it is possible to generate several other solutions like: RN, Taub-NUT and the Schwarzschild-Melvin BHs. Following this approach, Astorino, Martelli, and Viganò showed that one can obtain the Schwarzschild and Kerr BHs immersed in a SU [160]. They obtained these BHs solutions by means of the Ehlers transformations. The investigation conducted in Ref. [160] goes beyond the metric derivation and includes also analyses of the horizon embedding, ergoregion, closed timelike curves, conical singularities and geodesics.

Applying the Ernst formalism requires both stationarity and axisymmetry. Stationarity means that there must exist a (asymptotic) timelike Killing vector field ξ; axisymmetry implies another Killing vector field ψ, whose trajectories form closed spacelike curves. We also assume that the two Killing vector fields commute[3], which implies that we have the freedom to select coordinates (t, φ) that are specifically suited to these symmetries. In this

[2]It is hard to implement the Ernst formalism beyond the electrovacuum case of stationary and axisymmetric spacetimes without spoiling the Ernst equation symmetries. Nevertheless, there are a few possible extensions, such as also considering a minimally and conformally coupled scalar field [169].

[3]We remark that in asymptotically flat spacetimes, there is a theorem established by Carter [173] which guarantees the commutation of these two Killing vector fields for asymptotically flat spacetimes. However, we will not consider asymptotically flatness as a hypothesis here.

coordinate system, ξ corresponds to ∂_t, and ψ corresponds to ∂_φ, as established in Ref. [156]. Additionally, the metric components remain independent of these chosen coordinates.

The spacetime to be constructed is a solution of the EM equations, without the inclusion of a cosmological constant. This system of equations is expressed as follows:

$$R_{\mu\nu} - \frac{1}{2}Rg_{\mu\nu} = 2\left(F_{\mu\alpha}F_{\nu}{}^{\alpha} - \frac{1}{4}g_{\mu\nu}F_{\alpha\beta}F^{\alpha\beta}\right), \tag{3.1}$$

$$\partial_\mu\left(\sqrt{-g}F^{\mu\nu}\right) = 0, \tag{3.2}$$

where $R_{\mu\nu}$ is the Ricci tensor and R the Ricci scalar constructed from the metric $g_{\mu\nu}$. The Maxwell-Faraday tensor is represented by $F_{\mu\nu}$ and is defined by the $U(1)$ gauge potential A_μ according to $F_{\mu\nu} = \partial_\mu A_\nu - \partial_\nu A_\mu$. Assuming that the gauge potential inherits the symmetries from the spacetime, we must have $A = A_t dt + A_\varphi d\varphi$.

Within this framework, the most general line element is described bt the Lewis-Weyl-Papapetrou (LWP) metric, given by

$$ds^2 = -f\left(dt - \omega d\varphi\right)^2 + f^{-1}\left[\rho^2 d\varphi^2 + e^{2\gamma}\left(d\rho^2 + dz^2\right)\right]. \tag{3.3}$$

In Eq. (3.3), we have adopted the Weyl canonical coordinates (t, ρ, z, φ), where $z \in (-\infty, \infty)$ and $\rho \in [0, \infty)$. The function ω is associated to the spacetime rotation with respect to the axis $\rho = 0$. By substituting the LWP metric back into the EM system, one may obtain a set of four coupled, partial differential equations for the functions f, ω, A_t and A_φ (see Refs. [174, 175] for more details). The equations for γ decouple from the others, implying that γ is fully determined by the remaining functions.

Let $\mathcal{E}$ and Φ be complex functions representing the Ernst potentials defined according to

$$\Phi = A_t + i\overline{A}_\varphi, \tag{3.4}$$

$$\mathcal{E} = f - |\Phi\Phi^*| + ih, \tag{3.5}$$

where

$$\nabla\overline{A}_\varphi = f\rho^{-1}\hat{e}_\varphi \times (\nabla A_\varphi + \omega\nabla A_t), \tag{3.6}$$

$$\nabla h = -f^2\rho^{-1}\hat{e}_\varphi \times \nabla\omega - 2\mathrm{Im}(\Phi^*\nabla\Phi). \tag{3.7}$$

The operator ∇ in Eqs. (3.6) and (3.7) is the flat vectorial operator associated with the "nonphysical" metric $ds^2 = d\rho^2 + dz^2 + \rho^2 d\varphi^2$, written in cylindrical Weyl coordinates. The vector $\hat{e}_\varphi$ corresponds to the unit vector in the azimuthal direction.

Ernst showed that Eqs. (3.1) and (3.2), assuming the previously mentioned spacetime symmetries, are equivalent to the Ernst equations, which are given by

$$\left(\Re(\mathcal{E}) + |\Phi|^2\right) \nabla^2 \mathcal{E} = (\nabla \mathcal{E} + 2\Phi^* \nabla \Phi) \cdot \nabla \mathcal{E}, \tag{3.8}$$

$$\left(\Re(\mathcal{E}) + |\Phi|^2\right) \nabla^2 \Phi = (\nabla \mathcal{E} + 2\Phi^* \nabla \Phi) \cdot \nabla \Phi. \tag{3.9}$$

The Ernst equations are symmetric under the action of the group $SU(2,1)$, which, following Kinnersley, can be represented by five transformations on the Ernst potentials. The Kinnersley transformations are given by [171, 172]

$$\mathcal{E} \to \mathcal{E}' = \alpha\alpha^* \mathcal{E}\,, \quad \Phi \to \Phi' = \alpha \Phi\,, \tag{3.10}$$

$$\mathcal{E} \to \mathcal{E}' = \mathcal{E} + ib\,, \quad \Phi \to \Phi' = \Phi\,, \tag{3.11}$$

$$\mathcal{E} \to \mathcal{E}' = \frac{\mathcal{E}}{1 + ic\mathcal{E}}\,, \quad \Phi \to \Phi' = \frac{\Phi}{1 + ic\mathcal{E}}\,, \tag{3.12}$$

$$\mathcal{E} \to \mathcal{E}' = \mathcal{E} - 2\beta\Phi - \beta\beta^*\,, \quad \Phi \to \Phi' = \Phi + \beta^*\,, \tag{3.13}$$

$$\mathcal{E} \to \mathcal{E}' = \frac{\mathcal{E}}{1 - 2\gamma^*\Phi - \gamma\gamma^*\mathcal{E}}\,, \quad \Phi \to \Phi' = \frac{\Phi + \gamma\mathcal{E}}{1 - 2\gamma^*\Phi - \gamma\gamma^*\mathcal{E}}\,, \tag{3.14}$$

where $b, c \in \mathbb{R}$ and $\alpha, \beta, \gamma \in \mathbb{C}$. Hence, the aforementioned transformations depend upon 8 arbitrary real parameters, which matches the dimension of $SU(2,1)$[4]. Notably, these transformations map the space of solutions of the EM equations into itself. We remark, however, that Eqs. (3.10), (3.11) and (3.13) lead to trivial transformations, *i.e.* the modifications can be absorbed in gauge transformations of either the metric or the electromagnetic potential. The transformations defined in Eqs. (3.12) and (3.14) are known as Ehlers and Harrison transformations, respectively, and act on the Ernst potential in a non-trivial way, giving rise to nonequivalent spacetimes solutions.

[4]Let $GL(3,\mathbb{C})$ be the general linear group of order 3 over $\mathbb{C}$ and $\eta = \mathrm{diag}(1,1,-1)$. Since $SU(2,1)\{A \in GL(3,\mathbb{C}) | \det A = 1 \wedge A\eta A^\dagger = \eta\}$, the dimension of $SU(2,1)$ must be 8, since we have 18 real free parameters from $GL(3,\mathbb{C})$ that are constrained by 1+9 conditions according to $\det A = 1$ and $A\eta A^\dagger = \eta$, respectively.

3.2.2 Conjugate metrics

There is a property of the LWP metric that is, if (f, ω, γ) constitutes a triple defining a LWP line element that solves the EM system, then there exist $(\overline{f}, \overline{\omega}, \overline{\gamma})$ defining a non-equivalent LWP metric which is also a solution. These triples must be related by a discrete transformation called conjugation, defined by [160, 176]

$$\left\{ f \to \frac{\rho^2}{\overline{f}} - \overline{f}\overline{\omega}^2, \omega \to \frac{\overline{f}^2\overline{\omega}}{\overline{f}^2\overline{\omega}^2 - \rho^2}, e^{2\gamma} \to e^{2\overline{\gamma}}\left(\frac{\rho^2}{\overline{f}^2} - \overline{\omega}^2\right)\right\}. \tag{3.15}$$

After applying the transformation given in Eq. (3.15), one may obtain the metric

$$d\overline{s}^2 = -\overline{f}\left(d\varphi - \overline{\omega}dt\right)^2 + \overline{f}^{-1}\left[\rho^2 dt^2 + e^{2\overline{\gamma}}\left(d\rho^2 + dz^2\right)\right]. \tag{3.16}$$

The two LWP metrics correspondent to Eqs. (3.3) and (3.16), related by Eq. (3.15), are called conjugate metrics.

The combination of Kinnersley transformations obtained from the Ernst formalism, together with the conjugation operation, enables one to obtain a total of five non-equivalent metrics from only one seed. In Ref. [160] the authors refer to the metric of Eq. (3.3) as electric LWP metric, whereas the metric of Eq. (3.16) is referred to as magnetic LWP metric. In Fig. 3.1 we display all solutions that can be generated starting with Schwarzschild spacetime as a seed.

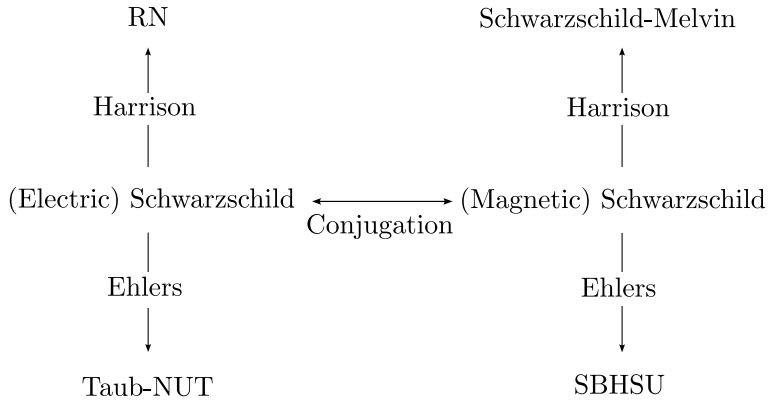

Figure 3.1: Schematic representation of the metrics generated from Schwarzschild spacetime using conjugation and Kinnersley transformations.

From the electric version of Schwarzschild metric we may obtain RN (Taub-NUT) by means of a Harrison (Ehlers) transformation. If, instead, we first conjugate the Schwarzschild

solution to obtain the magnetic version of the Schwarzschild BH, it is possible to generate the Schwarzschild-Melvin (SBHSU) metric through a Harrison (Ehlers) transformation.

3.2.3 The metric

As discussed in the previous subsection, the SBHSU spacetime can be obtained by means of an Ehlers transformation on the magnetic Schwarzschild solution. It is an algebraically general, stationary, axially symmetric and non-asymptotically flat BH solution of the vacuum EFE. Its line element can be written as

$$\begin{aligned} ds^2 = F(r,\theta)\left[-f(r)dt^2 + \frac{dr^2}{f(r)} + r^2 d\theta^2 \right] + \frac{r^2 \sin^2\theta}{F(r,\theta)} \times \\ \left\{ d\varphi + [4jrf(r)\cos\theta]\, dt \right\}^2, \end{aligned} \tag{3.17}$$

with

$$f(r) = 1 - \frac{2M}{r}, \tag{3.18}$$

$$F(r,\theta) = 1 + j^2 r^4 \sin^4\theta. \tag{3.19}$$

For stationary, axisymmetric and asymptotically flat BH spacetimes, the central object mass and angular momentum may be defined via Komar integrals [177]. These integrals are given by

$$M_{\text{Komar}} = -\frac{1}{8\pi} \lim_{r\to\infty} \int_{\mathbb{S}^2} \star d\xi^\flat, \tag{3.20}$$

$$J_{\text{Komar}} = \frac{1}{16\pi} \lim_{r\to\infty} \int_{\mathbb{S}^2} \star d\psi^\flat, \tag{3.21}$$

where $\mathbb{S}^2$ represents a topological spherical 2-surface, $\star$ is the Hodge star operator and $\flat$ is the musical isomorphism [178].

For non-asymptotically flat spacetimes, even if the Komar integrals can be defined, their physical interpretation is no longer straightforward. For the SBHSU, on $\mathbb{S}^2$, we have

$$\begin{aligned} \star d\xi^\flat = r^2 \sin\theta \Bigg[\frac{4j^2 r^3 f(r) \sin^2 2\theta}{F(r,\theta)^2} \left(f(r) + r f'(r) \right) \\ - f(r) \frac{\partial_r F(r,\theta)}{F(r,\theta)} - f'(r) \Bigg] d\theta \wedge d\varphi, \end{aligned} \tag{3.22}$$

$$\star d\psi^{\flat} = \frac{4jr^4 \sin^3\theta\cos\theta\,(rf'(r)+f(r))}{F(r,\theta)^2} d\theta\wedge d\varphi, \tag{3.23}$$

which, after the integration over $\mathbb{S}^2$, results in

$$M_{\text{Komar}} = M, \qquad J_{\text{Komar}} = 0. \tag{3.24}$$

This calculation shows that M can be heuristically interpreted as the BH mass and the total angular momentum is zero. Although $J_{\text{Komar}} = 0$, the space is not static (see Sec. 3.2.4). The Authors in Ref. [160] obtained the same result using the canonical integrability method.

When $j = 0$, the SBHSU metric simplifies to the Schwarzschild solution, and when $M = 0$, it reduces to the SU, whose line element can be expressed as

$$ds^2 = (1+j^2\rho^4)(-dt^2+d\rho^2+dz^2) + \frac{\rho^2}{1+j^2\rho^4}(d\varphi+4jzdt)^2, \tag{3.25}$$

where we have written Eq. (3.25) in cylindrical coordinates

$$\rho = r\sin\theta, \qquad z = r\cos\theta. \tag{3.26}$$

The parameter j is associated with the background spacetime rotation.

The SBHSU is not plagued with geometric pathologies such as conical singularities, nor causality violation due to closed timelike curves [160]. Nevertheless, the SBHSU solution has a singularity at $r = 2M$ and $r = 0$, inherited from the Schwarzschild BH. The former is a coordinate singularity and defines the location of the event horizon, whereas the latter cannot be removed by a change of coordinates, since the curvature invariant, given by

$$R_{\mu\nu\alpha\beta}R^{\mu\nu\alpha\beta} = \frac{\mathcal{F}(r,\theta)}{r^6}, \tag{3.27}$$

diverges as $r \to 0$, for all $\theta \in (0,\pi)$, indicating that the spacetime is, indeed, singular. The function $\mathcal{F}(r,\theta)$ is a lengthy expression in terms of the coordinates r and θ (which we choose not to show explicitly in this work) that satisfies $\lim_{r\to 0}\mathcal{F}(r,\theta) = 48M^2$.

On the other hand, the background spacetime defined by Eq. (3.25) is everywhere regular, as it can be shown by setting $M = 0$ in Eq. (3.27), obtaining

$$R_{\mu\nu\alpha\beta}R^{\mu\nu\alpha\beta}|_{M=0} = \frac{192j^2\,(j^6\rho^{12}-15j^4\rho^8+15j^2\rho^4-1)}{(j^2\rho^4+1)^6}. \tag{3.28}$$

In Fig. 3.2 we plot the Kretschmann scalar, setting $\theta = \pi/2$, for SU and SBHSU spacetimes. In both cases, the curvature scalar tends to zero as $r \to \infty$; however, while $|R_{\mu\nu\alpha\beta}R^{\mu\nu\alpha\beta}| < \infty$ as $r \to 0$ for the SU, the Kretschmann scalar diverges for the SBHSU.

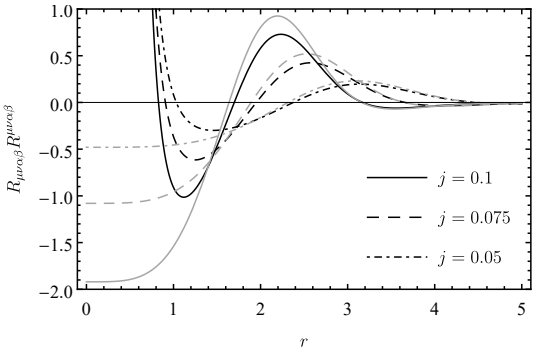

Figure 3.2: Kretschmann scalar of the SU (gray) and SBHSU (black) spacetimes, for $\theta = \pi/2$ and $j = 0.05,\ 0.075,\ 0.1$. For the BH cases we have set $M = 0.1$ and $\theta = \pi/2$.

3.2.4 Ergoregion

This solution also possesses an ergoregion, implicitly defined by $g_{tt}(r, \theta) = 0$ (excluding the surface $r = 2M$) [160, 179]. We consider the g_{tt} metric component as a function $g_{tt} : \mathbb{R}^3 \to \mathbb{R}$, where r and θ are the usual spherical polar coordinates in $\mathbb{R}^3$. Let $\{x, y, z\}$ be the rectangular coordinates in $\mathbb{R}^3$. We plot in Fig. 3.3 the cross-section through the surface $y = 0$ of the surface $g_{tt}(r, \theta) = 0$ (which is not an isometric embedding).

The ergosurface is defined by 2 disconnected patches, namely: the two non-compact branches above and below the BH. The direction of the frame-dragging can be inferred from

$$\frac{d\phi}{dt} = -\frac{g_{t\varphi}}{g_{\varphi\varphi}} = -4j(r - 2M)\cos\theta\,. \tag{3.29}$$

Therefore, inside the top (bottom) branch, as well as in the region inside the BH, below (above) the equatorial plane, observers must rotate in the negative (positive) direction. The sense of rotation is also indicated in Fig. 3.3 by + (−) sign if it is positively (negatively) oriented. The opposite spin directions of the north and south is what renders the zero angular momentum obtained in Sec. 3.2.3. Similar to the SBHSU case, the RN-Melvin solution also has a non-compact ergoregion [161].

We remark that the Killing vector $\xi = \partial_t$ is asymptotically timelike in the sense that $g_{tt}(r, \theta) \underset{r\to\infty}{\approx} -j^2 r^4 \sin^4\theta$. This quantity is negative for every $\theta \in (0, \pi)$, but tends to zero when $\theta \to 0$ or $\theta \to \pi$. Hence, in the vicinity of the symmetry axis, ξ may lose its timelike character [160]. This serves as an indicator of the presence of a non-compact ergoregion in

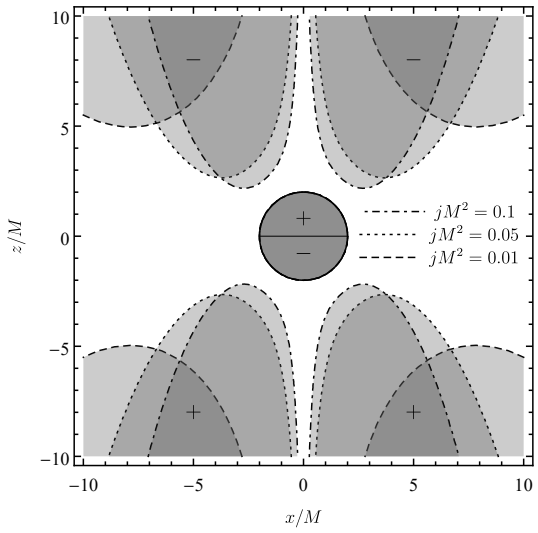

Figure 3.3: Representation of the surface $g_{tt}(r,\theta) = 0$ in the section $y = 0$ of the 3-dimensional Euclidean space, for $jM^2 = 0.01, 0.05, 0.1$. As the parameter of the swirling background increases, the ergosurface gets closer to the horizon surface.

the vicinity of the rotational axis.

3.2.5 Horizon geometry

The geometry of the event horizon is defined by Eq. (3.17) restricted to the 2-surface $t =$constant and $r = 2M$, from where we obtain

$$ds^2|_{\substack{r=2M \\ t=\text{const}}} = 4M^2 F(2M,\theta)d\theta^2 + \frac{4M^2\sin^2\theta}{F(2M,\theta)}d\varphi^2. \tag{3.30}$$

For a two-dimensional surface embedded in a three-dimensional space, the Gaussian curvature K is defined as the product of the principal curvatures k_1 and k_2 at each point. The principal curvatures represent the maximum and minimum curvatures in orthogonal directions on the surface. In our case, the two principal directions are $\{\theta, \varphi\}$ and we will represent the corresponding principal curvatures by $\{k_\theta, k_\varphi\}$, respectively. From Eq. (3.30) we can compute the Gaussian curvature [180]

$$\begin{aligned} K &= -\frac{1}{2\sqrt{\det(g_{\mu\nu})}}\frac{\partial}{\partial\theta}\left(\frac{\partial_\theta g_{\varphi\varphi}}{\sqrt{\det(g_{\mu\nu})}}\right) \\ &= \frac{\mathcal{K}(\theta)}{4M^2(1+16j^2M^4\sin^4\theta)^3}, \end{aligned} \tag{3.31}$$

where $g_{\mu\nu}$ are the metric components of Eq. (3.30) and

$$\mathcal{K}(\theta) = 1 + 48j^2M^4\sin^2 2\theta - 1024j^4M^8\sin^6\theta\cos^2\theta - 256j^4M^8\sin^8\theta. \tag{3.32}$$

One key significance of the Gaussian curvature lies in its classification of different types of surfaces regarding its sign. By examining the signs and values of the Gaussian curvature at various points on a surface, we can identify whether the surface is flat/parabolic[5], positively or negatively curved. One can show that, for all $j > 0$, $\theta = \pi/2$ corresponds to a global minimum of K, where it is evaluated to

$$K|_{\theta=\pi/2} = \frac{1 - 16j^2M^4}{4M^2\left(1 + 16j^2M^4\right)^2}. \tag{3.33}$$

Therefore, for $j < 1/4M^2$ the Gaussian curvature is always positive. If we set $j = 1/4M^2$, the Gaussian curvature is zero at the equatorial plane. If j is greater than this critical value, then K is negative on a neighborhood of $\theta = \pi/2$. Since k_φ is always positive due to axisymmetry, k_θ must be negative in a neighborhood of $\theta = \pi/2$ for $j > 1/4M^2$.

We can classify the horizon geometry according to the sign of the Gaussian curvature in the following way [180]:

- $j < 1/4M^2$: Globally elliptic;
- $j = 1/4M^2$: Everywhere elliptic, except at the equator, where it is parabolic;
- $j > 1/4M^2$: Locally elliptic at the poles and locally hyperbolic at the equator.

In Fig. 3.4 we plot the isometric embedding for $jM^2 = 0, 1/4, 1/2$, specifying where K is zero (negative) by points (continuous lines). The dashed, dot dashed and dotted lines represent points where K is greater than zero.

Another way to deduce the horizon local hyperbolic geometry at equator for $j > 1/4M^2$

[5]In both flat and parabolic points, the Gaussian curvature vanishes, but in flat spaces both principal curvatures are zero, whereas in parabolic points just one of the principal curvatures is zero. An example of a surface with parabolic points is the surface of a cylinder.

is to calculate the proper length

$$\begin{aligned} L(\theta) &= \int_0^{2\pi} \sqrt{g_{\varphi\varphi}(r,\theta)}|_{r\to 2M} d\varphi \\ &= 2\pi \sqrt{\frac{4M^2 \sin^2\theta}{1+16j^2M^4\sin^4\theta}}\,, \end{aligned} \tag{3.34}$$

which represents the horizon perimetral length at a fixed value of θ.

For every compact, globally elliptic and $\mathbb{Z}_2$ symmetric surface contained in $\mathbb{R}^3$, the length $L(\theta)$ attains its maximum at $\theta = \pi/2$. This holds true for $j < 1/4M^2$. However, as we extend to $j > 1/4M^2$, the point $\theta = \pi/2$ transitions to a local minimum of $L(\theta)$, while the points $\arcsin\sqrt{1/4jM^2}$ and $\pi - \arcsin\sqrt{1/4jM^2}$ become maxima.

The existence of an elliptic portion on the horizon geometry is expected, since every compact surface embedded in $\mathbb{R}^3$ has, at least, one elliptical point [180]. Thus, either the horizon surface is purely elliptical or there exists a region where it can be hyperbolic. In the Kerr case, for high enough values of the dimensionless rotation parameter ($a/M > \sqrt{3}/2$), there are regions where the horizon surface is hyperbolic, namely, in a neighborhood of the poles. In the vicinity of those points, the isometric embedding into the Euclidean 3-space is not realizable. Generically, any $U(1)$-symmetric $2d$-surface with negative Gaussian curvature at fixed points of a $U(1)$ symmetry cannot be globally embedded into Euclidean 3-space [181]. In the case of SBHSU, the negative curvature regions are not vicinities of the poles, hence, the previous theorem does not apply. In fact, the global embedding exists for all values of j.

Although the horizon gets deformed with increasing j, the horizon area $\mathcal{A}$ does not change, *i.e.* the area of the Schwarzschild BH $\mathcal{A} = 16\pi M^2$ is preserved, regardless of j.

3.3 LRs in the SBHSU (and SU) spacetimes

3.3.1 Null geodesics

We now study null geodesics on the SBHSU. We adopt the Hamiltonian formalism. In order to do so, we consider the Hamiltonian function $\mathscr{H}$,

$$\mathscr{H} = \frac{1}{2} g^{\mu\nu} p_\mu p_\nu = 0, \tag{3.35}$$

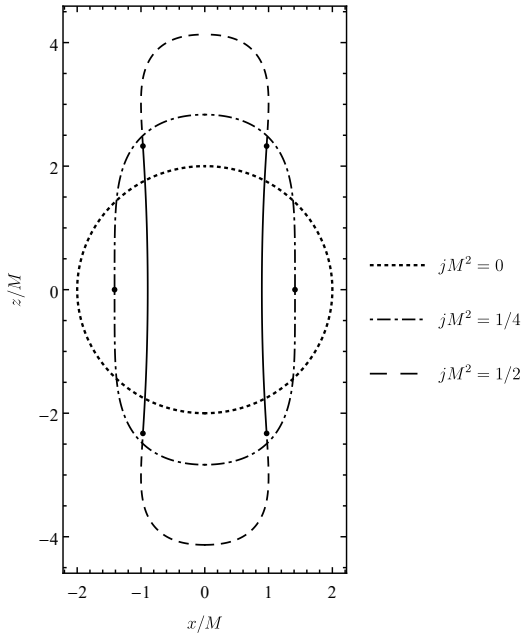

Figure 3.4: Isometric embedding of the horizon into the 3-dimensional Euclidean space, for $jM^2 = 0, 1/4, 1/2$. As the parameter of the swirling background increases, the horizon gets more prolate and thinner along the equator.

where p_μ is the 4-momentum of the photon. The corresponding Hamilton's equations are given by

$$\dot{x}^\mu = \frac{\partial \mathscr{H}}{\partial p_\mu}, \tag{3.36}$$

$$\dot{p}_\mu = -\frac{\partial \mathscr{H}}{\partial x^\mu}. \tag{3.37}$$

In Eqs. (3.36) and (3.37) the dots stands for derivatives with respect to an affine parameter.

As discussed in Sec. 3.2.1, the SBHSU admits two Killing vectors fields, namely, ∂_t and ∂_φ. These vectors are responsible for generating the isometries governing time translation and rotation around the symmetry axis, respectively. The existence of the two Killing vectors also implies the existence of two quantities, defined by

$$E = -(\partial_t)^\mu p_\mu = -p_t, \tag{3.38}$$

$$L = (\partial_\varphi)^\mu p_\mu = p_\varphi, \tag{3.39}$$

which are conserved along the direction of the geodesics.

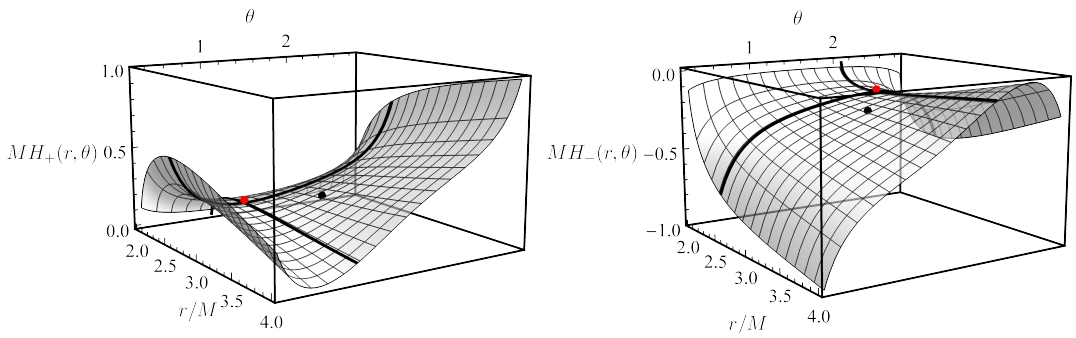

Figure 3.5: 3D plot representations showing the potentials $\mathcal{H}_{+}^{\mathrm{SBHSU}}$ (left panel) and $\mathcal{H}_{-}^{\mathrm{SBHSU}}$ (right panel), as a function of the (r,θ) coordinates for $M^2 j = 0.05$. The critical points for both $\mathcal{H}_{\pm}^{\mathrm{SBHSU}}$ are highlighted in red, while the Schwarzschild LR locations are denoted by black points.

The Hamiltonian can be separated into a kinetic term T plus a potential V, according to

$$\mathscr{H} = T + V, \tag{3.40}$$

where

$$T = g^{rr}(p_r)^2 + g^{\theta\theta}(p_\theta)^2, \tag{3.41}$$

$$V = \frac{L^2 F(r,\theta)}{r^2 \sin^2\theta} - \frac{\left(4jrf(r)L\cos\theta + E\right)^2}{f(r)F(r,\theta)}. \tag{3.42}$$

It is possible to define potentials $\mathcal{H}_{\pm}^{\mathrm{SBHSU}}$, which do not depend on the conserved quantities E and L. Such potentials are given by

$$\mathcal{H}_{\pm}^{\mathrm{SBHSU}}(r,\theta) = \pm\frac{\sqrt{f(r)}F(r,\theta)}{r\sin\theta} - 4jrf(r)\cos\theta, \tag{3.43}$$

and are related with V by

$$V = -\frac{L^2}{f(r)F(r,\theta)}\left(\frac{E}{L} - \mathcal{H}_{+}^{\mathrm{SBHSU}}\right)\left(\frac{E}{L} - \mathcal{H}_{-}^{\mathrm{SBHSU}}\right). \tag{3.44}$$

In Fig. 3.5 we illustrate the null geodesic potentials $\mathcal{H}_{\pm}^{\mathrm{SBHSU}}$.

We remark that the potentials $\mathcal{H}_{\pm}^{\mathrm{SBHSU}}(r,\theta)$, defined in Eq. (3.43) satisfy

$$\mathcal{H}_{\pm}(r,\theta) = -\mathcal{H}_{\mp}^{\mathrm{SBHSU}}(r,\pi-\theta), \tag{3.45}$$

which implies that the potential $\mathcal{H}_{-}^{\mathrm{SBHSU}}$ can be fully constructed from $\mathcal{H}_{+}^{\mathrm{SBHSU}}$ and vice-versa.

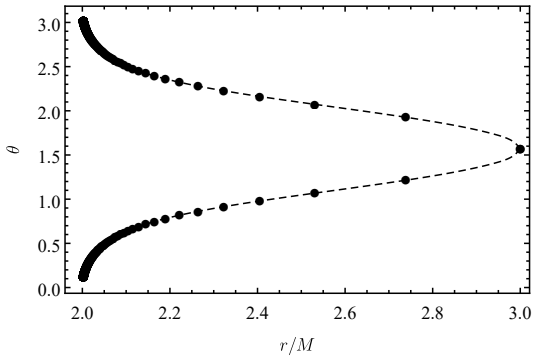

Figure 3.6: LR position on the (r, θ)-plane for various values of the rotation parameter j. We considered a sequence of values of j defined by $j = 0.025 \times n$ for $n \in \mathbb{N}$. The sequence starts at $j = 0$, for which the LR is located at $(3M, \pi/2)$, and for $j \to \infty$ the LR positions go to $(2M, 0)$ and $(2M, \pi)$ in the used coordinate system, which, albeit not geometrically invariant, clearly shows the off-equatorial displacement of the LRs with increasing j.

3.3.2 Topological charge

We now inspect the LRs of the SBHSU. By definition, LRs are critical points of the potential V defined in Eq. (3.44). In Ref. [104] it was shown that critical points of V are also critical points of $\mathcal{H}_{\pm}^{\mathrm{SBHSU}}$. The critical points $(r_{\pm}, \theta_{\pm})$ of $\mathcal{H}_{\pm}^{\mathrm{SBHSU}}$ for the SBHSU with $jM^2 = 0.05$, are displayed in Fig. 3.5 as red points, whereas the black points represent the Schwarzschild LR position. This spacetime exhibits the unusual characteristic of having a LR outside the equatorial plane, *i.e.* $\theta_{\pm} \neq \pi/2$. The absence of $\mathbb{Z}_2$ symmetry causes the Schwarzschild LR - which is the same for both circulation directions - to move in the θ-direction either upwards or downwards, depending on the photon's circulation direction. Consequently, the Schwarzschild LR splits into two separate LRs: one positioned above the equatorial plane and another below it. A similar effect was reported to occur in the Taub-NUT solution [109], and Kerr BHs surrounded by plasma [182].

In Fig. 3.6 we display the LR position as we increase the value of the background rotation parameter j. The point on the far right of Fig. 3.6 corresponds to the Schwarzschild LR. As we increase j, the LR split into two, one for each potential $\mathcal{H}_{\pm}^{\mathrm{SBHSU}}$, such that $\theta_+ < \pi/2$ ($\theta_- > \pi/2$) is associated with $\mathcal{H}_{+}^{\mathrm{SBHSU}}$ ($\mathcal{H}_{-}^{\mathrm{SBHSU}}$). The points $(2M, 0)$ and $(2M, \pi)$ in the (r, θ)-space are accumulation points of the sequence presented in Fig. 3.6.

The result presented in Fig. 3.6 is in accordance with Eq. (3.45), which implies that if (r, θ) is a critical point of $\mathcal{H}_{+}^{\mathrm{SBHSU}}$, then $(r, \pi - \theta)$ must be a critical point of $\mathcal{H}_{-}^{\mathrm{SBHSU}}$. Hence, if (r, θ) corresponds to a LR position such that $\theta \neq \pi/2$, then there must exist another LR with the same radius, separated from the former by one θ-reflection with respect to the equator. These two LRs also must share the same stability properties.

We remark that the correspondence between the labels $\pm$ of the potentials $\mathcal{H}_{\pm}^{\mathrm{SBHSU}}$ and the rotation sense requires careful analysis. In the case of Kerr, for instance, there exists two LRs that counter rotate in relation to each other. Due to the single direction of rotation in Kerr spacetime, one LR must co-rotate with the BH, while the other counter rotates. The SBHSU spacetime similarly accommodates two counter rotating LRs, but both of them co-rotate locally with the spacetime, as can be inferred from Eq. (3.29).

A powerful technique to determine whether there are LRs in a given spacetime was developed in Ref. [105]. This technique consists of calculating a topological charge (TC) obtained from the circulation integral of the gradient of the potentials $\mathcal{H}_{\pm}^{\mathrm{SBHSU}}$. The sign of the TC defines the stability of the corresponding LR. It was shown that any stationary, axially symmetric, circular and asymptotically flat BH spacetime must have a TC equal to -1 for each $\mathcal{H}_{\pm}^{\mathrm{SBHSU}}$, indicating the existence of at least one unstable LR associated with each potential.

Given that the SBHSU is not asymptotically flat, it falls outside the scope of the theorem proved in Ref. [105]. Our task now is therefore to evaluate the TC for this case. We choose to work with the Weyl coordinate system defined by

$$\rho = \sqrt{r^2 - 2Mr}\sin\theta, \tag{3.46}$$

$$z = (r - M)\cos\theta \ . \tag{3.47}$$

The Weyl coordinates reduce to cylindrical coordinates in the asymptotic limit. In these coordinates, the horizon is located at $\rho = 0$ and $|z| < M$. The axis of symmetry is determined by $\rho = 0$ and $|z| > M$. The remaining exterior region is defined by $\rho > 0$.

The SBHSU metric in Weyl coordinates is given by

$$\begin{aligned} ds^2 = & \frac{F(r,\theta)}{f(r)+\left(M^2\sin^2\theta\right)/r^2}\left(d\rho^2+dz^2\right) \\ & -f(r)F(r,\theta)dt^2+\frac{r^2\sin^2\theta}{F(r,\theta)}\Big\{d\varphi+\left[4jrf(r)\cos\theta\right]dt\Big\}^2, \end{aligned} \tag{3.48}$$

where the quantities r and θ in Eq. (3.48) are to be understood as functions of ρ and z, implicitly defined by Eqs. (3.46) and (3.47). Let $\mathbf{v}_{\pm}^{\mathrm{SBHSU}}$ be the vector fields defined by

$$\mathbf{v}_{\pm}^{\mathrm{SBHSU}} = \left(\frac{1}{\sqrt{g_{\rho\rho}}}\frac{\partial\mathcal{H}_{\pm}^{\mathrm{SBHSU}}}{\partial\rho}, \frac{1}{\sqrt{g_{zz}}}\frac{\partial\mathcal{H}_{\pm}^{\mathrm{SBHSU}}}{\partial z}\right) = \left(\mathrm{v}_{\rho,\pm}^{\mathrm{SBHSU}}, \mathrm{v}_{z,\pm}^{\mathrm{SBHSU}}\right). \tag{3.49}$$

The explicit expression of these vector fields, even in terms of the coordinates (r,θ), is too lengthy and we choose not to show it here.

We can write each component of the vector fields as

$$\mathrm{v}_{\rho,\pm}^{\mathrm{SBHSU}} = |\mathbf{v}_{\pm}^{\mathrm{SBHSU}}|\cos\Omega(\rho,z), \tag{3.50}$$

$$\mathrm{v}_{z,\pm}^{\mathrm{SBHSU}} = |\mathbf{v}_{\pm}^{\mathrm{SBHSU}}|\sin\Omega(\rho,z), \tag{3.51}$$

where $|\mathbf{v}_{\pm}^{\mathrm{SBHSU}}| = \sqrt{(\mathrm{v}_{\rho,\pm}^{\mathrm{SBHSU}})^2+(\mathrm{v}_{z,\pm}^{\mathrm{SBHSU}})^2}$ is the norm of $\mathbf{v}_{\pm}^{\mathrm{SBHSU}}$ and Ω is the angle formed by $\mathbf{v}_{\pm}^{\mathrm{SBHSU}}$ and the horizontal axis parametrized by $\mathrm{v}_{\rho,\pm}^{\mathrm{SBHSU}}$.

Let $\mathscr{C}$ be the homotopy class of (simple) curves in the (ρ,z)-space homotopic to the circle. The TC w is a map $w:\mathscr{C}\to\mathbb{Z}$, defined to be

$$w_C = \frac{1}{2\pi}\oint_C d\Omega, \tag{3.52}$$

where $C\in\mathscr{C}$. Eq. (3.52) represents the winding number of the vector fields $\mathbf{v}_{\pm}^{\mathrm{SBHSU}}$ along some curve C in the homotopy class $\mathscr{C}$ defined over the (ρ,z)-space.

Each LR enclosed by C contributes to the TC by ±1. Therefore, w_C is a homotopic invariant if the number of LRs inside C does not change. LRs with $w=-1$ are unstable, whereas LRs with $w=1$ are stable.

To calculate the total TC, one must consider a curve C, as defined in Eq. (3.52), that encompasses all the LRs. Hence, despite the complexity of the vector fields $\mathbf{v}_{\pm}^{\mathrm{SBHSU}}$ components in terms of the coordinates (ρ,z), determining the TC only requires an analysis of its behavior in asymptotic regions, namely, near the horizon, the axis, and at infinity.

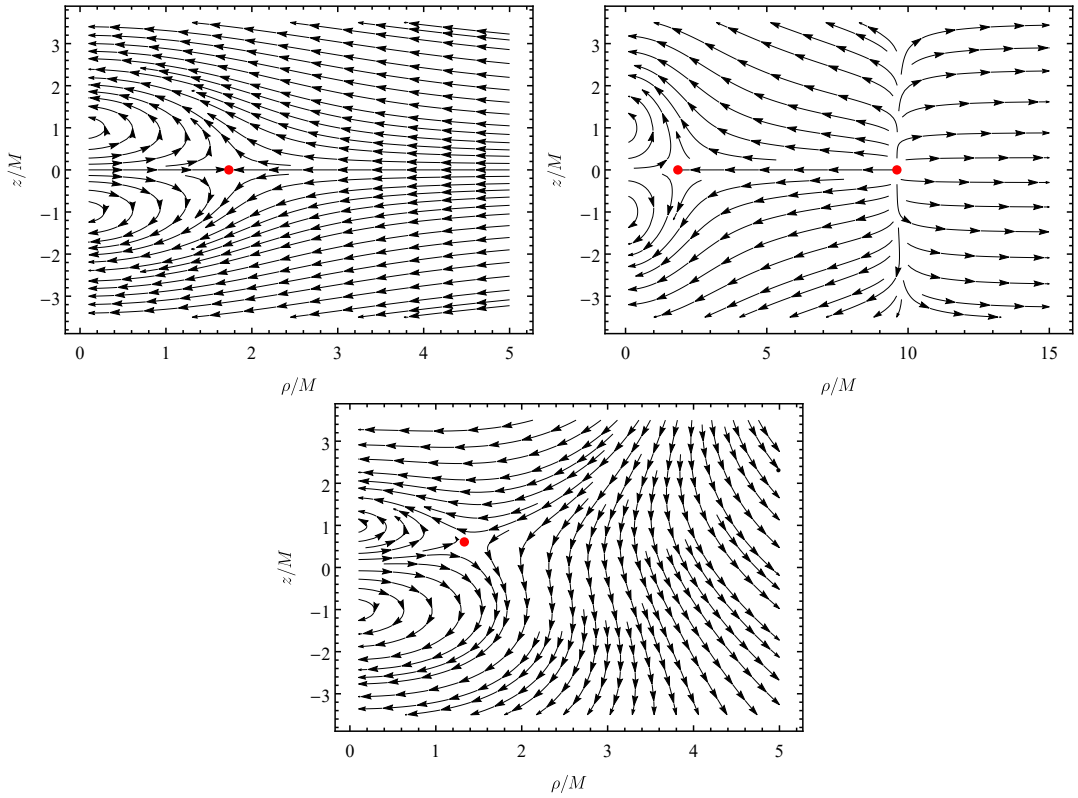

Figure 3.7: Vector field $\mathbf{v}_{+}^{\mathrm{SBHSU}} = (\mathrm{v}_{\rho,+}^{\mathrm{SBHSU}}, \mathrm{v}_{z,+}^{\mathrm{SBHSU}})$ in the $(\rho/M, z/M)$-plane for the Schwarzschild BH (top), Schwarzschild-Melvin BH with $BM = 0.1$ (middle) and SBHSU with $jM^2 = 0.025$ (bottom). The red points represent the location of the LRs of the corresponding spacetime.

The vector plot of the $\mathbf{v}_{+}^{\mathrm{SBHSU}} = \{\mathrm{v}_{\rho,+}^{\mathrm{SBHSU}}, \mathrm{v}_{z,+}^{\mathrm{SBHSU}}\}$ field in terms of the Weyl coordinates can be seen in Fig. 3.7. It suffices to restrict our analysis to $\mathbf{v}_{+}^{\mathrm{SBHSU}}$, since we can always derive the conclusions for $\mathbf{v}_{-}^{\mathrm{SBHSU}}$ by means of Eq. (3.45).

In Fig. 3.7 we compare the vector field $\mathbf{v}_{+}^{\mathrm{SBHSU}}$ of SBHSU with Schwarzschild spacetime and also with Schwarzschild BH immersed in the Melvin universe. The qualitative behavior of the vector field $\mathbf{v}_{+}^{\mathrm{SBHSU}}$ near the horizon and close to the axis is similar for all the three cases. The primary distinction between Schwarzschild, Schwarzschild-Melvin and SBHSU arises in the asymptotic region. The Melvin and SU asymptotics result in a positive asymptotic value for $\mathrm{v}_{\rho,+}^{\mathrm{SBHSU}}$, whereas it is negative for asymptotically flat spacetimes. Nevertheless, the vector fields $\mathbf{v}_{+}^{\mathrm{SBHSU}}$ of Schwarzschild-Melvin and SBHSU are different for $z \gg 1$, namely, the vector fields turns in different directions to flip the sign of $\mathrm{v}_{\rho,+}^{\mathrm{SBHSU}}$. This difference will

have a decisive impact on the TC of SBHSU, when compared to Schwarzschild-Melvin.

Given a real number $\xi > 0$, the total TC is computed by considering a curve $C = \bigcup_{k=1}^{6} C_k$. In this arrangement, the z coordinate of the paths C_1 and C_3 is fixed at $-M\xi$ and $M\xi$, respectively. Meanwhile, for the other paths C_2 and the combination $C_4 \cup C_5 \cup C_6$, the radial coordinate ρ is fixed at $M\xi$ and M/ξ, respectively (see Fig. 3.8).

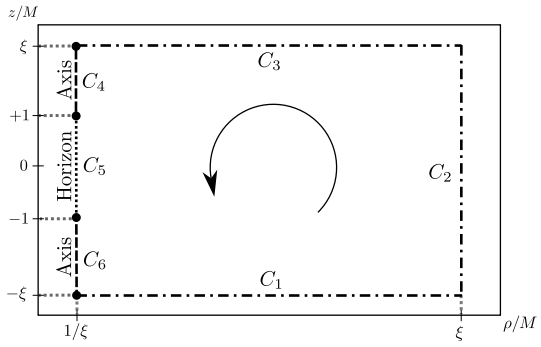

Figure 3.8: Schematic representation of the contour C, enclosing a compact region outside the horizon in the (ρ, z)-plane. The region inside the curve C is designed to encompass all of the spacetime outside the horizon as $\xi \to \infty$.

Thus, we can separate the integral of Eq. (3.52) into six pieces, according to

$$2\pi w_C = \mathcal{I}_1 + \mathcal{I}_2 + \mathcal{I}_3 + \mathcal{I}_4 + \mathcal{I}_5 + \mathcal{I}_6, \tag{3.53}$$

where

$$\mathcal{I}_1 = \left[\int_{M/\xi}^{M\xi} \frac{d\Omega}{d\rho} d\rho\right]_{z=-M\xi}, \tag{3.54}$$

$$\mathcal{I}_2 = \left[\int_{-M\xi}^{M\xi} \frac{d\Omega}{dz} dz\right]_{\rho=M\xi}, \tag{3.55}$$

$$\mathcal{I}_3 = \left[\int_{M\xi}^{M/\xi} \frac{d\Omega}{d\rho} d\rho\right]_{z=M\xi}, \tag{3.56}$$

$$\mathcal{I}_4 = \left[\int_{M\xi}^{M} \frac{d\Omega}{dz} dz\right]_{\rho=M/\xi}, \tag{3.57}$$

$$\mathcal{I}_5 = \left[\int_{M}^{-M} \frac{d\Omega}{dz} dz\right]_{\rho=M/\xi}, \tag{3.58}$$

$$\mathcal{I}_6 = \left[\int_{-M}^{-M\xi} \frac{d\Omega}{dz} dz\right]_{\rho=M/\xi}. \tag{3.59}$$

Hence, the total TC in the exterior region of the BH is given by the limit

$$w = \lim_{\xi \to \infty} w_C. \tag{3.60}$$

The composite curve formed by $C_4 \cup C_6$ represents the axis limit, while C_5 denotes the horizon limit. Additionally, the path formed by the combination $C_1 \cup C_2 \cup C_3$ corresponds to the asymptotic limit.

In order to compute the integrals presented in Eqs. (3.54)-(3.59), it is necessary to ensure that the associated angle Ω, within each path C_k, falls within the valid range for the inverse trigonometric functions arccos and arcsin. Thus, Ω must belong, along each path C_k, to one of the following four intervals: $(\pi/2, -\pi/2)$, $(\pi/2, 3\pi/2)$, $(0, \pi)$, or $(-\pi, 0)$.

For each of the four possibilities, Ω is calculated inverting Eqs. (3.50) and (3.51) according to

$$\text{if } \Omega \in (\pi/2, -\pi/2): \ \Omega = \arcsin\left(\frac{\mathrm{v}_{z,\pm}^{\mathrm{SBHSU}}}{|\mathbf{v}_{\pm}^{\mathrm{SBHSU}}|}\right), \tag{3.61}$$

$$\text{if } \Omega \in (\pi/2, 3\pi/2): \ \Omega = \pi - \arcsin\left(\frac{\mathrm{v}_{z,\pm}^{\mathrm{SBHSU}}}{|\mathbf{v}_{\pm}^{\mathrm{SBHSU}}|}\right), \tag{3.62}$$

$$\text{if } \Omega \in (0, \pi): \ \Omega = \arccos\left(\frac{\mathrm{v}_{\rho,\pm}^{\mathrm{SBHSU}}}{|\mathbf{v}_{\pm}^{\mathrm{SBHSU}}|}\right), \tag{3.63}$$

$$\text{if } \Omega \in (-\pi, 0): \ \Omega = -\arccos\left(\frac{\mathrm{v}_{\rho,\pm}^{\mathrm{SBHSU}}}{|\mathbf{v}_{\pm}^{\mathrm{SBHSU}}|}\right). \tag{3.64}$$

For any of the four possibilities, the integrals $\mathcal{I}_k$ are calculated by substituting Ω for the formulae given in Eqs. (3.61)-(3.64), evaluated at the corresponding integration limits.

Asymptotic limit

In the asymptotic limit we have to calculate the Integrals $\mathcal{I}_1$, $\mathcal{I}_2$ and $\mathcal{I}_3$. Starting with the integral $\mathcal{I}_1$, we have $z = -M\xi \to -\infty$, where the vector field $\mathbf{v}_{+}^{\mathrm{SBHSU}}$ can be approximated as:

$$\mathrm{v}_{\rho,+}^{\mathrm{SBHSU}} \approx -\frac{1 - 3j^2\rho^4}{\rho^2\sqrt{1 + j^2\rho^4}} + \mathcal{O}(\xi^{-1}), \tag{3.65}$$

$$\mathrm{v}_{z,-}^{\mathrm{SBHSU}} \approx -\frac{4j}{\sqrt{1 + j^2\rho^4}} + \mathcal{O}(\xi^{-1}), \tag{3.66}$$

with higher-order terms represented by $\mathcal{O}(\xi^{-1})$. In this part of the integration, the corresponding angle Ω will be denoted by $\Omega_{z\to-\infty}$.

Since the z-component, $\mathrm{v}_{z,+}^{\mathrm{SBHSU}}$, is negative ($\mathrm{v}_{z,+}^{\mathrm{SBHSU}} < 0$), it indicates that the angle $\Omega_{z\to-\infty} \in (-\pi, 0)$, which implies that the function $\Omega_{z\to-\infty}$ can be calculated via Eq. (3.64). Thus, the expression for the first integral can be written as

$$\mathcal{I}_1 = \pi - \frac{1}{3\sqrt{2}}\frac{1}{\xi} + \mathcal{O}(\xi^{-2}). \tag{3.67}$$

Now we may consider the integration for $\rho = M\xi \to \infty$, where the vector field $\mathbf{v}_{+}^{\mathrm{SBHSU}}$ is approximately given by

$$\mathrm{v}_{\rho,+}^{\mathrm{SBHSU}} \approx 3j + \mathcal{O}(\xi^{-1}), \tag{3.68}$$

$$\mathrm{v}_{z,+}^{\mathrm{SBHSU}} \approx 0 + \mathcal{O}(\xi^{-1}). \tag{3.69}$$

Since, up to zeroth order in ξ^{-1}, the vector field $\mathbf{v}_{+}^{\mathrm{SBHSU}}$ does not depend on neither of the coordinates ρ and z, as ρ approaches infinity, we can deduce that the contribution $\mathcal{I}_2$ from path C_2 to the TC is zero:

$$\mathcal{I}_2 = 0\ . \tag{3.70}$$

To complete the asymptotic analysis, we have to calculate $\mathcal{I}_3$. In this integration we let $z = M\xi \to \infty$, where the vector field $\mathbf{v}_{+}^{\mathrm{SBHSU}}$ is approximately given by

$$\mathrm{v}_{\rho,+}^{\mathrm{SBHSU}} \approx -\frac{1 - 3j^2\rho^4}{\rho^2\sqrt{1 + j^2\rho^4}} + \mathcal{O}(\xi^{-1}), \tag{3.71}$$

$$\mathrm{v}_{z,+}^{\mathrm{SBHSU}} \approx -\frac{4j}{\sqrt{1 + j^2\rho^4}} + \mathcal{O}(\xi^{-1}). \tag{3.72}$$

Thus, the calculation is performed exactly the same as it was for the C_1 path, just swapping the integration limits, which gives

$$\mathcal{I}_3 = -\pi + \frac{1}{3\sqrt{2}}\frac{1}{\xi} + \mathcal{O}(\xi^{-2}). \tag{3.73}$$

Axis limit

In this part of integration we let $\rho = M/\xi \to 0$. The coordinate z has to satisfy either $z > M$ or $z < -M$. We first consider the case $z > M$, which is associated with the $\mathcal{I}_4$ integral. Thus, we can make an approximation for the vector field $\mathbf{v}_+^{\mathrm{SBHSU}}$ as follows:

$$\mathrm{v}_{\rho,+}^{\mathrm{SBHSU}} \approx -\left(\frac{z-M}{z+M}\right)^{3/2} \frac{\xi^2}{M^2} + \mathcal{O}(\xi^0) \ , \tag{3.74}$$

$$\mathrm{v}_{z,+}^{\mathrm{SBHSU}} \approx \frac{2\sqrt{z-M}}{(z+M)^{5/2}}\xi + \mathcal{O}(\xi^0) \ . \tag{3.75}$$

The corresponding angle Ω will be denoted by $\Omega_{\rho\to 0}^{z>M}$. Since the ρ-component, $\mathrm{v}_{\rho,+}^{\mathrm{SBHSU}}$, is negative ($\mathrm{v}_{\rho,+}^{\mathrm{SBHSU}} > 0$), it indicates that the angle $\Omega_{\rho\to 0}^{z>M}$ lies between $\pi/2$ and $3\pi/2$, which implies that Eq. (3.62) is suitable for this calculation. Thus, the expression for $\mathcal{I}_4$ can be written as

$$\mathcal{I}_4 = -\frac{\pi}{2} + \frac{8jM^2}{\xi} + \mathcal{O}(\xi^{-2}). \tag{3.76}$$

Analogously, we may calculate $\mathcal{I}_6$ considering $z < -M$. We obtain that the vector field $\mathbf{v}_+^{\mathrm{SBHSU}}$ takes the approximated form:

$$\mathrm{v}_{\rho,+}^{\mathrm{SBHSU}} \approx -\left(\frac{z+M}{z-M}\right)^{3/2} \frac{\xi^2}{M^2} + \mathcal{O}(\xi^0) \ , \tag{3.77}$$

$$\mathrm{v}_{z,+}^{\mathrm{SBHSU}} \approx -\frac{2\sqrt{-z-M}}{(-z+M)^{5/2}}\xi + \mathcal{O}(\xi^0) \ . \tag{3.78}$$

The corresponding angle Ω will be denoted by $\Omega_{\rho\to 0}^{z<-M}$. Since the ρ-component, $\mathrm{v}_{\rho,+}^{\mathrm{SBHSU}}$, is negative ($\mathrm{v}_{\rho,+}^{\mathrm{SBHSU}} < 0$), it indicates that the angle $\Omega_{\rho\to 0}^{z<-M}$ lies between $\pi/2$ and $3\pi/2$, which implies that we must use Eq. (3.62). Thus, the expression for $\mathcal{I}_6$ is given by

$$\mathcal{I}_6 = -\frac{\pi}{2} + \frac{8jM^2}{\xi} + \mathcal{O}(\xi^{-2}). \tag{3.79}$$

Horizon limit

Following the C_5 curve, we still have $\rho = M/\xi \to 0$, but now $|z| < M$. We want to show that $\mathrm{v}_{\rho,+}^{\mathrm{SBHSU}} > 0$, hence we may use Eq. (3.61) to evaluate $\mathcal{I}_5$. In order to do so, we have to

go back do spherical coordinates. Thus, we have that

$$\mathrm{v}_{\rho,+}^{\mathrm{SBHSU}}=\frac{\partial_\rho\mathcal{H}_+^{\mathrm{SBHSU}}}{\sqrt{g_{\rho\rho}}}=\frac{\left(\frac{\partial r}{\partial\rho}\frac{\partial}{\partial r}+\frac{\partial\theta}{\partial\rho}\frac{\partial}{\partial\theta}\right)\mathcal{H}_+^{\mathrm{SBHSU}}}{\sqrt{\left(\frac{\partial r}{\partial\rho}\right)^2 g_{rr}+\left(\frac{\partial\theta}{\partial\rho}\right)^2 g_{\theta\theta}}}\underset{r\to 2M}{\approx}\frac{\partial_r\mathcal{H}_+^{\mathrm{SBHSU}}}{\sqrt{g_{rr}}}. \tag{3.80}$$

Therefore, the ρ-component of the vector field $\mathbf{v}_+$, nearby the horizon ($r=2M+\delta r$, where δr is a small, positive real number), in spherical coordinates, can be written as

$$\mathrm{v}_{\rho,+}^{\mathrm{SBHSU}}\approx\frac{\sqrt{F(2M,\theta)}}{8M^2\sin\theta}-\sqrt{\frac{2}{M}}\frac{2j\cos\theta}{\sqrt{F(2M,\theta)}}\delta r^{1/2}+\mathcal{O}(\delta r). \tag{3.81}$$

Since $\delta r\to 0$, we have that $\mathrm{v}_{\rho,+}^{\mathrm{SBHSU}}>0$. Thus, let $\Omega_{\rho\to 0}^{|z|<M}$ denote the vector field angle with the horizontal axis. We must have $\Omega_{\rho\to 0}^{|z|<M}\in(-\pi/2,\pi/2)$, implying that we may use Eq. (3.61). The corresponding integral $\mathcal{I}_5$ must be given by

$$\mathcal{I}_5=-\pi+\frac{16jM}{\xi}+\mathcal{O}(\xi^{-2}). \tag{3.82}$$

We can now compute the total TC using Eq. (3.60), which is given by

$$\begin{aligned} w&=\lim_{\xi\to\infty}\frac{1}{2\pi}\left(\mathcal{I}_1+\mathcal{I}_2+\mathcal{I}_3+\mathcal{I}_4+\mathcal{I}_5+\mathcal{I}_6\right)\\ &=\lim_{\xi\to\infty}\left[-\pi+\frac{16jM^2}{\xi}+\mathcal{O}(\xi^{-2})\right]=-\pi. \end{aligned} \tag{3.83}$$

Therefore, we proved that there must exist one unstable LR, for all values of $j\in(0,\infty)$, associated with the vector field $\mathbf{v}_+$. Due to the odd $\mathbb{Z}_2$ symmetry (see Appendix A) manifested in Eq. (3.45), we can also conclude that there is also another LR associated with $\mathbf{v}_-$, with the same radial coordinate ρ and reflected z-coordinate with respect to the equatorial plane. Therefore, there are two LRs, one for each potential.

To conclude our analysis in this section concerning LRs, we turn our attention to the examination of the TC within the context of the background spacetime alone, excluding the presence of the Schwarzschild BH. To study the SU we have to consider the same calculation, but now setting $M=0$. For $M=0$, the formulae undergo a substantial simplification. The Weyl coordinates reduce to cylindrical coordinates (see Eq. (3.26)).

The potentials $\mathcal{H}_\pm^{\mathrm{SBHSU}}|_{M=0}\equiv\mathcal{H}_\pm^{\mathrm{SU}}$ are given by

$$\mathcal{H}_\pm^{\mathrm{SU}}=-4jz\pm\left(j^2\rho^3+\frac{1}{\rho}\right). \tag{3.84}$$

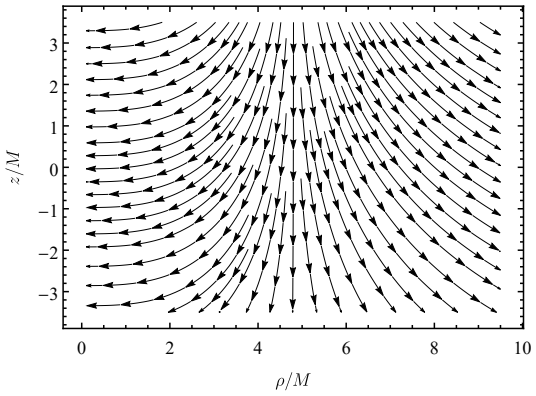

Figure 3.9: Plot illustrating the vector field $\mathbf{v}_{+}^{\mathrm{SBHSU}} = (\mathrm{v}_{\rho,+}^{\mathrm{SBHSU}}, \mathrm{v}_{z,+}^{\mathrm{SBHSU}})$ in the $(\rho/M, z/M)$-plane for the SU with $j = 0.025$. Since Eq. (3.85) does not depend on the coordinate z, the pattern of the vector field displayed in the plot repeats itself infinitely upwards and downwards.

The associated vector fields $\mathbf{v}_{\pm}^{\mathrm{SBHSU}}$ can be written as

$$\mathbf{v}_{\pm}^{\mathrm{SBHSU}} = \left(\mp \frac{1 - 3j^2\rho^4}{\rho^2\sqrt{1 + j^2\rho^4}}, -\frac{4j}{\sqrt{1 + j^2\rho^4}} \right). \tag{3.85}$$

The vector fields $\mathbf{v}_{\pm}^{\mathrm{SBHSU}}$ of the SU are precisely the ones that we obtained for the SBHSU case in the limit $z \to \pm\infty$.

In Fig. 3.9 we display a vector plot of $\mathbf{v}_{+}^{\mathrm{SBHSU}}$. Since the vector field does not depend on the z coordinate, the winding number is zero for any curve C in the (ρ, z)-plane. Therefore, the total TC is also zero, implying that in the SU there are no LRs.

To conclude, the LR of the SBHSU spacetime is actually the LR inherited from the Schwarzschild BH that was split and pushed off the equator by the the swirling background.

3.4 Shadows and gravitational lensing

In this section we investigate the shadow and gravitational lensing phenomena of the SBHSU solution defined by Eq. (3.17).

However, the SBHSU does not appear to be integrable in the (t, r, θ, φ) coordinates, in contrast with the SU background [179]. But one may calculate the shadow by means of numerical simulations using (backward) ray-tracing codes.

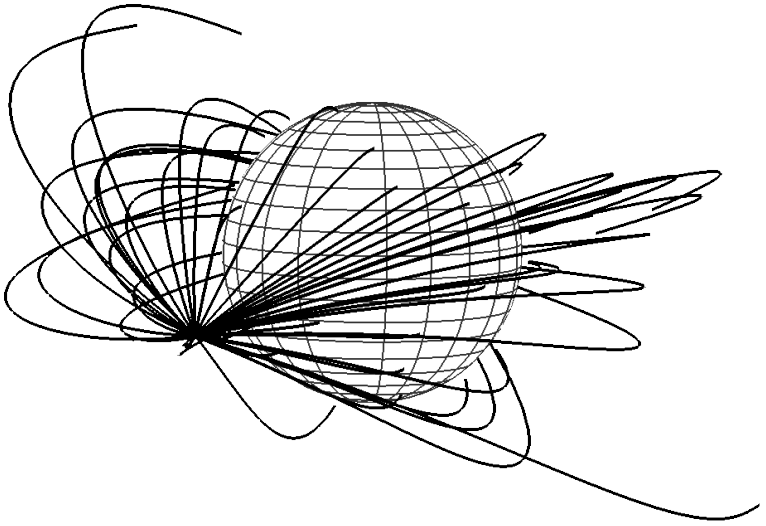

Figure 3.10: Plot illustrating the backward ray-tracing method for the SBHSU spacetime. We evolved, numerically, 50 null geodesics with initial conditions given by Eqs. (3.86)-(3.89), $\theta = \pi/2$ and $r = 10M$. We have chosen the observation angles at random.

Here, we numerically integrate Eqs. (3.36) and (3.37), with initial conditions given by

$$E = \sqrt{f(r)F(r,\theta)} - \frac{4jr^2 \cos\alpha \sin\beta f(r) \sin\theta \cos\theta}{\sqrt{F(r,\theta)}}, \tag{3.86}$$

$$p_r = \cos\alpha \cos\beta \sqrt{\frac{F(r,\theta)}{f(r)}}, \tag{3.87}$$

$$p_\theta = r\sqrt{F(r,\theta)} \sin\alpha, \tag{3.88}$$

$$L = \frac{r \cos\alpha \sin\beta \sin\theta}{\sqrt{F(r,\theta)}}, \tag{3.89}$$

where α, β are the observation angles and Eqs. (4.32)-(4.35) are evaluated at the observer coordinates. These initial conditions are obtained by projecting the photon's momentum into the observer's tetrad frame - see Ref. [115] for more details.

The initial conditions of the photon are defined by the observation angles. Using the PyHole package implemented in Python [116], varying the observation angles, we evolved 1024×1024 light ray trajectories. An illustration of the backward ray-tracing method is depicted in Fig. 3.10.

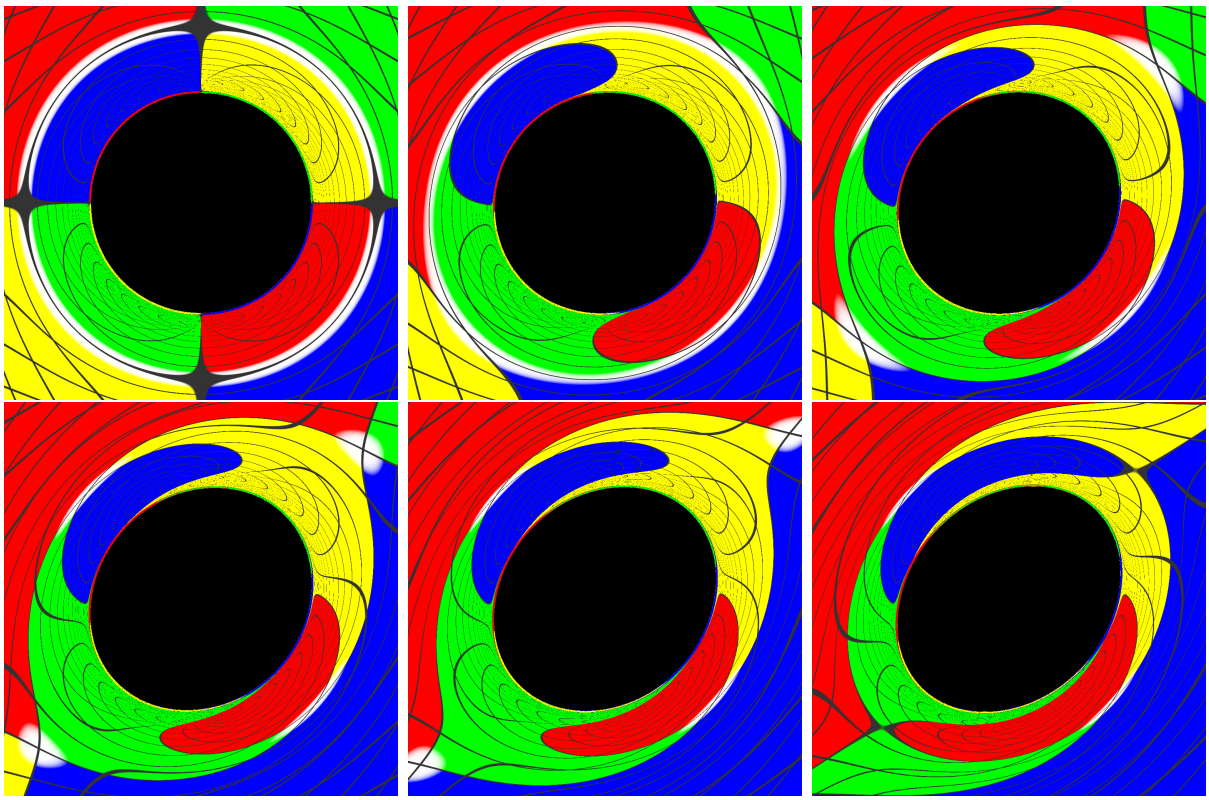

Figure 3.11: Shadow and gravitational lensing of the SBHSU, starting with the Schwarzschild case and increasing the swirling parameter j in equal steps of $\delta j = 0.0001$. In all the images, the observer is positioned at the equatorial plane ($\theta = \pi/2$) and at the radius $r = 15M$.

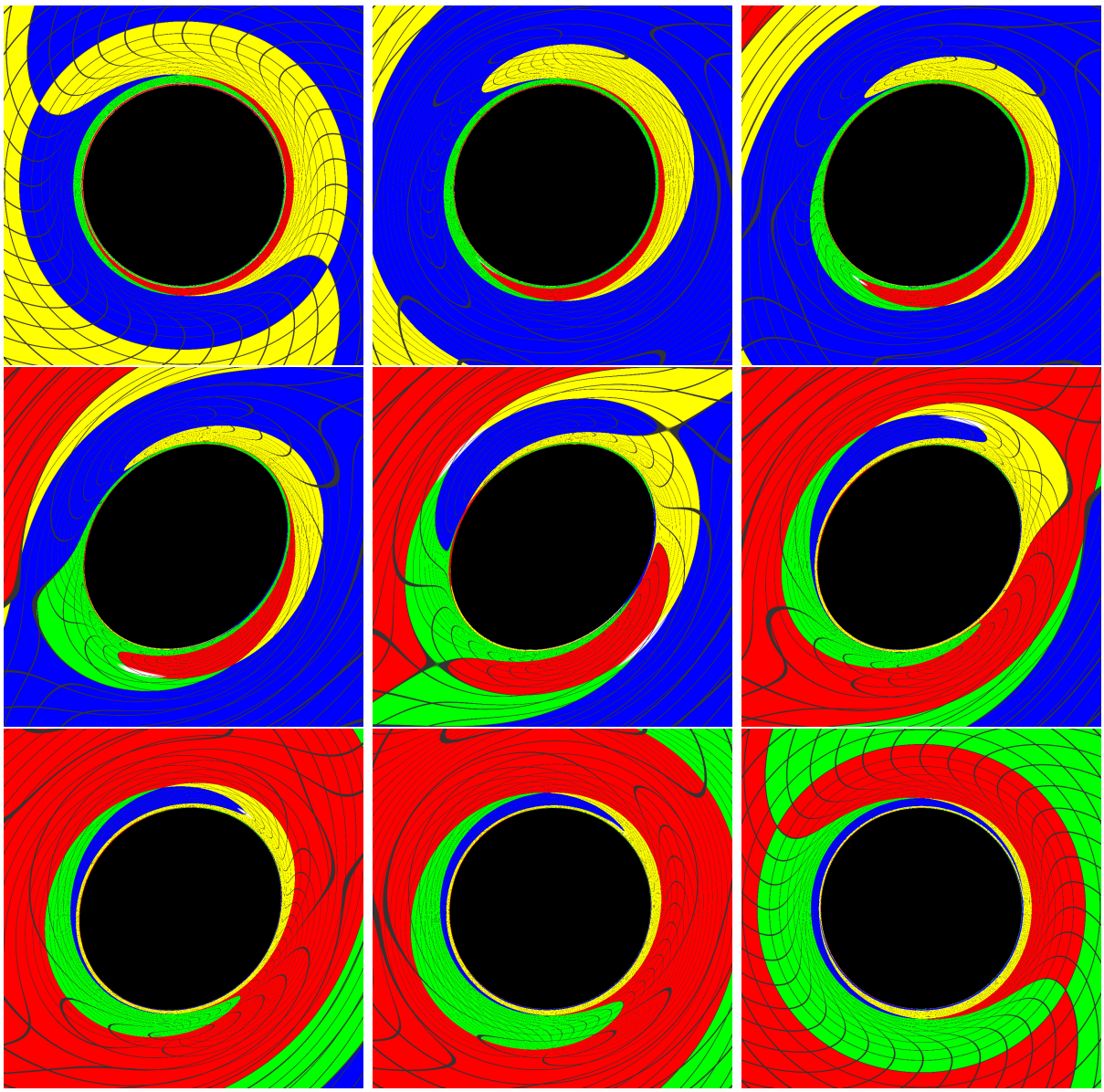

Figure 3.12: Shadow and gravitational lensing of the SBHSU, for $jM^2 = 0.0005$, for several observer positions. We start with $\theta = 0$ (on axis observer seeing the BH from the top) and we increase the angle θ in equal steps of $\delta\theta = \pi/8$, until we reach $\theta = \pi$ (on axis observer seeing the BH from the bottom). We kept the radius fixed at $r = 15M$.

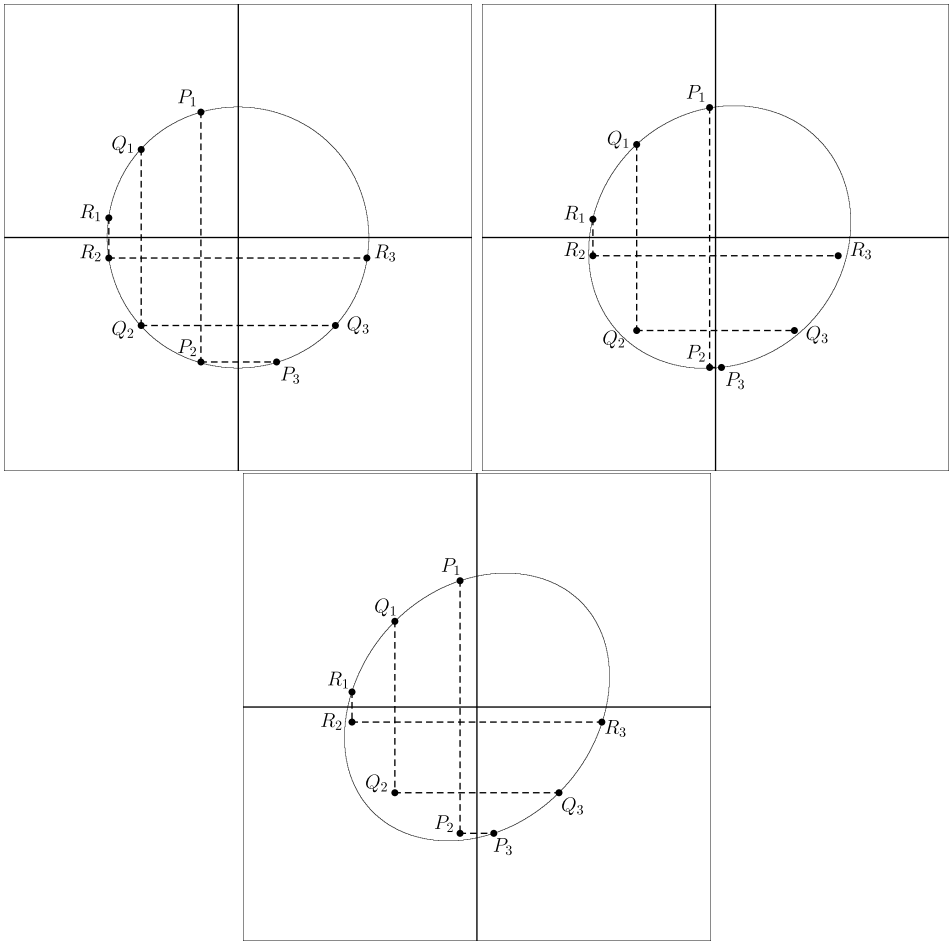

Figure 3.13: Shadow edge of the SBHSU for $jM^2 = 0.0005$, for observers positioned at $\theta = 0$ (top left), $\theta = \pi/4$ (top right) and $\theta = \pi/2$ (bottom). We kept the radius fixed at $r = 15M$. The points P_1, Q_1 and R_1 are randomly chosen points on the shadow's edge. The points P_2, Q_2 and R_2 are obtained by reflecting P_1, Q_1 and R_1 with respect to the horizontal axis at the middle of each plot. The points P_3, Q_3 and R_3 are obtained by reflecting P_2, Q_2 and R_2 with respect to the vertical axis.

3.4.1 Equatorial plane images

The shadows and gravitational lensing of the SBHSU, described by Eq. (3.17), are displayed in Fig. 3.11. We considered the observer positioned on the equatorial plane, $\theta = \pi/2$, and with radial coordinate $r = 15M$. We computed the images for several values of the swirling background parameter, namely, $jM^2 = n\delta j$, with $n \in \{0, 1, 2, 3, 4, 5\}$ and $\delta j = 0.0001$. The top left image corresponds to the Schwarzschild BH, for reference. We increase the parameter j from left to right, top to bottom, in each image of Fig. 3.11. The contour of the shadow gets a tilted oblate shape in comparison to the Schwarzschild BH. Regarding the gravitational lensing effects in the images, they also become more oblate as j increases. The Einstein ring, present in the Schwarzschild's case, disappears when we increase the swirling parameter.

3.4.2 Off-equatorial plane images

Next we analyze the shadow and gravitational lensing when the observer is positioned off the equator. For this case, we considered images with $jM^2 = 0.0005$, keeping the same radial distance, but now changing observer θ coordinate, starting at $\theta = 0$ and ending at $\theta = \pi$. We considered equal step displacements $\delta\theta = \pi/8$ in the observer's θ coordinate.

The simulated images are displayed in Fig. 3.12. The first (last) image corresponds to an observer located right above (below) the BH. In this case, due to axial symmetry, the shadow's boundary is a perfect circle. The predominant colors for this position of the observer are blue and yellow (green and red), which compose the bottom (top) hemisphere of the celestial sphere, hence, are in front of the observer. Nevertheless, it is still possible to see the other two colors near the shadow's edge, which are on the back of the observer.

As we move the observer along the θ direction, from the poles to the equator, all the colors blend together and the distinct circular shape of the shadow's edge fades away. Interestingly, moving the observer away from the poles disrupts the $\mathbb{Z}_2$ symmetry. The $\mathbb{Z}_2$ symmetry breaking of the shadow is depicted in Fig. 3.13. To represent the reflections we considered 3 different points, namely P_1, Q_1 and R_1; on the shadow's edge in each panel. The points P_1, Q_1 and R_1 are first reflected with respect to the horizontal axis and end up on the points

P_2, Q_2 and R_2, respectively. Afterwards, we consider a second reflection, now with respect to the vertical axis, mapping P_2, Q_2 and R_2 to P_3, Q_3 and R_3, respectively. The point P_1 is always chosen to be near the vertical axis, the point R_1 is close to horizontal axis, whereas the point Q_1 is chosen about half the way between the other two.

For an observer with $\theta = 0$ or $\theta = \pi$, the shadow's edge has a $\mathbb{Z}_2 \times \mathbb{Z}_2$ symmetry. This means that any point on the shadow's boundary, if reflected with respect to either horizontal or vertical axis, ends up in an another point contained on the shadow's edge. Those reflections are illustrated on the top left panel of Fig. 3.13.

Considering now an observer at $\theta = \pi/4$, no reflection symmetry with respect to the vertical and/or horizontal axes is present. The top right panel in Fig. 3.13 represents the reflection for this case. The point P_1 close to vertical axis is (approximately) mapped to another point on the shadow's edge after both vertical and horizontal reflections. However, as we consider points on the shadow closer to the horizontal axis, such as Q_1 and R_1, the reflections do not map those points to another point on the shadow's boundary. The point that most clearly illustrates the symmetry breaking is R_1, located near the horizontal axis.

Finally we considered the case where the observer is at the equatorial plane $\theta = \pi/2$. In this case the odd $\mathbb{Z}_2$ (see Appendix A) is present. Therefore, any point on the shadow's edge, after both vertical and horizontal reflections are mapped to other points on the shadow's edge. Hence, for those observers, the symmetry of the underlying spacetime is inherited for its shadow. Such modification of the symmetry properties of the shadow illustrated here emphasizes the already known concept that the shadow is observer dependent.

3.5 Remarks

The SBHSU [160,161] represents a novel class of exact solutions of vacuum Einstein's GR, initially explored in Ref. [160] and exhibiting intriguing properties. We explored the shadows and gravitational lensing of the SBHSU. Because the SBHSU described with (t, r, θ, φ) coordinates does not appear to be integrable, we employed the backward ray-tracing technique to compute the shadow and gravitational lensing. Our findings show that when observers are positioned at the equatorial plane, the shadow inherits the odd reflection symmetry present

in the spacetime, giving a prolate shape for its boundary along a diagonal direction - a sort of twisting of the shadow. However, for observers off the equatorial plane, this odd symmetry is lost, except for those situated at $\theta = 0$ or $\theta = \pi$, where the shadow exhibits $\mathbb{Z}_2 \times \mathbb{Z}_2$ symmetry.

Our analysis of the null geodesic flow in the SBHSU also revealed the existence of two unstable LRs (total TC $w = -1$ for each $\mathcal{H}_{\pm}^{\mathrm{SBHSU}}$), each co-rotating with the underlying spacetime. We have shown that, due to the odd $\mathbb{Z}_2$ symmetry, these LRs must exist outside the equatorial plane.

The concepts of odd and even $\mathbb{Z}_2$ symmetry, introduced in Appendix A, are fundamental to our results. This classification is important to understand the behavior of null geodesics in the Schwarzschild BH within the SU. Several distinguishing properties of LRs, shadows and gravitational lensing of the SBHSU are related to the odd type of symmetry.

Chapter 4

Spinning generalizations of Majumdar-Papapetrou multi-black hole spacetimes: light rings, lensing and shadows

4.1 Introduction

As discussed in Chap. 1, dynamical BBH solutions can model the complex dynamics of common gravitational wave sources. Yet, constructing these solutions in GR is exceptionally challenging, as the problem lacks generic symmetries and involves fundamentally time-dependent processes.

An intermediate simpler way, albeit limited in scope, to get a glimpse of how BHs interact with each other is to analyze exact stationary solutions involving multiple BHs. In such solutions the BHs must be "fixed", for equilibrium to be achieved. This can be done by either fine tuning their physical parameters (distances, masses, angular momenta, gauge charges, external fields,...) or by introducing artificial structures to hold the BHs in place, such as conical singularities.

In 4-dimensional vacuum GR, asymptotically flat multi-centered BH configurations cannot remain in equilibrium without the presence of naked singularities [183–186]. For example,

the double Schwarzschild solution [187] and the double Kerr solution [188] require conical singularities. Even without resorting to gauge fields, however, conical singularities can be removed either by introducing additional (non-gauge) fields, such as scalar fields [189, 190], or by waiving asymptotic flatness [191, 192].

The introduction of gauge fields, on the other hand, opens up new possibilities. In Newtonian mechanics, the equilibrium between two charged, massive particles is achieved when the product of their masses equals the product of their electric charges (in appropriate units). The inherent non-linearities of GR would seem to preclude a straightforward generalization of this simple rule. Remarkably, however, in EM theory an equally simple (and related) rule applies: two (or more) BH configurations are possible if the BHs have the same (unitary) charge to mass ratio. Such spacetimes are constructed by superimposing two (or more) extremal RN BHs, leading to the Majumdar-Papapetrou (MP) solution [193, 194].

There have been attempts to extend the static MP solution to rotating spacetimes within EM theory [195, 196]. It turns out that the obtained generalizations describe the interaction between naked singularities rather than BHs [197]. On the other hand, enlarging the model from EM to Einstein-Maxwell-dilaton (EMD) with the Kaluza-Klein (KK) coupling between the dilaton and Maxwell field - hereafter dubbed *KK theory* -, Teo and Wan constructed a generalized version of the MP solution that accommodates rotating, electrically and magnetically charged BHs [198] that reduce to the standard MP of EM in the static limit. In other words, the dilaton is sourced by rotation. Moreover, the Teo-Wan (TW) spacetime represents a regular superposition of the well-known rotating, charged BHs in KK theory, the Rasheed-Larsen (RL) BHs [199, 200].

The TW metric is much simpler than the double-Kerr solution, making it a convenient laboratory for rotational effects on physical observables. Additionally, it is free of conical singularities, which makes it more physically appealing. Even though it should not be faced as a representation of (astro)physical reality, as it remains inherently dyonic and with extremal horizons, its theoretical advantages, motivate us to analyze its null geodesic flow, exploring the effects of rotation on a multi-BH system.

In this chapter, we explore the LRs, shadows, and gravitational lensing effects of the TW spacetime. As we will demonstrate, the LR structure—or more generally, the FPO

structure—of this rotating, KK theory counterpart of the MP spacetime, is significantly more involved than that of its static counterpart. The remainder of this chapter is organized as follows. In Sect. 4.2, we review key aspects of the single RL BH solution, which is the basis for deriving the TW solution, revisiting its main properties. Sect. 4.3 reviews key aspects of the single TW solution restricted to the case of only two BHs in equilibrium. Sect. 4.4 focuses on the motion of null geodesics in the TW spacetime, where we define the 2-dimensional effective potentials $\mathcal{H}_{\pm}^{\rm TW}$ and analyze the LR structure using the techniques introduced in Ref. [105, 165]. In Sect. 4.5, we present our findings on the shadow and gravitational lensing effects of the TW spacetime. Finally, Sec. 4.6 presents some remarks about this chapter.

4.2 Single BH solution: Rasheed-Larsen spacetime

4.2.1 KK theory

In this section we review some aspects of the RL spacetime, a solution in KK theory.

KK theory emerges from Einstein's pure gravity theory in higher-dimensional spacetimes. Specifically, we consider $(1+4)$-dimensional vacuum GR, described by the action:

$$S = \frac{1}{16\pi G_5}\int d^5X\sqrt{-g_{(5)}}R_{(5)}, \tag{4.1}$$

where G_5 is Newton's constant in five spacetime dimensions, $g_{(5)}$ and $R_{(5)}$ denote the five dimensional metric and Ricci scalar, respectively, and $X^M=(x^\mu,x^5)$ are the five dimensional coordinates. The fifth dimension, x^5, is compactified, and the 5-dimensional metric remains invariant under translations along this compact dimension. These conditions allow the 5-dimensional vacuum equations to be mapped into a 4-dimensional theory with a (dilaton) scalar field coupled to Maxwell electrodynamics, under the KK ansatz

$$ds^2_{(5)} = e^{\phi/\sqrt{3}}g_{\mu\nu}dx^\mu dx^\nu + e^{-2\phi/\sqrt{3}}(dx^5+2A_\mu dx^\mu)^2, \tag{4.2}$$

leading to KK theory

$$S = \frac{1}{16\pi G_4}\int d^4x\sqrt{-g}\left[R-\frac{1}{2}(\nabla\phi)^2-\frac{1}{4}e^{-\sqrt{3}\phi}F^2\right], \tag{4.3}$$

where ϕ is the dilaton field, $F^2 = F_{\mu\nu}F^{\mu\nu}$, $F_{\mu\nu} = \partial_\mu A_\nu - \partial_\nu A_\mu$ is the Maxwell 2-form and A_μ the potential 1-form. Thus, the higher-dimensional geometry naturally incorporates both scalar and electromagnetic sources within a 4-dimensional framework. This corresponds to a specific type of EMD theory, where the dilaton coupling constant is fixed as $\sqrt{3}$, by the process of dimensional reduction.

4.2.2 5-dimensional metric

The RL BH represents a stationary and axisymmetric solution in KK theory (4.3), characterized by a connected event horizon. This solution is parametrized by four independent physical quantities: the mass M, angular momentum J, electric charge Q, and magnetic charge P. For such family, there exists two distinct *extremal* classes, each corresponding to a different condition that saturates the bound for a horizon to exist. These two conditions can be represented within the parameter space shown in Fig. 4.1.

The TW solution is constructed using one of these classes, called *under-rotating extremal solutions*, for which Q and P are non-vanishing and J can take values in a certain (charge) dependent interval, with the minimum value being always zero. This is illustrated in Fig. 4.1.

Using a spherical-like coordinate system $(t, r, \theta, \varphi, x^5)$, the under-rotating limit of RL extremal solution [199, 200] is described (in their five dimensional guise) by the 5-dimensional metric

$$\begin{aligned} ds^2_{(5)} =& \frac{H_2}{H_1}\Bigg\{dx^5 - \left[2\left(r + \frac{p}{2} - pj\cos\theta\right)\right]\frac{Q}{H_2}dt \\ &- \left[2H_2\cos\theta - q\left(r + \frac{pq}{p+q}\right)j\sin^2\theta\right]\frac{P}{H_2}d\varphi\Bigg\}^2 \\ &- \frac{r^2}{H_2}\left(dt + \frac{2jPQ\sin^2\theta d\varphi}{r}\right)^2 \\ &+ H_1\left(\frac{dr^2}{r^2} + d\theta^2 + \sin^2\theta d\varphi^2\right), \end{aligned} \tag{4.4}$$

where

$$H_1 = r^2 + rp + \frac{p^2 q(1 + j\cos\theta)}{2(p+q)}, \tag{4.5}$$

$$H_2 = r^2 + rq + \frac{pq^2(1 - j\cos\theta)}{2(p+q)}, \tag{4.6}$$

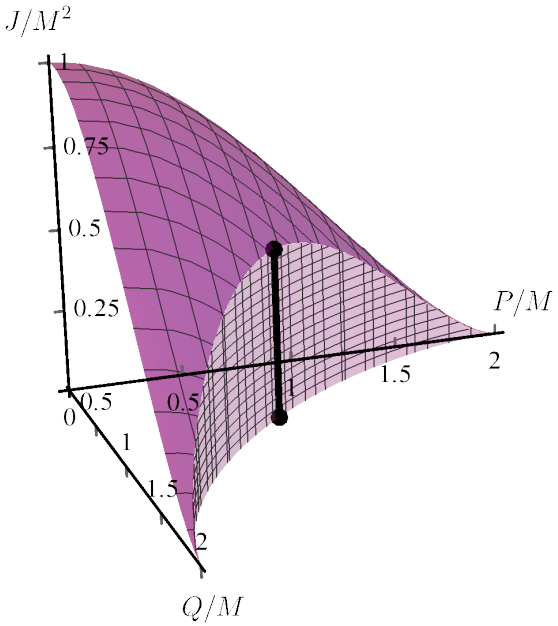

Figure 4.1: Surfaces of extreme solutions in KK theory. The under-rotating extremal solutions fall into the lighter purple wall. Fixing the charges and varying J, one gets a vertical line segment, as illustrated by the black solid line, with a vanishing minimum value of J. The other class of extremal solutions fall into the darker purple surface.

and p and q are positive quantities related to the electric and magnetic charge by

$$P^2 = \frac{p^3}{4(p+q)}, \qquad Q^2 = \frac{q^3}{4(p+q)}. \tag{4.7}$$

The mass and angular momentum are [198] $4M = p + q$ and $J = jPQ$ and are constrained by $(P/M)^{2/3} + (Q/M)^{2/3} = 2^{2/3}$ and $|J| < |PQ|$. Following [198], to construct the multi-centered solution, a simplification is achieved by considering $P = Q = M/\sqrt{2}$, yielding the simplified five dimensional geometry

$$\begin{aligned} ds^2_{(5)} = \frac{H_2}{H_1}\{dx^5 - \sqrt{2}H_2^{-1}[M(r+M) - 2J\cos\theta]dt \\ - \sqrt{2}\left[M\cos\theta - 2JH_2^{-1}(r+M)\sin^2\theta\right]d\varphi\}^2 \\ - \frac{r^2}{H_2}\left(dt + \frac{2J\sin^2\theta d\varphi}{r}\right)^2 \\ + H_1\left(\frac{dr^2}{r^2} + d\theta^2 + \sin^2\theta d\varphi^2\right) \end{aligned} , \tag{4.8}$$

where now $H_{1,2} = (r+M)^2 \pm 2J\cos\theta$. While imposing equality between the charges is not a strict requirement, it greatly simplifies the construction of the multi-centered solution.

Eq. (4.8) describes a BH solution that lies along the black line segment on the parameter space represented in Fig. 4.1. This solution is characterized by two parameters, M and J, where $|J| < J_{\rm e} = M^2/2$. Here, $J = 0$ corresponds to the bottom black point in Fig. 4.1, while $J = J_{\rm e}$ represents the point on the top.

4.2.3 4-dimensional metric

After performing dimensional reduction with (4.2), the particular case of equal charges BHs, Eq. (4.8), leads to the 4-dimensional spacetime, characterized by its metric, gauge potential, and scalar field configuration:

$$\begin{aligned} ds^2 = &- \frac{(r-M)^2}{\sqrt{r^4 - 4J^2\cos^2\theta}}\left(dt + \frac{2J\sin^2\theta d\varphi}{r-M}\right)^2 \\ &+ \sqrt{r^4 - 4J^2\cos^2\theta}\left[\frac{dr^2}{(r-M)^2} + d\theta^2 + \sin^2\theta d\varphi^2\right], \end{aligned} \tag{4.9}$$

$$\begin{aligned} A_\mu dx^\mu = -\sqrt{2}\Bigg[&\left(\frac{Mr - 2J\cos\theta}{r^2 - 2J\cos\theta}\right)dt + \Bigg(M\cos\theta \\ &- \frac{2Jr\sin^2\theta}{r^2 - 2J\cos\theta}\Bigg)d\varphi\Bigg], \end{aligned} \tag{4.10}$$

$$\phi = \frac{\sqrt{3}}{2}\ln\left(\frac{r^2 + 2J\cos\theta}{r^2 - 2J\cos\theta}\right), \tag{4.11}$$

respectively.

The event horizon is located at $r = M$, enclosing a curvature singularity at $r = \sqrt{2|J\cos\theta|}$. In the limit $J = 0$ the dilaton trivializes, and this solution reduces to the extremal RN BH of EM theory.

The geometry of the event horizon is determined by restricting Eq. (4.9) to the 2-surface $t =$ constant and $r = M$. The area A_H of this surface is given by $A_H = 4\pi\sqrt{M^4 - 4J^2}$. The horizon Gaussian curvature is everywhere positive throughout the entire parameter space. Consequently, there exists a unique isometric embedding (up to rigid rotations) of the horizon surface into a 3-dimensional Euclidean space [201]. In Fig. 4.2 we display the isometric embedding for $J/J_{\rm e} = 0, 0.2, 0.4, 0.6$.

The parameters M and J are constants obtained via Komar integrals evaluated at infinity. However, we may also evaluate the mass and angular momentum by Komar integrals over

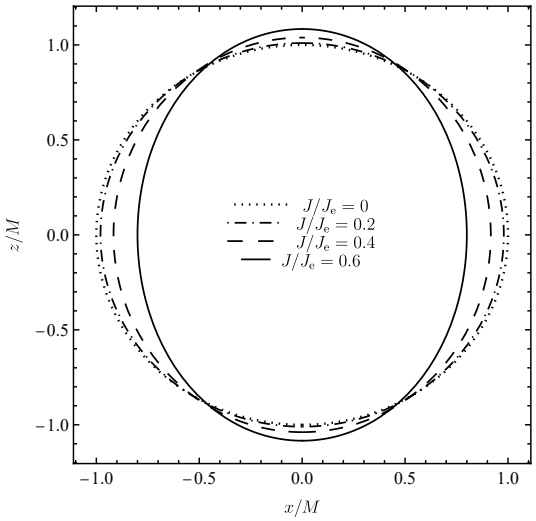

Figure 4.2: Isometric embedding of the horizon into 3-dimensional Euclidean space for $J/J_{\rm e} = 0, 0.2, 0.4, 0.6$. As the angular momentum increases, the area diminishes, in accordance with the expression of A_H. In the limit of $J/J_{\rm e} \to 1$, the area A_H vanishes.

the horizon [202]. From this, we find that the horizon mass M_H and the horizon angular momentum J_H are given by

$$M_H = 0, \tag{4.12}$$

$$J_H = \frac{(4J^2 - M^4)\left[(4J^2 - M^4)\tanh^{-1}\left(\frac{2J}{M^2}\right) + 2JM^2\right]}{16J^2M^2}, \tag{4.13}$$

respectively.

Thus, RL under-rotating extremal solutions have their entire mass contained outside the horizon, carried by the external fields, a characteristic shared with the RN extremal solution [202], while $J_H \neq 0$ in general. Figure 4.3 shows the profile of J_H as a function of J, from which we observe that the horizon angular momentum has an opposite sign to the angular momentum of the whole spacetime.

Despite the non-vanishing horizon angular momentum, we emphasize that the horizon has zero angular velocity, as inferred from $-g_{t\varphi}/g_{\varphi\varphi} = 2J(r-M)/(r^4 - 4J^2)$ [199,200]. This implies the absence of an ergoregion. Unlike other well known cases, as the BMPV BH in $D = 5$, in which the absence of an ergoregion can be associated to supersymmetry [203], this class of solutions is not supersymmetric [198].

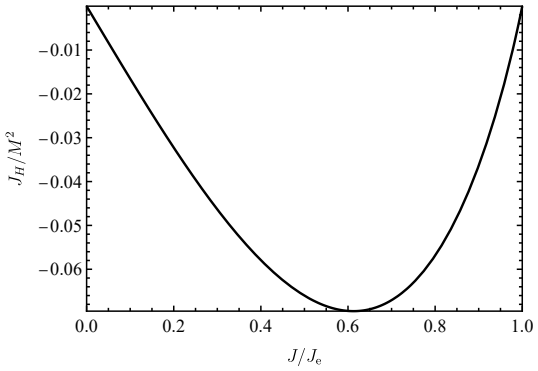

Figure 4.3: Angular momentum at the horizon J_H, as a function of the parameter J of the solution (4.9).

4.3 Teo-Wan spacetime

4.3.1 The solution

It was remarked in Ref. [198] that the RL solution in the under-rotating extremal limit is contained within a class of solutions reported by Clément [204], characterized by two harmonic functions. This structure is the trademark of a superposition principle and allowed Teo and Wan to extend the single extremal BH solution (4.8) to a multi-BH configuration by generalizing the single center harmonic functions to multi-center ones. The resulting TW solution describes an asymptotically flat, stationary, axisymmetric, multi-centered nonsingular equilibrium configuration of rotating dyonic BHs, each with an extremal horizon. The particular case of two BHs may be written as

$$ds^2 = -\frac{(dt+\omega^0_\varphi d\varphi)^2}{\sqrt{H_+H_-}} + \sqrt{H_+H_-}\left(d\rho^2+dz^2+\rho^2 d\varphi^2\right), \tag{4.14}$$

$$\begin{aligned} A_\mu dx^\mu = \frac{\sqrt{2}}{H_-}\Bigg\{ &-\left[(1+f)f-2g\right]dt \\ &+\left[(1+f)\omega^0_\varphi + \frac{H_-\tilde{\omega}^5_\varphi}{\sqrt{2}}\right]d\varphi\Bigg\}, \end{aligned} \tag{4.15}$$

$$\phi = \frac{\sqrt{3}}{2}\ln\frac{H_+}{H_-}, \tag{4.16}$$

where

$$H_\pm = (1+f)^2 \pm 2g, \tag{4.17}$$

$$\omega^0_\varphi = \frac{2J_1\rho^2}{[\rho^2+(z+a)^2]^{3/2}} + \frac{2J_2\rho^2}{[\rho^2+(z-a)^2]^{3/2}}, \tag{4.18}$$

$$\tilde{\omega}^5_\varphi = -\frac{\sqrt{2}M_1(z+a)}{\sqrt{\rho^2+(z-a)^2}} - \frac{\sqrt{2}M_2(z-a)}{\sqrt{\rho^2+(z+a)^2}}, \tag{4.19}$$

and

$$f = \frac{M_1}{\sqrt{\rho^2+(z+a)^2}} + \frac{M_2}{\sqrt{\rho^2+(z-a)^2}}, \tag{4.20}$$

$$g = \frac{J_1(z+a)}{\sqrt{\rho^2+(z+a)^2}^3} + \frac{J_2(z-a)}{\sqrt{\rho^2+(z-a)^2}^3}. \tag{4.21}$$

The double BH spacetime is determined by 5 parameters, namely: M_1, M_2, J_1, J_2 and a, where $|J_1| < J_{\mathrm{e},1} = M_1^2/2$, $|J_2| < J_{\mathrm{e},2} = M_2^2/2$ and $a \geq 0$. The multi-centered solution reduces to the single 4-dimensional BH solution of Sec. 4.2 with the coordinate change $\{\rho = (r-M)\sin\theta, z = (r-M)\cos\theta\}$, when $a \to 0$ and with the identifications $M_1 \to M/2$, $M_2 \to M/2$, $J_1 \to J/2$, and $J_2 \to J/2$.

We remark that Eq. (4.14), expressed in cylindrical coordinates $\{t, \rho, z, \varphi\}$, has a spatial sector conformal to the Euclidean 3-space, $\mathbb{E}^3$. Accordingly, we define the Euclidean position $\boldsymbol{x} = (x, y, z)$, where x, y, and z are rectangular coordinates. The two BHs are located at $\boldsymbol{x}_1 = (0, 0, -a)$ and $\boldsymbol{x}_2 = (0, 0, a)$, making a the coordinate distance from the origin of $\mathbb{E}^3$ to each gravitating center.

The functions f and g are solutions of the Poisson equation on $\mathbb{E}^3$, respectively, namely

$$\Delta_{\mathbb{E}^3} f = 4\pi M_1 \delta(\boldsymbol{x} + a\hat{\boldsymbol{z}}) + 4\pi M_2 \delta(\boldsymbol{x} - a\hat{\boldsymbol{z}}), \tag{4.22}$$

$$\Delta_{\mathbb{E}^3} g = 4\pi \boldsymbol{J}_1 \cdot \nabla_{\mathbb{E}^3}\delta(\boldsymbol{x} + a\hat{\boldsymbol{z}}) + 4\pi \boldsymbol{J}_2 \cdot \nabla_{\mathbb{E}^3}\delta(\boldsymbol{x} - a\hat{\boldsymbol{z}}), \tag{4.23}$$

where $\delta(\cdot)$ is the Dirac delta function, $\hat{\boldsymbol{z}}$ denotes the unit vector along the z-axis and the vectors $\boldsymbol{J}_1$ and $\boldsymbol{J}_2$ are defined as $\boldsymbol{J}_1 = J_1\hat{\boldsymbol{z}}$ and $\boldsymbol{J}_2 = J_2\hat{\boldsymbol{z}}$. The operators $\Delta_{\mathbb{E}^3}$ and $\nabla_{\mathbb{E}^3}$ refer to the Laplacian and gradient on $\mathbb{E}^3$, respectively. Hence, f represents a pair of monopole solutions with monopole strengths M_1 and M_2, while g corresponds to a pair of dipole solutions with dipole moments J_1 and J_2.

The spacetime total mass and angular momentum can be calculated using Komar integrals and the Gauss's law, are given by $M_1 + M_2$ and $J_1 + J_2$, respectively. Moreover, the parameters (M_1, J_1) and (M_2, J_2) can be interpreted as the mass and angular momentum of the BHs located at $\boldsymbol{x}_1$ and $\boldsymbol{x}_2$, respectively, since Eqs. (4.14), (4.15), and (4.16) reduce to

Eqs. (4.9), (4.10), and (4.11) near each center, with the identifications $(M_1, J_1) \to (M, J)$ or $(M_2, J_2) \to (M, J)$. Therefore, all the analyses presented in Sec. 4.2 regarding horizon quantities and horizon embedding, remain valid for the multi-centered solution.

4.3.2 Majumdar-Papapetrou limit

For $J_1 = J_2 = 0$, the scalar field ϕ vanishes, as $H_+|_{J_1=J_2=0} = H_-|_{J_1=J_2=0}$. In this limit, the metric and the vector potential reduce to:

$$ds^2 = \frac{dt^2}{(1+f)^2} + (1+f)^2(d\rho^2 + dz^2 + \rho^2 d\varphi^2), \tag{4.24}$$

$$A_\mu dx^\mu = -\frac{\sqrt{2}f}{1+f}dt + \tilde{\omega}^5_\varphi d\varphi. \tag{4.25}$$

The metric and gauge potential given in Eqs. (4.24) and (4.25) correspond to the dyonic MP solution[1] [205].

4.4 Null orbits

4.4.1 Majumdar-Papapetrou null orbits

This subsection reviews null orbits in the MP spacetime, with a particular focus on null planar orbits, including LRs and other general FPOs. In Ref. [105], a theorem guarantees the existence of unstable LRs for BH spacetimes for each rotation sense. This result was later generalized in Ref. [165] for a configuration of N collinear BHs, which must accommodate at least N unstable LRs for each sense of rotation. Since this result relies solely on boundary conditions and not on the field equations, it applies to the TW solution (and in particular to MP) as well. The topological techniques developed in Refs. [105, 165] offer a powerful framework for analyzing the LR structure of both BH spacetimes and horizonless objects [104, 206]. This approach relies on evaluating a TC, which is derived from a circulation integral

[1] Usually the MP is presented with $A_t = (1+f)^{-1}$, different from Eq. (4.25). However, $-f/(1+f) = 1/(1+f) - 1$ and the -1 term can be gauged away, hence the two potentials are equivalent.

involving the normalized gradient of the following potential functions:

$$\mathcal{H}_{\pm} = \frac{-g_{t\varphi} \pm \sqrt{g_{t\varphi}^2 - g_{tt} g_{\varphi\varphi}}}{g_{\varphi\varphi}}. \tag{4.26}$$

The normalized gradients of $\mathcal{H}_{\pm}$ are defined by

$$\mathbf{v}_{\pm} = \left(\frac{1}{\sqrt{g_{\rho\rho}}} \frac{\partial \mathcal{H}_{\pm}}{\partial \rho}, \frac{1}{\sqrt{g_{zz}}} \frac{\partial \mathcal{H}_{\pm}}{\partial z} \right) = \left(\mathrm{v}_{\rho}^{\pm}, \mathrm{v}_{z}^{\pm} \right). \tag{4.27}$$

To determine the location of each LR, one can find the critical points of the potentials $\mathcal{H}_{\pm}$, or equivalently, identify the zeros of the vector field $\mathbf{v}_{\pm}$. By evaluating the circulation of $\mathbf{v}_{\pm}$ along a closed path in the (ρ, z)-plane that encloses exactly one of these zeros, a TC can be assigned to each LR. The TC is defined as $+1$ if the winding direction of $\mathbf{v}_{\pm}$ matches its circulation around the path; otherwise, it is -1.

TC$=-1$ corresponds to a saddle point of $\mathcal{H}_{\pm}$, TC$=+1$ indicates either a maximum or a minimum. Whether the LR represents a maximum or a minimum, depends on the behavior of the vector field $\mathbf{v}_{\pm}$ in a neighborhood of the point: if $\mathbf{v}_{\pm}$ is convergent, the point is a maximum, if it is divergent, the point is a minimum.

The total TC, calculated over a path that encloses all the LRs of a given spacetime, can be generically determined under appropriate boundary conditions. In Ref. [105], it was shown that in any single BH spacetime with properties of stationarity, axial symmetry, circularity, and asymptotic flatness, the total TC for each potential $\mathcal{H}_{\pm}$ is always -1. This result was later generalized in Ref. [165] to account for a configuration of N collinear BHs, where the corresponding total TC is given by $-N$.

The MP LR structure can be analyzed through the lens of the TC formalism. The potential functions $\mathcal{H}_{\pm}^{\mathrm{MP}}$ for the MP spacetime are given by

$$\mathcal{H}_{\pm}^{\mathrm{MP}} = \frac{\pm 1}{\rho \left(1+f\right)^2}. \tag{4.28}$$

Its corresponding vector fields $\mathbf{v}_{\pm}^{\mathrm{MP}}$ are given by

$$\left(\mathbf{v}_{\pm}^{\mathrm{MP}}\right)_j = \pm \frac{(1+f)\delta_j^{\rho} + 2\rho \partial_j f}{\rho^2 (1+f)^4}, \tag{4.29}$$

where $j = \rho, z$ and $\left(\mathbf{v}_{\pm}^{\mathrm{MP}}\right)_j$ denotes the j-th component of $\mathbf{v}_{\pm}^{\mathrm{MP}}$.

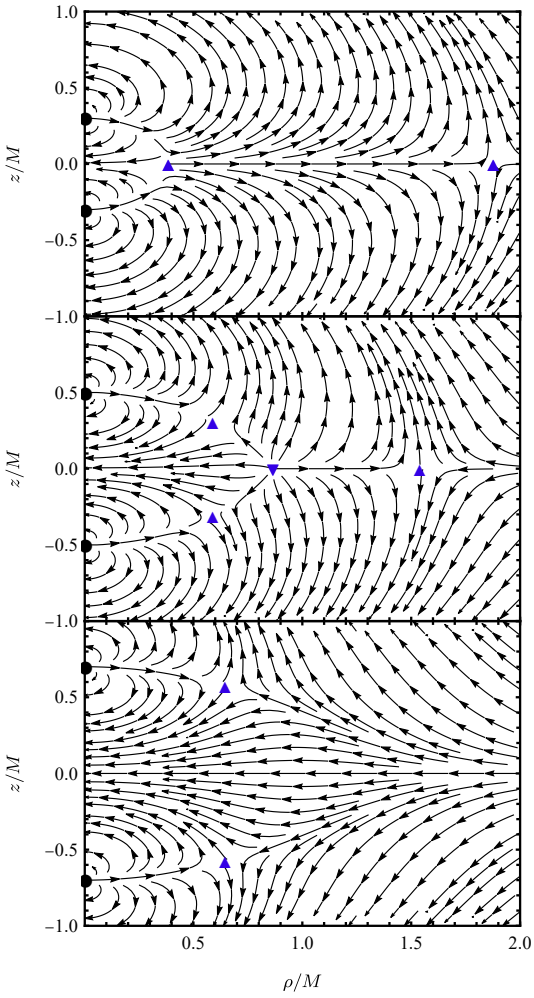

Figure 4.4: Vector field $\mathbf{v}_+^{\mathrm{MP}}$ over the (ρ, z)-plane for the 2-center MP with $a/M = 0.3$ (top), 0.5 (middle), 0.7 (bottom). Blue upright triangles indicate the positions of LRs with a TC of -1, while the inverted triangle marks the location of the LR with a TC of $+1$.

Since the MP solution is static, the potentials $\mathcal{H}_\pm^{\mathrm{MP}}$ and the vector fields $\mathbf{v}_\pm^{\mathrm{MP}}$ can only differ by a global minus sign. Hence it suffices to find the critical points and zeros of $\mathcal{H}_+^{\mathrm{MP}}$ and $\mathbf{v}_+^{\mathrm{MP}}$, respectively. Fig. 4.4 shows the LR configuration for $a/M = 0.3,\ 0.5,\ 0.7$, along with the vector plot of $\mathbf{v}_+^{\mathrm{MP}}$ for equal-mass BHs.

In the MP spacetime, for $M_1 = M_2 = M$, equatorial LRs can only exist when the coordinate distance a of each BH from the origin is below a critical value of $a_f/M \approx 0.5443$:

i) If a is smaller than another critical distance, $a_i/M \approx 0.3849$, both LRs are saddle points [207].

ii) Letting $a_i < a < a_f$, the internal LR becomes stable, while the external one remains a saddle point. Simultaneously, two off-equator LRs emerge, both saddle points.

iii) For $a > a_f$, the off-equatorial LRs remain saddle points and the equatorial ones disappear. For a summary, see Table 4.1.

For $a_i < a < a_f$, the saddle point indicates the presence of two critical contour lines on the non-Killing submanifold, along which the LR exhibits stability (along one) and instability (along the other one). In general, these lines do not need to intersect orthogonally. However, it can be shown that for (stationary, axisymmetric, circular) $\mathbb{Z}_2$-symmetric spacetimes in four dimensions with an unstable LR at the equator, the critical lines are indeed orthogonal. This orthogonality arises from the $\mathbb{Z}_2$ symmetry, which enforces $\partial_z g_{\mu\nu}|z=0 = \partial_z\partial_\rho g_{\mu\nu}|_{z=0} = 0 \Rightarrow \partial_z\partial_\rho \mathcal{H}_+^{\rm MP}|_{\rm LR} = 0$. Since the 2-center MP solution with equal masses is $\mathbb{Z}_2$, the stability of equatorial LRs is fully determined by their stability along the orthogonal ρ and z directions, *i.e.* $\partial_\rho^2 \mathcal{H}_+^{\rm MP}|_{\rm LR}$ and $\partial_z^2 \mathcal{H}_+^{\rm MP}|_{\rm LR}$.

	$a < a_i$	$a_i < a < a_f$	$a_f < a < \overline{a}_f$	$\overline{a}_f < a$
Internal	$\rho \smile \mid z \frown$ (-1)	$\rho \smile \mid z \smile$ (+1)	–	–
External	$\rho \frown \mid z \smile$ (-1)	$\rho \frown \mid z \smile$ (-1)	–	–
Top	–	$\rho \smile \mid z \smile$ (-1)	$\rho \smile \mid z \smile$ (-1)	$\rho \frown \mid z \smile$ (-1)
Bottom	–	$\rho \smile \mid z \smile$ (-1)	$\rho \smile \mid z \smile$ (-1)	$\rho \frown \mid z \smile$ (-1)

Table 4.1: LR (in)stability along the ρ and z directions of the MP solution with equal masses, for different ranges of the parameter a. Here, $\rho \smile$ and $z \smile$ denote stability, while $\rho \frown$ and $z \frown$ denote instability, in the respective directions. In brackets, after each LR, we present its TC. Clearly, in all cases the total TC is -2. But the analysis of purely the ρ and z behaviour may be misleading when cross derivatives of the potential are non-vanishing.

Off-equatorial LRs in the range $a_i < a < a_f$ are stable in both ρ and z directions; however in this case stability along both directions is not sufficient to conclude that these LRs correspond to minima of $\mathcal{H}_+^{\rm MP}$. Specifically, for off-equatorial LRs, the cross derivative $\partial_z\partial_\rho \mathcal{H}_+^{\rm MP}|_{\rm LR}$ does not vanish, so that the stability must be determined by the Hessian. Since $\det(\partial_i\partial_j \mathcal{H}_+^{\rm MP}) < 0$, these LRs are indeed saddle points.

It is worth noting that there is another critical value, $\overline{a}_f \approx 0.5515M \gtrapprox a_f$, for the parameter a, at which the stability of the off-equatorial LRs along the ρ direction transitions from stable to unstable. To better illustrate this stability transition, we plot the potential $\mathcal{H}_+^{\rm MP}$ as a function of ρ in Fig. 4.5, with $z = z_{\rm LR}(a)$. Here, $z_{\rm LR}(a)$ represents the z coordinate of the top off-equatorial LR corresponding to the parameter a.

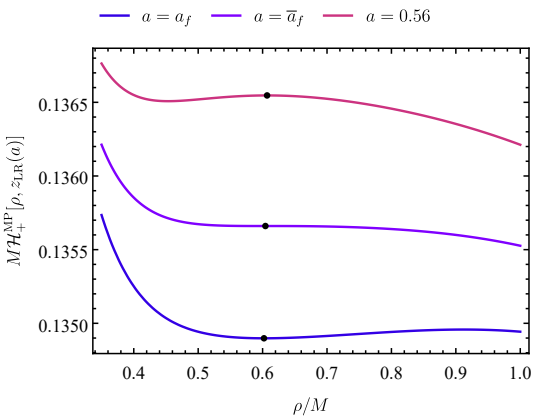

Figure 4.5: Plot showing the potential $\mathcal{H}_+^{\rm MP}$, as a function of the ρ coordinate for $z = z_{\rm LR}(a)$. The critical points associated with LRs are highlighted with black points.

According to Table 4.1, the MP solution exhibits four LRs for any value of a within the range (a_i, a_f). Outside this range, there are only two LRs: equatorial when $a < a_i$, and off-equatorial when $a > a_f$. Since the TC is additive, the total TC is just the sum of the individual TCs. Hence, for all values of a, the MP binary has TC$=-2$, in accordance with Ref. [165].

The variation in the number of LRs within the MP solution is associated with the coalescence of the $+1$ LR with one or more of the -1 LRs. As a approaches a_f, the two equatorial LRs converge and annihilate each other due to their opposite TCs, resulting in the disappearance of LRs at the equator. Conversely, as a approaches a_i, the $+1$ LR merges with the two off-equatorial plane LRs. The combined TC of these three merging LRs results in a single LR with a TC of -1. The interpolation between these two LR coalescing configurations can be visualized in Fig. 4.6. In all the three cases, namely $a < a_i$, $a_i < a < a_f$ and a_f, the total TC is always equal to -2, which could not have been different, since the boundary conditions of the solution are not changed.

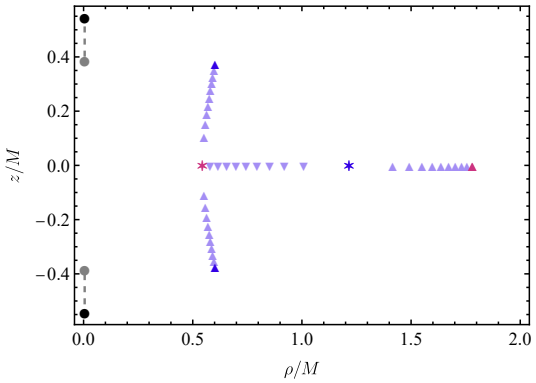

Figure 4.6: Positions of the LRs in the 2-center MP solution as the parameter a varies. For $a = a_i$, the BHs are located at the gray circles. The corresponding LRs are represented by a pink six-pointed star and a triangle. The triangle denotes the external equatorial LR with TC $= -1$, while the six-pointed star indicates a three-fold superposition of LRs, also with TC $= -1$. As the distance between the BHs increases, the six-pointed star splits into three distinct LRs: two are represented by purple upright triangles moving away from the equator, each with TC $= -1$, and the third by purple inverted triangles moving along the equator with TC $= +1$. For $a = a_f$, the BHs positions are represented by the black circle, the off-equatorial LRs reach the positions indicated by the dark blue triangles, and the two equatorial LRs merge at the position of the blue six-pointed star.

The LR positions in the closest configuration with $a < a_i$ closely resemble those found in a single BH solution, with the LRs confined to the equatorial plane. In contrast, when the BHs are taken apart beyond the critical distance a_f, the system exhibits a LR profile characteristic of two BHs, each with its own LR. The regime where $a_i < a < a_f$ represents a transitional phase between these two qualitatively distinct LR structures.

LRs represent a specific example of null trajectories within a larger family of orbits, termed FPOs. Broadly speaking, a FPO is a bound photon trajectory that neither falls into the BHs nor escapes to infinity [110]. Such orbits for the MP spacetime were analyzed in Ref. [207]. In Fig. 4.7, we represent photon trajectories as curves in $\mathbb{E}^3$ using cylindrical coordinates (ρ, z, φ). The LRs (black circles) are shown along with other null geodesics (colored lines) that lie within a vertical plane, i.e., $\varphi = 0$. The LRs depicted here correspond exactly to those in the second panel of Fig. 4.4.

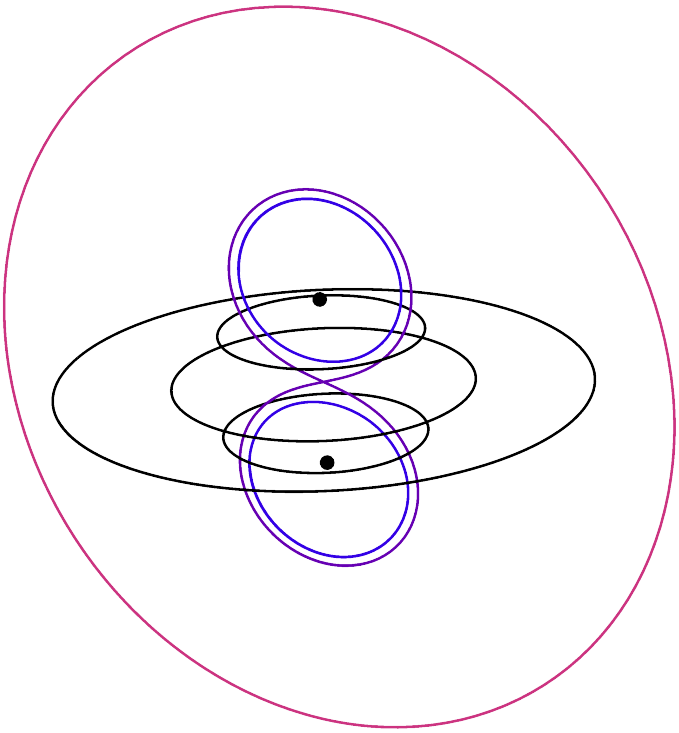

Figure 4.7: FPOs in the 2-center MP spacetime for $a/M = 0.5$. Black points indicate the BHs, black circles mark the LRs, as displayed in Fig. 4.4 and colored lines show additional bounded null trajectories.

4.4.2 Teo-Wan null orbits

The LR structure of the TW solution is significantly more complex than that of the MP case discussed above. With the introduction of angular momentum into the system, the potentials $\mathcal{H}_{\pm}^{\mathrm{TW}}$ for the TW spacetime no longer differ merely by a global sign, and are now given by

$$\mathcal{H}_{\pm}^{\mathrm{TW}} = \frac{1}{\pm\rho\sqrt{H_+H_-} - \omega_\varphi^0}, \tag{4.30}$$

and the associated vector field $\mathbf{v}_{\pm}^{\mathrm{TW}}$ can be written as

$$\left(\mathbf{v}_{\pm}^{\mathrm{TW}}\right)_j = \frac{\sqrt{H_+H_-}\partial_j\omega_\varphi^0 \mp \left[\delta_j^\rho + (\rho/2)\partial_j\right] H_+H_-}{(H_+H_-)^{3/4}\left(\omega_\varphi^0 \mp \rho\sqrt{H_+H_-}\right)^2}, \tag{4.31}$$

where $j = \rho, z$ and $\left(\mathbf{v}_{\pm}^{\mathrm{TW}}\right)_j$ denotes the j-th component of $\mathbf{v}_{\pm}^{\mathrm{TW}}$.

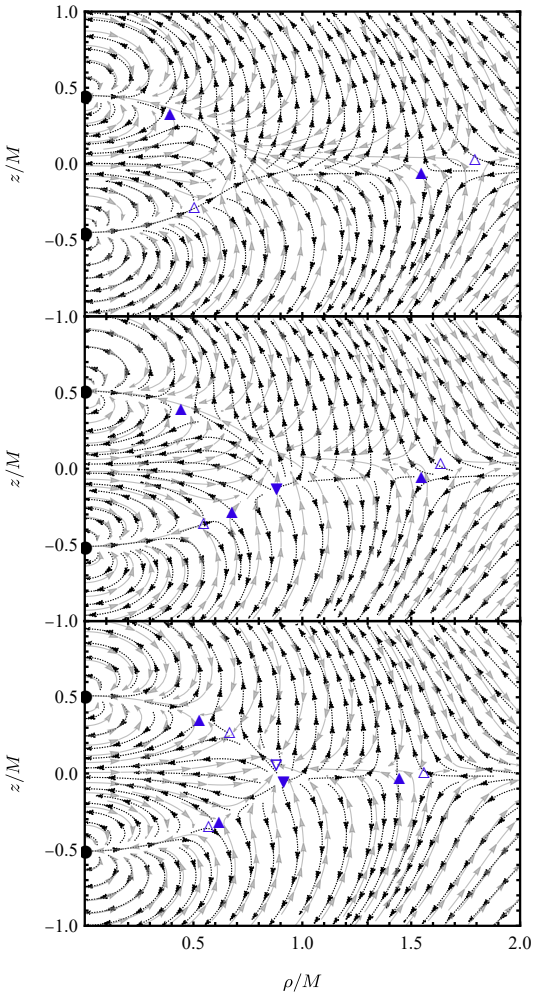

Figure 4.8: Vector fields $\mathbf{v}_+^{\mathrm{TW}}$ (dotted black) and $\mathbf{v}_-^{\mathrm{TW}}$ (gray) are shown on the (ρ, z)-plane with parameters $J_1 = 0$, $J_2 = J$, and $(a/M, J/M^2)$ values of $(0.45, 0.2)$ (top), $(0.51, 0.17)$ (middle), and $(0.51, 0.07)$ (bottom). Blue upright triangles mark the positions of LRs with a TC of -1, with filled triangles representing LRs obtained from $\mathcal{H}_+^{\mathrm{TW}}$ and empty triangles from $\mathcal{H}_-^{\mathrm{TW}}$. Similarly, the inverted triangles indicate the location of a LR with a TC of $+1$, with filled and empty markers denoting LRs from $\mathcal{H}_+^{\mathrm{TW}}$ and $\mathcal{H}_-^{\mathrm{TW}}$, respectively.

We remark that the total TC, for each $\mathcal{H}_\pm^{\mathrm{TW}}$, remains the same as in the MP spacetime, regardless of the values of J_1 and J_2, as the boundary conditions are unchanged. Hence, although the LRs change position with different choices of angular momentum, their total TCs must still sum to -2.

In the MP case there is a maximum of 4 LRs. However, since the potentials $\mathcal{H}_\pm^{\mathrm{TW}}$ are no

longer related by a simple global sign, the TW spacetime may exhibit more than four LRs. In Fig. 4.8, we show cases with 4, 6, and 8 LRs, along with the vector fields plot of $\mathbf{v}_{\pm}^{\mathrm{TW}}$ for equal-mass BHs, where one BH is non-rotating, while the other rotates.

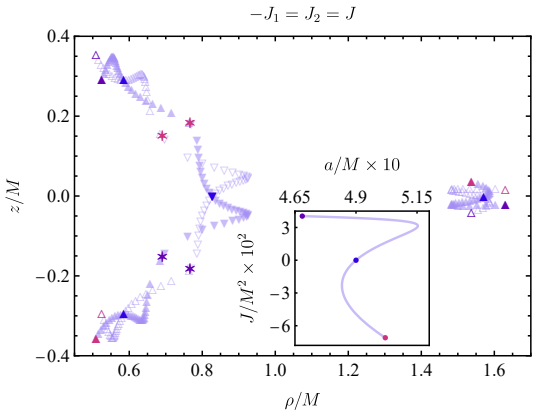

Figure 4.9: Variation in the positions of LRs of equal-mass, oppositely rotating BHs, with $-J_1 = J_2 = J$, as the parameters a and J change. Positions of LRs with a TC of -1 are indicated by upright triangles, where filled triangles correspond to those derived from $\mathcal{H}_{+}^{\mathrm{TW}}$ and empty triangles to those from $\mathcal{H}_{-}^{\mathrm{TW}}$. In contrast, inverted triangles mark the locations of LRs with a TC of $+1$, with filled and empty inverted triangles representing LRs from $\mathcal{H}_{+}^{\mathrm{TW}}$ and $\mathcal{H}_{-}^{\mathrm{TW}}$, respectively. The six-pointed stars represent superposition of LRs with opposite TCs.

In Fig. 4.9, we present an analogous plot to Fig. 4.6 for the TW spacetime, showing how the positions of LRs change as we vary the solution parameters. We consider equal-mass, oppositely rotating BHs, *i.e.* $M_1 = M_2 = M$ and $-J_1 = J_2 = J$. A curve in the parameter space $a \times J$ is shown in the inset of Fig. 4.9. The corresponding LR locations are plotted on the $\rho \times z$ plane, with colors that match those in the parameter space. For example, the purple point in the parameter space corresponds to the LR configuration marked by the purple triangles and inverted triangles.

The TW solution allows for a minimum of 2 LRs and a maximum of 4 LRs for each potential, $\mathcal{H}_{\pm}^{\mathrm{TW}}$. Consequently, the total number of LRs, for $J_1 \neq 0$ or $J_2 \neq 0$, will always be 4, 6, or 8. As in the MP case, changes in the number of LRs arise from the coalescence of LRs with different TCs. Given that the TW solution has 5 parameters, verifying all possible cases that result in 4, 6, or 8 LRs is significantly more challenging. Therefore, we restrict

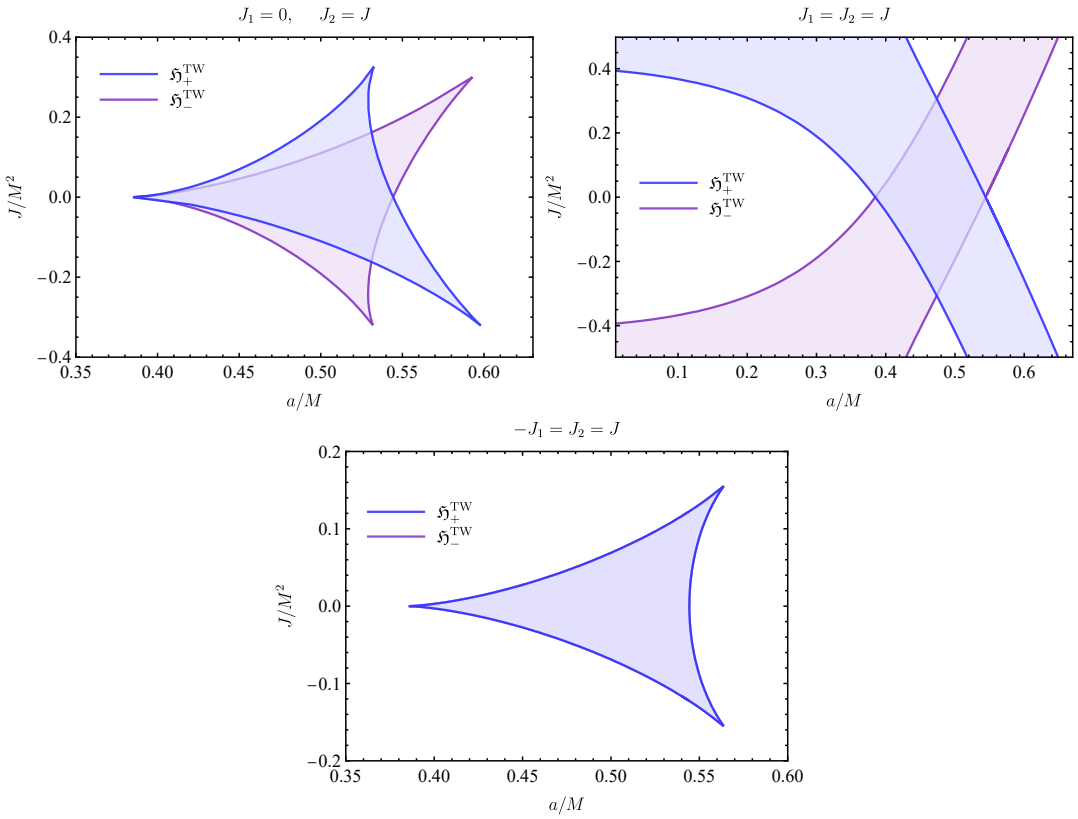

Figure 4.10: Parameter space highlighting regions with 4, 6 and 8 LRs for equal-mass BHs with $J_1 = 0,\ J_2 = J$ (top); $J_1 = J_2 = J$ (middle) and $-J_1 = J_2 = J$ (bottom). In the white regions, the total number of LRs is 4. In the blue and purple regions without overlap, there are 6 LRs. In the overlapping blue and purple regions, the total number of LRs is 8.

our analysis to equal-mass BHs and to three different configurations for angular momentum: $(i) J_1 = 0,\ J_2 = J$; $(ii) J_1 = J_2 = J$ and $(iii) - J_1 = J_2 = J$. This approach leaves us with only two free parameters, namely a and J.

In Fig. 4.10, we show the regions of the parameter space corresponding to 4, 6, and 8 LRs (except for the trivial cases of $J = 0$ and $a < a_i$, or $J = 0$ and $a > a_f$, where we recover the 2 or 4 LRs of the MP solution discussed in Sec. 4.4.1). The white regions indicate areas where both potentials, $\mathcal{H}_\pm^{\rm TW}$, each contribute with 2 LRs. In the dark blue (light purple) region, $\mathcal{H}_+^{\rm TW}$ ($\mathcal{H}_-^{\rm TW}$) yields 4 LRs, while $\mathcal{H}_-^{\rm TW}$ ($\mathcal{H}_+^{\rm TW}$) produces only 2. In the overlapping regions, both potentials yield 4 LRs each.

For the case $J_1 = 0,\ J_2 = J$, and $-J_1 = J_2 = J$ we notice that the boundary is composed

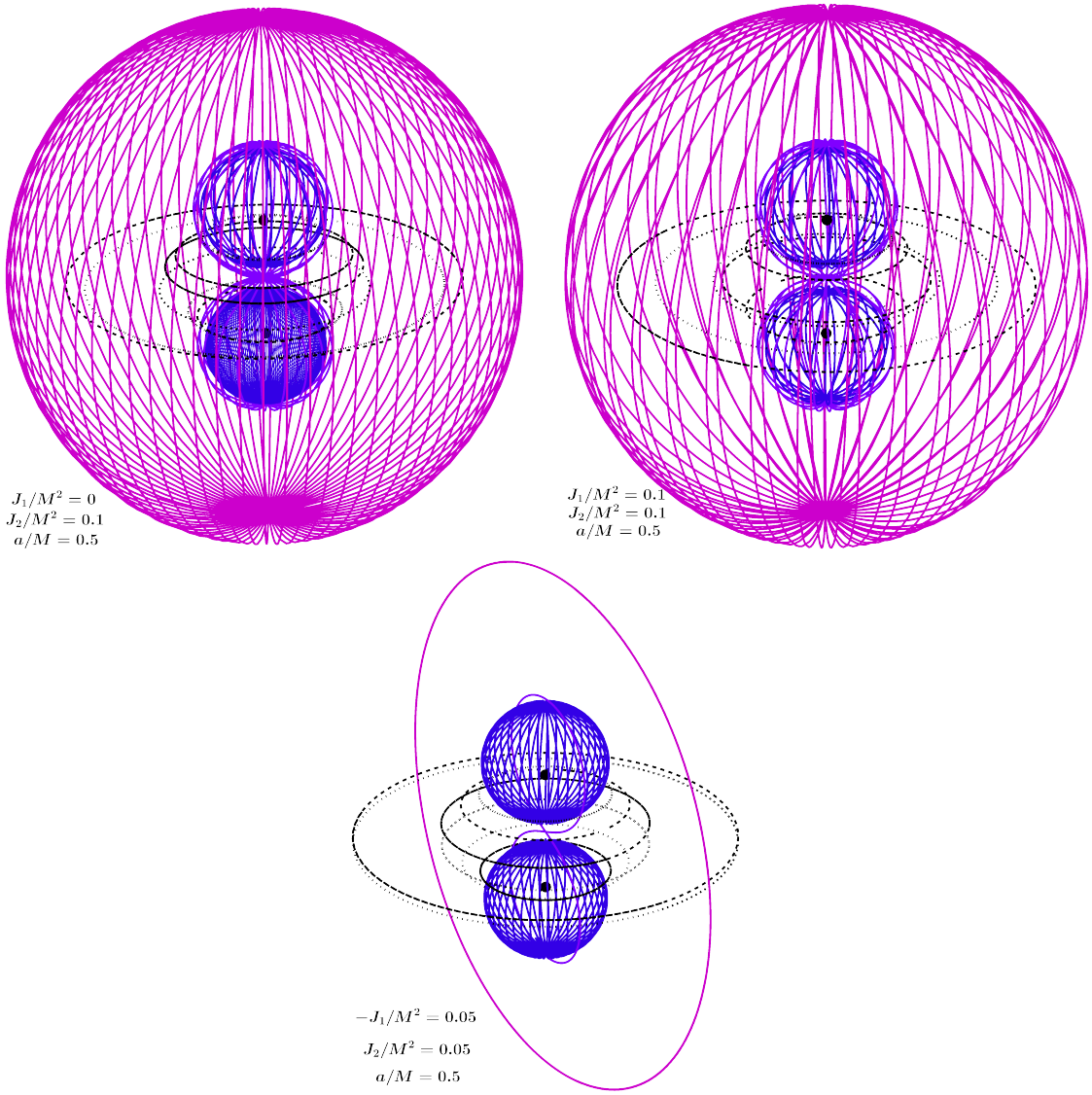

Figure 4.11: FPOs in the TW spacetime for $a/M = 0.5$ and three different angular momentum configurations. Black points indicate the BHs, black dashed ($H_+^{\rm TW}$) and dotted ($H_-^{\rm TW}$) orbits mark the LRs and colored lines, analogous to the colored lines exhibited in Fig. 4.7, show additional bounded null trajectories.

of three different smooth pieces. This boundary represents critical values of (a, J) where the number of LRs contributed by one potential changes from 2 to 4, or vice versa. Each smooth boundary segment corresponds to the coalescence of the $+1$ LR with one of the three -1 LRs.

For oppositely rotating BHs, the blue and purple regions coincide, even if the potentials

$\mathcal{H}^{\rm TW}_{\pm}$ are not identical. This overlap arises due to the symmetry of the parameter space along the horizontal axis $J = 0$, which prevents configurations with a total of 6 LRs.

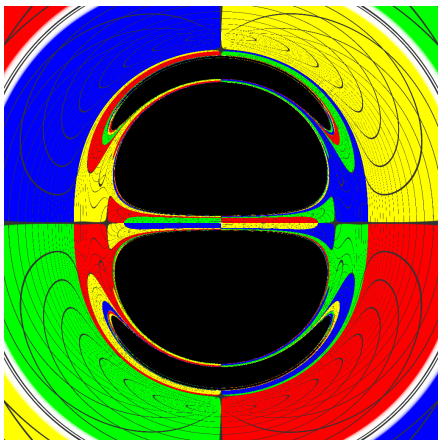

Figure 4.12: Shadow and gravitational lensing of the equal-mass MP solution. The observer is positioned at the equatorial plane ($z = 0$) and at the radius $\rho = 15M$.

We also computed some FPOs of the TW spacetime, as shown in Fig. 4.11. Black points represent the BHs, with light trajectories shown in both colored and black lines. Dotted lines indicate LRs derived from $\mathcal{H}^{\rm TW}_{+}$, while dashed lines correspond to LRs from $\mathcal{H}^{\rm TW}_{-}$. Each image serves as a natural generalization of Fig. 4.7, illustrating how photon trajectories are influenced by different configurations of BH angular momentum. Each colored FPO in Fig. 4.7 assumes some sort of 3 dimensional rotated version in Fig. 4.11. The external pink orbit "sees" the binary as almost a single gravitational center, whereas the internal purple and blue orbits see each center individually.

In configuration (i), with $J_1 = 0$ (top left), the blue trajectory is asymmetric with respect to the plane $z = 0$. In this setup, light rays are strongly dragged near the top BH, which carries angular momentum $J_2/M^2 = 0.1$, compared to the bottom BH with $J_1 = 0$. As a result, rays above $z = 0$ are more widely spaced, while trajectories below $z = 0$ are more closely clustered.

In contrast, cases (ii) and (iii) exhibit blue light rays that are more symmetric with respect to the equatorial plane, due to the spacetime's reflection symmetry across this plane. Additionally, in case (iii), involving oppositely rotating BHs, the LRs of $\mathcal{H}^{\rm TW}_{+}$ always share the same ρ coordinate with a corresponding LR of $\mathcal{H}^{\rm TW}_{-}$, which is symmetrically reflected

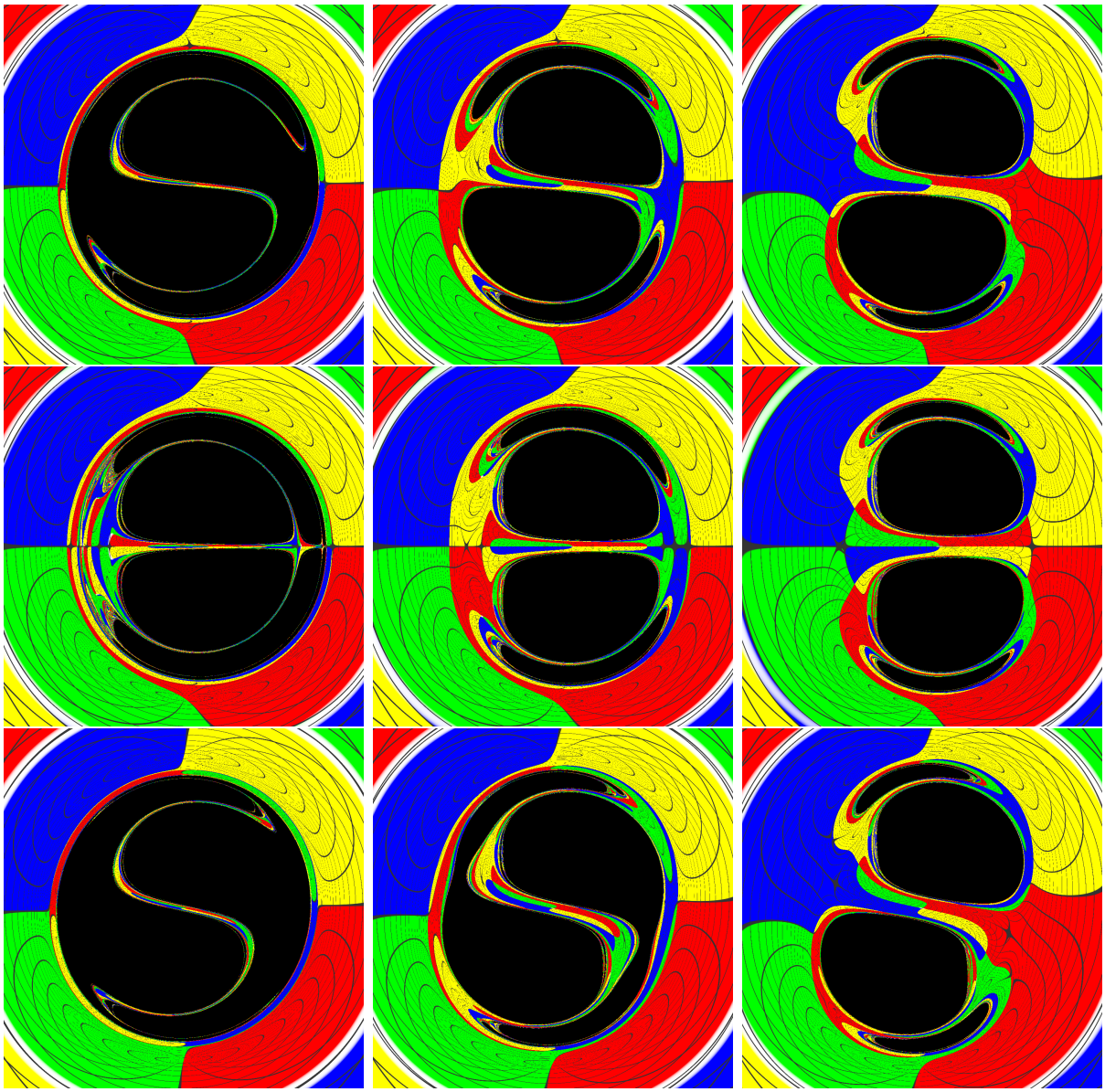

Figure 4.13: Shadow and gravitational lensing of the rapdily rotating ($J \approx J_{\rm e}$) TW solution, starting with equal-mass MP solution and increasing the coordinate distance parameter a for three different angular momentum configurations, namely the cases (i), (ii) and (iii) discussed in Sec. 4.4.2. In all the images, the observer is positioned at the equatorial plane ($z = 0$) and at the radius $\rho = 15M$.

across the plane $z = 0$. This is a special feature of *odd* $\mathbb{Z}_2$ symmetric spacetimes, which was discussed in more detail in Appendix A [208].

It is worth noting that in configuration (iii), although the purple and pink trajectories

appear to be confined to a vertical two-dimensional plane, this is not the case. The opposite angular momenta prevent these trajectories from developing the three-dimensional structure observed in configurations (i) and (ii). However, there are frame dragging effects that add to the trajectories a wiggly appearance, which deviates from the behavior obtained in Fig. 4.7.

4.5 Shadow and gravitational lensing

Here, we analyze the shadow and gravitational lensing effects associated with the TW solution. In spacetimes where geodesic equations are not integrable, which seem to be the case of the metric (4.14), numerical techniques like backward ray-tracing are very useful. Hence the set up here is very similar to the one presented in Sec. 3.4.

The initial conditions for this integration are derived by projecting the photon's momentum onto the observer's tetrad frame—details of which can be found in Ref. [115]. The initial conditions for a ZAMO frame are given by

$$E = \frac{(H_+H_-)^{1/4}}{\sqrt{\rho^2 H_+H_- - \omega_\varphi^{0\,2}}}\left(\rho + \frac{\omega_\varphi^0 \cos\alpha \sin\beta}{\sqrt{H_+H_-}}\right), \tag{4.32}$$

$$p_\rho = (H_+H_-)^{1/4}\cos\alpha\cos\beta, \tag{4.33}$$

$$p_z = (H_+H_-)^{1/4}\sin\alpha, \tag{4.34}$$

$$L = \frac{\sqrt{\rho^2 H_+H_- - \omega_\varphi^{0\,2}}}{(H_+H_-)^{1/4}}\cos\alpha\sin\beta, \tag{4.35}$$

where α, β are the observation angles and Eqs. (4.32)-(4.35) must be evaluated at the observer coordinates.

The initial conditions for the photons are determined by the observation angles.

4.5.1 Equatorial plane images

We display in Fig. 4.12 the case $J/M^2 = 0$, which corresponds to the MP subcase with $a/M = 1$, to provide a consistent reference. Althought the shadows of MP and double-Schwarzschild are significantly similar (see Figure 2 of Ref. [209]), the MP image does not

exhibit the discontinuity on the lensing as it does for the double-Schwarzschild, since there are no conical singularities.

Figure 4.13 presents the shadows and gravitational lensing of the TW solution for an observer located on the equatorial plane ($z = 0$) at a radial coordinate of $\rho = 15M$. The three rows correspond to the angular momentum configurations (i), (ii), and (iii) described in 4.4.2, respectively. To calculate the images we fix the magnitude of the angular momentum to $J/M^2 = 0.499 \approx J_e/M^2$. For each configuration, the coordinate distance parameter a takes three values: $a/M = 0.5$, 1.0, and 1.5, with the distance increasing from left to right along each row.

The shadows reveal no significantly novel characteristics and it seems hard to distinguish them from the double-Kerr [210]. In particular, the characteristic 'eyebrows' [207, 211, 212], located above and below each primary shadow, are a typical feature of double-BH configurations.

These features appear in simulations as secondary shadows, which are more clearly visualized in Fig. 4.14. For illustration, the top panel shows an equatorial observer facing equal-mass MP BHs, with $a/M = 0.5$. We display a vertical cross-section of light rays corresponding to each shadow seen in Fig. 4.13. The group of geodesics that either fall into the bottom BH or end on the FPO surrounding it corresponds to the primary shadow of the bottom BH. This group is highlighted in gray regions in the top panel of Fig. 4.14, with boundaries marked by black dashed lines. Similarly, geodesics bounded by the dotted line either fall into the top BH or become trapped by its nearby FPO, forming a secondary shadow below the primary shadow. This secondary shadow, or the bottom eyebrow, is much thinner due to the smaller viewing angle of these geodesics. A similar and even thinner shadow layer, associated with the dot dashed line, exists below this bottom eyebrow, associated with the bottom BH. This pattern repeats infinitely, creating a fractal-like structure of nested shadows.

The first row, which represents case (i), the bottom BH has $J = 0$. The eyebrows become significantly larger when the BHs possess angular momentum. Hence, its shadow looks distorted only by frame dragging effects of the top BH and is not, as expected, $\mathbb{Z}_2$ symmetric.

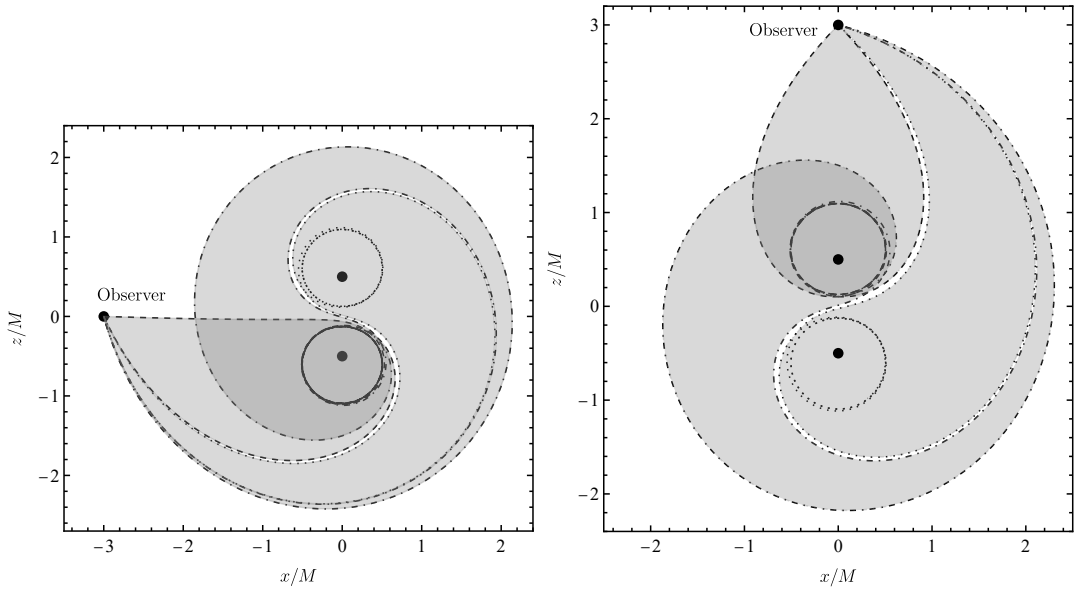

Figure 4.14: Light trajectories corresponding to the eyebrow features of the MP's shadow with two BHs. In the top panel, the observer is located at the equator, while in the bottom panel, the observer is positioned above the BHs.

In contrast with case (i), the cases (ii) and (iii) have shadows that are even and odd $\mathbb{Z}_2$ symmetric, respectively [208]. We additionally remark that the rotation effects on the shadows are more noticeable in case (iii), as the eyebrows merge with the primary shadows.

4.5.2 Off-equatorial plane images

Next, we examine the shadow and gravitational lensing when the observer is positioned off the equatorial plane. For this analysis, we consider the near-maximum angular momentum $J \approx J_{\rm e}$ configuration for the same cases (i), (ii), and (iii) on each row. The observer's radial distance remains fixed, but the polar angle $\theta \equiv \arctan \frac{\varrho}{z}$ is varied, starting from $\theta = 0$ and ending at $\theta = \pi/2$. We use equal step increments of $\delta\theta = \pi/4$ in the observer's θ coordinate.

The simulated images are shown in Fig. 4.15. The leftmost image on each row corresponds to an observer positioned at the equator, as in previous analyses, for reference. The rightmost image shows the perspective from directly above the two BHs. Due to axial symmetry, the shadow boundary for $\theta = 0$ observer's forms a perfect circle at the center, representing the shadow of the top BH. The central portion of the shadow corresponds to geodesics within

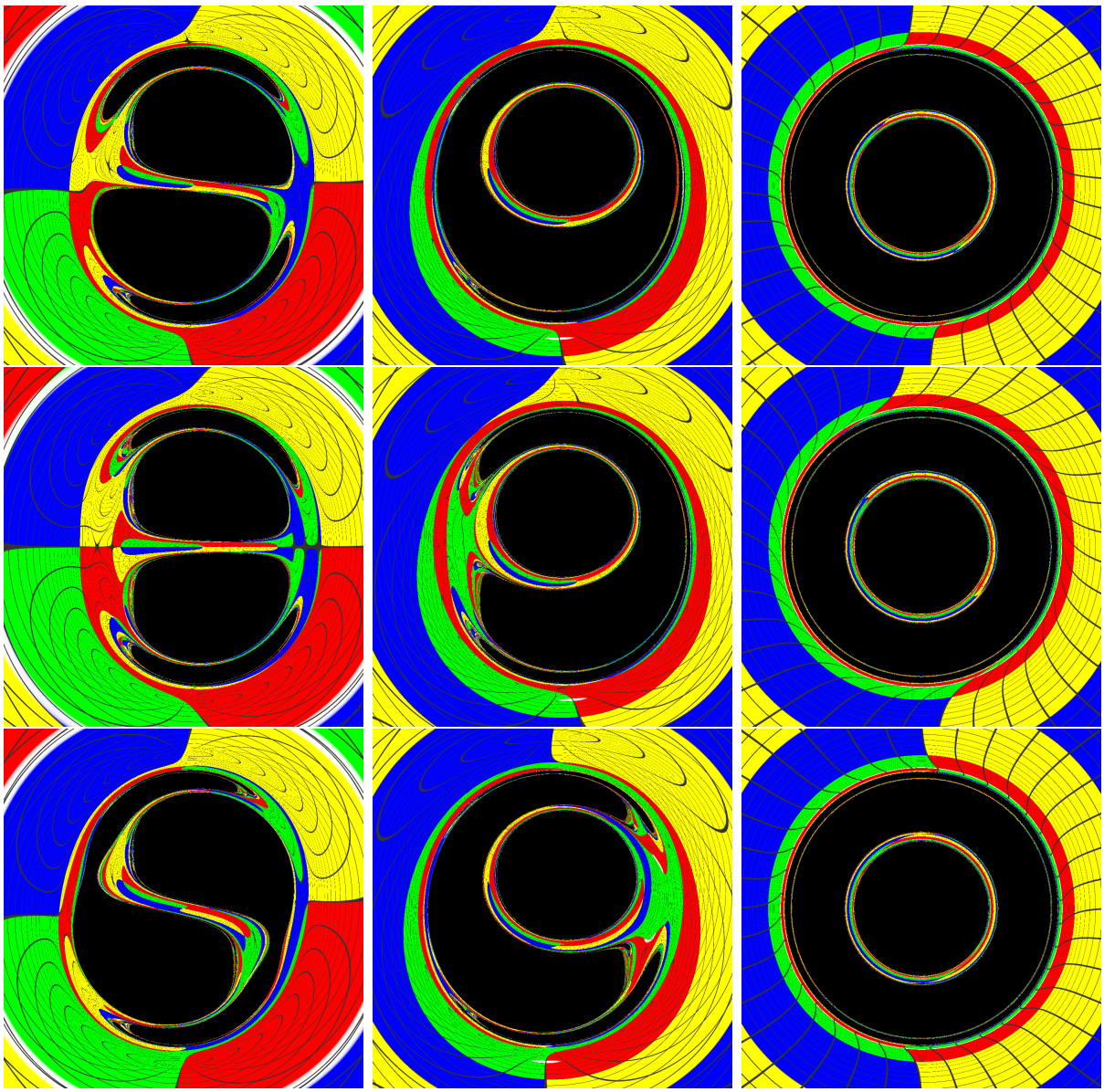

Figure 4.15: Shadow and gravitational lensing of the TW solution, starting with an observer at the equator for near-extremal $J \approx J_{\rm e}$ on the left of each row, corresponding to configurations (i), (ii), and (iii), respectively. Moving from left to right, the observer's position changes with increments of $\theta = \pi/4$ and ending at the top of the binary.

the gray region in Fig. 4.14, bounded by the dashed line, which are captured by the top BH. Surrounding this core shadow, there is a ring-shaped shadow created by the bottom BH, followed by a thinner outer ring associated with a secondary shadow of the top BH. These two ring-like shadows are related with ther dotted and dot dashed lines in Fig. 4.14, respectively. This nested structure of shadows and rings continues infinitely, reflecting a similar repeating pattern seen in eyebrow formation.

4.6 Remarks

The TW spacetime [198] represents a novel class of exact solutions obtained in the context of KK theory, as a multi-center generalization of the RL BH [199, 200]. The TW solution is also a regular rotating generalization of MP solution, where the equilibrium established is ensured not only by the electromagnetic field, but also by the dilaton field. As is Refs. [189, 190], the presence of a scalar field is fundamental to achieve a proper equilibrium.

Our analysis of LRs focused on using the TC formalism to examine the various LR configurations across different parameter choices. We revisited the properties of the equal-mass MP spacetime through the lens of the TC method, exploring all possibilities within the parameter space. This leads to three distinct LR configurations: a compact setup with two equatorial LRs for $a < a_i$, a transient regime with four LRs—two of which are equatorial—for $a_i < a < a_f$, and a spread-out BH regime for $a > a_f$, featuring two LRs near each gravitating center. The transition between the regimes $a < a_i$ and $a > a_f$ is illustrated in Fig. 4.6, aiding in a clearer understanding of the process. Additionally, the stability of the LRs has been analyzed and summarized in Tab. 4.1.

In the rotating case, with five parameters, the LR structure becomes significantly richer than in the static scenario. The angular momentum splits each LR of the static case into two, one for each sense of rotation, resulting in a maximum of 8 LRs. However, LRs with opposite TC can merge and annihilate, leading to configurations with 6 or 4 LRs. Whether there are 4, 6, or 8 LRs depends on the choice of solution parameters. Focusing on equal-mass BHs and three specific angular momentum configurations, namely: $(i) : J_1 = 0, J_2 = J$; $(ii) : J_1 = J_2 = J$; and $(iii) : -J_1 = J_2 = J$, we mapped the parameter space and identified

all possible LR configurations (see Fig. 4.10).

We also calculated some FPOs for the TW spacetime and compared them with those previously reported for the MP spacetime. As before, we focused on the specific angular momentum configurations (*i*), (*ii*), and (*iii*). The MP orbits shown in Fig. 4.7, initially confined to a vertical plane, become frame-dragged when angular momentum is introduced, transforming into the orbits displayed in Fig. 4.11. Notably, the pink and purple orbits in Fig. 4.11, for oppositely rotating BHs appear to lie within a vertical plane; however, due to the dragging effect, this is not the case. As these orbits evolve, they experience dragging in opposite directions, ultimately forming a 1-dimensional submanifold.

We also investigated the shadows and gravitational lensing of the TW solution. In non-integrable spacetimes, as the TW binary seems to be, the geodesic equations cannot be separated, making analytical shadow calculations not possible in a general context. Instead, shadows can be determined through numerical simulations using backward ray-tracing techniques. The shadow's 'eyebrows' grow significantly when the BHs have angular momentum, and its shape adopts a D-like appearance, similar to that of the double-Kerr spacetime. While the TW and double-Kerr spacetimes may differ in many respects, they share similar shadow characteristics.

Appendix A

General considerations regarding $\mathbb{Z}_2$ symmetry and null geodesic motion

A.1 Definition of odd $\mathbb{Z}_2$ symmetry

The goal of this Appendix is to define the odd $\mathbb{Z}_2$ symmetry and put it in contrast with the usual (even) $\mathbb{Z}_2$ symmetry. The $\mathbb{Z}_2$ symmetry is associated with a particular type of symmetry operation involving some kind of inversion of a physical system. This type of transformation is mathematically represented by the action of the cyclic group of order 2, $\mathbb{Z}_2$ [213].

Let $(\mathcal{M}, g_{\mu\nu})$ be a 4-dimensional, stationary, axisymmetric, circular spacetime. For this class of spacetimes, we can parameterize the non-Killing submanifold by the coordinates $r \in (r_h, \infty)$ and $\theta \in (0, \pi)$, where $r = r_h$ is the horizon surface. Under these assumptions, the spacetime metric can be written as

$$ds^2 = g_{tt}dt^2 + 2g_{t\varphi}dtd\varphi + g_{\varphi\varphi}d\varphi^2 + g_{rr}dr^2 + g_{\theta\theta}d\theta^2. \tag{A.1}$$

In the context of BH physics, or more generically, of localized compact objects, the action of $\mathbb{Z}_2$ is commonly related with the reflection transformation $\theta \to \theta_R := \pi - \theta$, which intuitively amounts to swapping the "north" and the "south" hemispheres. Spacetimes that are symmetric under such reflection, *i.e.*

$$\forall(\mu, \nu) : g_{\mu\nu}(r, \theta) = g_{\mu\nu}(r, \theta_R), \tag{A.2}$$

are called $\mathbb{Z}_2$ symmetric and the fixed point $\theta = \pi/2$ is the equatorial plane. The Kerr spacetime, as well as all spherically symmetric spacetimes are examples of $\mathbb{Z}_2$ symmetric spacetimes. But there are well known non-$\mathbb{Z}_2$ symmetric spacetimes, which have been studied in the context of light propagation [200, 214, 215].

The SBHSU is not $\mathbb{Z}_2$ symmetric, but it has the discrete symmetry defined by

$$(t, \theta) \to (-t, \theta_R). \tag{A.3}$$

That is, the metric is invariant under exchanging north and south *and* simultaneously the direction of the time coordinate. We will dub the spacetime with the symmetry defined by Eq. (A.3) as *odd* $\mathbb{Z}_2$ *symmetric*, whereas the standard $\mathbb{Z}_2$ symmetry will be referred as *even* $\mathbb{Z}_2$ *symmetry*. The SBHSU is also invariant under the same discrete transformation as (say) Kerr, namely $(t, \varphi) \to (-t, -\varphi)$; its distinctive feature is that it is *not* invariant under the standard (even) $\mathbb{Z}_2$ symmetry $\theta \to \theta_R$; it requires the additional transformation present in Eq. (A.3).

For odd symmetric spacetimes, we can still define the equatorial plane as the set of points which are fixed by the θ-reflection. Hence, the top submanifold $0 < \theta < \pi/2$ is isometric do the bottom spacetime patch $\pi/2 < \theta < \pi$, under time reversal for one of them. Equation (A.3) could also be written with a reflection in φ instead of t. The symmetry defined in Eq. (A.3) holds true for any spacetime with metric components invariant under θ-reflection, except for the $g_{t\varphi}$ component, which must pick up a minus sign. Therefore, an equivalent definition of an odd $\mathbb{Z}_2$ (symmetric) spacetime can be given, in the above metric chart, in terms of metric components transformations as follows:

$$\forall(\mu, \nu) \neq (t, \varphi) : g_{\mu\nu}(r, \theta) = g_{\mu\nu}(r, \theta_R), \tag{A.4}$$

$$g_{t\varphi}(r, \theta) = -g_{t\varphi}(r, \theta_R). \tag{A.5}$$

Thus, the reflection in t (or φ) corrects the "wrong" sign of the $g_{t\varphi}$ component. Moreover, any spacetime with the symmetry defined by Eq. (A.3) must have $g_{t\varphi}|_{\theta=\pi/2} = 0$, since $g_{t\varphi}$ is an odd function with respect to the plane $\theta = \pi/2$.

Apart from the SBHSU, another example of spacetime that is odd $\mathbb{Z}_2$ symmetric is the Taub-NUT BH.

A.2 The potentials $\mathcal{H}_\pm$

It is possible to express the potentials $\mathcal{H}_\pm$ purely in terms of the metric components according to Eq. 4.26. One may check that Eq. (4.26) agrees with Eq. (3.43) when the metric components are given by Eq. (3.17).

The symmetry relation in Eq. (3.45) between the potentials $\mathcal{H}_\pm$ is true for any spacetime that is symmetric under action of Eq. (A.3). This can be shown as follows:

$$\begin{aligned}\mathcal{H}_\pm(r,\theta) &= \frac{-g_{t\varphi}(r,\theta) \pm \sqrt{g_{t\varphi}(r,\theta)^2 - g_{tt}(r,\theta)g_{\varphi\varphi}(r,\theta)}}{g_{\varphi\varphi}(r,\theta)} \\ &= -\frac{-g_{t\varphi}(r,\theta_R) \mp \sqrt{g_{t\varphi}(r,\theta_R)^2 - g_{tt}(r,\theta_R)g_{\varphi\varphi}(r,\theta_R)}}{g_{\varphi\varphi}(r,\theta_R)} \\ &= -\mathcal{H}_\mp(r,\theta_R).\end{aligned} \tag{A.6}$$

Eq. (A.6) shows that, for odd $\mathbb{Z}_2$ symmetric spacetimes, the potential $\mathcal{H}_-$ can be fully constructed from the $\mathcal{H}_+$ potential and vice-versa, which is not true for even $\mathbb{Z}_2$ symmetric spacetimes.

A.3 Equatorial light rings

It is interesting to investigate the relation between even $\mathbb{Z}_2$ symmetry and LRs positioned on the equator, assuming a single BH with spherical topology. This can be simply addressed for spacetimes possessing the same properties mentioned in the preceding section plus asymptotically flatness.

Let $\tilde{\mathcal{H}}_\pm$ be null geodesic potentials of a BH with such properties. LRs are critical points of the potentials $\tilde{\mathcal{H}}_\pm$, *i.e.* the LR position $(\tilde{r}_\pm, \tilde{\theta}_\pm)$ is defined by $\nabla\tilde{\mathcal{H}}_\pm(\tilde{r}_\pm, \tilde{\theta}_\pm) = 0$. From the first three hypotheses we obtain

$$\forall\theta \in \mathscr{I} \subset (0,\pi)\ \exists\ \tilde{r}_\pm \in (r_h,\infty):\ \frac{\partial\tilde{\mathcal{H}}_\pm(\tilde{r}_\pm,\theta)}{\partial r} = 0, \tag{A.7}$$

where $\mathscr{I}$ is an open interval that includes $\pi/2$. In fact, for asymptotically flat spacetimes, a stronger version of the condition (A.7) is satisfied, which is valid for all values of $\theta \in (0,\pi)$ and not only for an open neighborhood of $\pi/2$. With this assumption, one can also show that there is a odd number of $\tilde{r}_\pm$'s satisfying Eq. (A.7).

Now, imposing the even $\mathbb{Z}_2$ symmetry, we obtain that

$$\forall\theta \in \mathscr{I} \subset (0,\pi): \ \frac{\partial\tilde{\mathcal{H}}_{\pm}(r,\theta)}{\partial\theta} = -\frac{\partial\tilde{\mathcal{H}}_{\pm}(r,\pi-\theta)}{\partial\theta}. \tag{A.8}$$

In particular, we may choose $\theta = \pi/2$ in Eq. (A.8), from where we get $\partial\tilde{H}_{\pm}(r,\pi/2)/\partial\theta = 0$. Therefore, the following "formal" implication is true:

$$\text{even } \mathbb{Z}_2 \Rightarrow \exists \text{ LR at } \theta = \pi/2. \tag{A.9}$$

Alternatively, we could have calculated the gradient of Eq. (4.26) and evaluated at the equatorial plane. If the spacetime is even $\mathbb{Z}_2$ symmetric, the metric components should be even functions with respect to the equator, according to Eq. (A.2). Thus, their corresponding derivatives with respect to θ are odd functions, which implies Eq. (A.9).

It also holds the contrapositive of Eq. (A.9), which states that the absence of a LR at $\theta = \pi/2$ implies that the corresponding spacetime is not even $\mathbb{Z}_2$ symmetric, *i.e.*

$$(\nexists \text{ LR at } \theta = \pi/2) \Rightarrow \neg(\text{even } \mathbb{Z}_2). \tag{A.10}$$

We remark, however, that *it is not true* in general that: $(\exists$ LR at $\theta = \pi/2) \Rightarrow$ even $\mathbb{Z}_2$, since is easy to construct examples of spacetimes with a LR at the equatorial plane, which are not even $\mathbb{Z}_2$ symmetric. Both Eqs. (A.9) and (A.10) are only valid for asymptotically flat spacetimes.

Therefore, at least for the asymptotically flat cases, the relation between even $\mathbb{Z}_2$ symmetry and equatorial LRs - assuming a single BH[1] - is already well established. For other asymptotics, Eq. (A.7) is not necessarily true. For instance, considering a BH which is asymptotically Melvin, the existence of critical points in the radial direction is determined by the strength of the magnetic field. If the magnetic field is weak (subcritical regime), then Eq. (A.7) is satisfied, but for strong magnetic fields (supercritical regime) it is not [107]. Nevertheless, the condition (A.7) is necessary in order to have an equatorial LR in the first place, thus the general conclusion is: *for any stationary, axisymmetric, even* $\mathbb{Z}_2$ *symmetric,*

[1]The point here is that for, say, a 2-centre solution, *e.g.* the 2-centre Majumdar-Papapetrou solution, there needs not to be a LR on the equatorial plane. The loophole in such cases is because the horizon is multi-connected, and therefore it does not have spherical topology as assumed in Ref. [105] to compute the TC; it is rather a product of spheres.

(single) BH spacetime where Eq. (A.7) *is satisfied, there exists one LR lying on the equatorial plane.*

As we shall see, when we assume odd $\mathbb{Z}_2$ symmetry, the result is different. The odd symmetry implies that the metric components should transform according to Eqs. (A.4) and (A.5). Thus, we have that

$$\forall(\mu,\nu)\neq(t,\varphi):\frac{\partial g_{\mu\nu}(r,\theta)}{\partial\theta}=-\frac{\partial g_{\mu\nu}(r,\theta_R)}{\partial\theta}, \tag{A.11}$$

$$\frac{\partial g_{t\varphi}(r,\theta)}{\partial\theta}=\frac{\partial g_{t\varphi}(r,\theta_R)}{\partial\theta}. \tag{A.12}$$

From Eqs. (A.11) and (A.12) we may infer that $\forall(\mu,\nu)\neq(t,\varphi):\partial g_{\mu\nu}(r,\pi/2)/\partial\theta=0$, but nothing can be concluded for the component $g_{t\varphi}(r,\pi/2)$.

Let $\overline{\mathcal{H}}_{\pm}$ be null geodesic potentials of an odd $\mathbb{Z}_2$ symmetric BH. Using Eqs. (A.5) and (A.11), we have that

$$\frac{\partial\overline{\mathcal{H}}_{\pm}(r,\pi/2)}{\partial\theta}=-\frac{\partial g_{t\varphi}(r,\pi/2)/\partial\theta}{g_{\varphi\varphi}\,(r,\pi/2)}. \tag{A.13}$$

As we did for the even-symmetric case, we may assume that Eq. (A.7) is true for $\overline{\mathcal{H}}_{\pm}$. Hence, we have a condition for the existence of LRs at the equator for odd $\mathbb{Z}_2$ spacetimes, which is given by

$$\frac{\partial g_{t\varphi}(r,\pi/2)}{\partial\theta}=0. \tag{A.14}$$

The interpretation of Eq. (A.14) is that the spacetime, despite the fact that it is odd $\mathbb{Z}_2$ symmetric, is locally even $\mathbb{Z}_2$ symmetric in a small neighborhood of the equator. For this to be accomplished, the $g_{t\varphi}$, which vanishes at the equatorial plane (see Eq. (A.5)), is also zero in a small vicinity of $\theta=\pi/2$. As we shall see in the next subsection, Eq. (A.14)) is also a condition for the equatorial plane to be a totally geodesic submanifold of an odd $\mathbb{Z}_2$ symmetric spacetime. Therefore, the existence of equatorial LRs for odd symmetric BHs is intimately related with how null geodesics deviate from the equatorial plane.

From Eq. (3.17), one can show that

$$\frac{\partial g_{t\varphi}(r,\pi/2)}{\partial\theta}=-\frac{4jr^2(r-2M)}{j^2r^4+1}\neq 0, \tag{A.15}$$

which shows that the SBHSU spacetime cannot have LRs at the equatorial plane. A similar analysis can be done for the Taub-NUT BH.

A.4 Equatorial totally geodesic submanifold

Let $\overline{\mathcal{M}}$ denote a submanifold of $\mathcal{M}$, defined by $\theta = \pi/2$. The induced metric $h_{\mu\nu}$ on $\overline{\mathcal{M}}$ (also known as the first fundamental form) is given by the expression $h_{\mu\nu} = g_{\mu\nu} - n_\mu n_\nu$. Let $n = \left(1/\sqrt{g_{\theta\theta}}\right)\partial_\theta$ be the normal unit vector to $\overline{\mathcal{M}}$. The extrinsic curvature $k_{\mu\nu}$ (or the second fundamental form) of the hypersurface $\overline{\mathcal{M}}$ is the symmetric tensor defined by

$$k_{\mu\nu} = \frac{1}{2}\mathscr{L}_n h_{\mu\nu}, \tag{A.16}$$

where $\mathscr{L}_n$ denotes the Lie derivative with respect to the normal vector n [216]. The spacetime patch $\overline{\mathcal{M}}$ of $\mathcal{M}$ is said to be a totally geodesic submanifold if observers in $\mathcal{M}$ see no curving in $\overline{\mathcal{M}}$, *i.e.* $k_{\mu\nu} = 0$ [217].

For a spacetime defined by the metric (A.1) we can calculate the extrinsic curvature explicitly. The pullback of the extrinsic curvature $k_{ab} = \left(\partial x^\mu/\partial x^a\right)\left(\partial x^\nu/\partial x^b\right) k_{\mu\nu}$[2] is given by

$$(k_{ab}) = \frac{1}{2\sqrt{g_{\theta\theta}}}\begin{pmatrix} \partial_\theta g_{tt} & 0 & \partial_\theta g_{t\varphi} \\ 0 & \partial_\theta g_{rr} & 0 \\ \partial_\theta g_{t\varphi} & 0 & \partial_\theta g_{\varphi\varphi} \end{pmatrix}. \tag{A.17}$$

For even $\mathbb{Z}_2$ symmetric spacetimes we have that

$$\begin{aligned} g_{\mu\nu}(\theta) = g_{\mu\nu}(\theta_R) &\Rightarrow \partial_\theta g_{\mu\nu}(\theta) = -\partial_\theta g_{\mu\nu}(\theta_R) \\ &\Rightarrow \partial_\theta g_{\mu\nu}(\pi/2) = 0, \end{aligned} \tag{A.18}$$

hence Eq. (A.17) vanishes, which satisfy the condition of extrinsic flatness.

Similarly, for odd $\mathbb{Z}_2$, one can infer that

$$\begin{aligned} &\forall(\mu,\nu) \neq (t,\varphi) : g_{\mu\nu}(\theta) = g_{\mu\nu}(\theta_R) \Rightarrow \partial_\theta g_{\mu\nu}(\pi/2) = 0, \\ &g_{t\varphi}(\theta) = -g_{t\varphi}(\theta_R) \Rightarrow \partial_\theta g_{t\varphi}(\theta) = \partial_\theta g_{t\varphi}(\theta_R). \end{aligned} \tag{A.19}$$

Therefore, the difference in this case is that the $\partial_\theta g_{t\varphi}(\theta)$ term does not necessarily vanish at the equatorial plane, which implies that, generically, for odd symmetric spacetimes, $k_{ab} \neq 0$. Nevertheless, those spacetimes can have an equatorial totally geodesic submanifold, as long as Eq. (A.14) is satisfied. In general, a necessary and sufficient condition for a spacetime

[2]Here, we are working under the assumption that Latin indices are limited to the set $\{t, r, \varphi\}$.

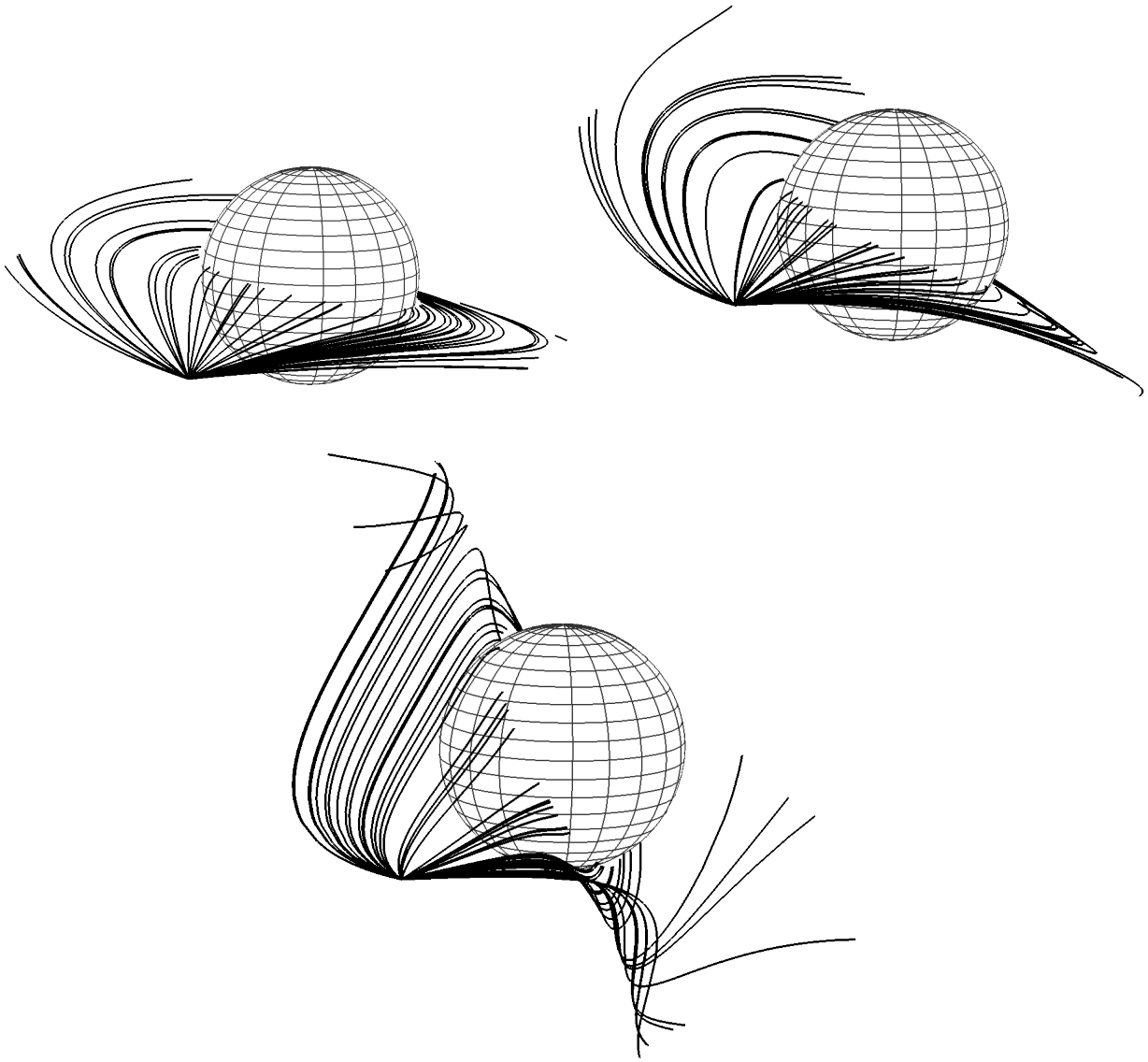

Figure A.1: Deviation of geodesics from the equatorial plane. We evolved, numerically, 50 null geodesics with initial conditions given by Eqs. (4.32)-(4.35), setting $\alpha = 0$, while β varies randomly.

(with metric given by Eq. (A.1)) to have an equatorial totally geodesic submanifold is to be locally even $\mathbb{Z}_2$ around the plane $\theta = \pi/2$.

An equivalent definition of totally geodesic submanifold is given in terms of geodesics. Let $T_p\mathcal{M}$ denote the tangent space of $\mathcal{M}$ at the point $p \in \mathcal{M}$. If, in a small interval $\lambda \in (-\epsilon, \epsilon) \subset \mathbb{R}$, a geodesic $\gamma(\lambda)$ of $\mathcal{M}$ with tangent vector $v \in T_{\gamma(\lambda)}\mathcal{M}$ have initial conditions given by $\gamma(0) \in \overline{\mathcal{M}}$ and $v \in T_{\gamma(0)}\overline{\mathcal{M}}$, lies in $\overline{\mathcal{M}}$, then $\overline{\mathcal{M}}$ is classified as a totally geodesic submanifold. Thus, every geodesic of $\overline{\mathcal{M}}$ must also be a geodesic of $\mathcal{M}$ [217].

To ensure consistency, let us demonstrate that a brief exploration of the geodesic equation results in identical criteria for the presence of an equatorial totally geodesic submanifold. Considering a spacetime characterized by the line element described in Eq. (A.1), we can derive the geodesic equation specifically for the θ coordinate as follows:

$$\ddot{\theta} + \Gamma^{\theta}_{tt}\dot{t}^2 + \Gamma^{\theta}_{rr}\dot{r}^2 + \Gamma^{\theta}_{\theta\theta}\dot{\theta}^2 + \Gamma^{\theta}_{\varphi\varphi}\dot{\varphi}^2 + 2\Gamma^{\theta}_{t\varphi}\dot{t}\dot{\varphi} + 2\Gamma^{\theta}_{r\theta}\dot{r}\dot{\theta} = 0, \tag{A.20}$$

where

$$\begin{aligned} \Gamma^{\theta}_{tt} &= -\frac{\partial_\theta g_{tt}}{2g_{\theta\theta}}, \quad \Gamma^{\theta}_{\varphi\varphi} = -\frac{\partial_\theta g_{\varphi\varphi}}{2g_{\theta\theta}}, \quad \Gamma^{\theta}_{t\varphi} = -\frac{\partial_\theta g_{t\varphi}}{2g_{\theta\theta}}, \\ \Gamma^{\theta}_{rr} &= -\frac{\partial_\theta g_{rr}}{2g_{\theta\theta}}, \quad \Gamma^{\theta}_{\theta\theta} = \frac{\partial_\theta g_{\theta\theta}}{2g_{\theta\theta}}, \quad \Gamma^{\theta}_{r\theta} = \frac{\partial_r g_{\theta\theta}}{2g_{\theta\theta}}. \end{aligned} \tag{A.21}$$

In order to set the particle movement at the equator, we choose the initial condition

$$\theta = \pi/2, \quad \dot{\theta} = 0, \tag{A.22}$$

which eliminates the terms $\Gamma^{\theta}_{\theta\theta}$ and $\Gamma^{\theta}_{r\theta}$. The remaining connection terms are precisely given by the components of the extrinsic curvature tensor k_{ab}. Therefore, the analysis is identical as the one made before, as expected from the equivalence of the definitions. We could also have written the extrinsic curvature with the equivalent formula [218]

$$k_{ab} = -n_\mu \left(\frac{\partial^2 x^\mu}{\partial x^a \partial x^b} + \Gamma^{\mu}_{\alpha\beta} \frac{\partial x^\alpha}{\partial x^a} \frac{\partial x^\beta}{\partial x^b} \right) = -\sqrt{g_{\theta\theta}}\Gamma^{\theta}_{ab}, \tag{A.23}$$

which is in accordance with Eqs. (A.17) and (A.21).

We conclude that, for odd $\mathbb{Z}_2$ symmetric spacetimes, it is possible for geodesics initially confined to the plane $\theta = \pi/2$, to deviate from it, namely

$$g_{\theta\theta}\ddot{\theta} = \dot{t}\dot{\varphi}\partial_\theta g_{t\varphi}. \tag{A.24}$$

In the literature, the existence of a well defined equator is associated only with spacetimes which are even $\mathbb{Z}_2$ symmetric. Expanding on this notion and from the results obtained in Eq. (A.18), one might think that the existence of a well defined equator is linked to a totally geodesic submanifold, which is not true. Our demonstration revealed that odd $\mathbb{Z}_2$ symmetric spacetimes provide a counter example, since they can also have a well defined equatorial plane, while also having geodesics escaping from it.

To illustrate how the geodesics deviate from the equatorial plane, we considered a plot of 50 geodesics in the SBHSU spacetime, with initial conditions given by Eqs. (4.32)-(4.35), $\theta = \pi/2$ and $r = 10M$. We fix $\alpha = 0$, which corresponds to geodesics launched at the equatorial plane ($p_\theta = 0$), and let β take values randomly. The plots are displayed in Fig. A.1 for $jM^2 = 0.001,\ 0.0025,\ 0.01$.

For the SBHSU, there exists a critical value for j, namely $j_{\rm c} = r^{-2}$, with r being the observer radial position, such that $|\partial_\theta g_{t\varphi}|$ is maximum. Therefore, the deviation of the geodesics is amplified for $j = j_{\rm c}$. For $r = 10M$, we have $j_{\rm c}M^2 = 0.01$, which corresponds to the bottom plot in Fig. A.1. For $j > j_{\rm c}$, the geodesic deviation from the equator starts to diminish. For $j \to \infty$, we have $\partial_\theta g_{t\varphi} \to 0$, so that, for high enough values of j, this effect disappears.

Concluding thoughts

In this thesis, we have explored various properties associated with BHs. The study was focused on QNMs and null geodesic calculations. To conclude, this final section highlights promising future directions for each study and discusses open questions that remain unanswered.

In Chapter 2, we explored the QNMs of a regular BH model with effective corrections from LQG. In recent years, there has been growing interest in regular BHs, though early attempts initially received little attention. The first regular BH was introduced by James Bardeen [219], which was later shown to be motivated by nonlinear Electrodynamics (NED) [220]. Several other solutions in NED-based models have also been reported (e.g., see Refs. [221–224]).

Effective LQG corrections have been successfully applied to cosmological models, as well as spherically symmetric BHs, where their singularities are replaced by bounces. More recently, the construction developed in Refs. [137, 138] has been extended to charged BHs, where a particularly interesting feature was reported: the Cauchy horizon lies inside the transition surface [225], making these models more physically appealing compared to other regular BH solutions found in NED. It has been shown that charged scalar fields in certain NED models can exhibit superradiant instability [226, 227], in contrast to the standard RN case [228, 229]. An intriguing avenue for further exploration would be to investigate whether effective quantum effects arising from LQG could also induce a similar instability.

In Chapter 3, we examined the behavior of null geodesics in the SBHSU. One may compare the number of LRs in the SBHSU spacetime with those in the Schwarzschild-Melvin

solution. When we non-linearly bring together the Schwarzschild BH ($w = -1$) and the SU ($w = 0$), the result is a spacetime with $w = -1$. On the other hand, both Schwarzschild and Melvin spacetimes admit the existence of LRs[3]. When these two spaces are non-linearly superposed in the Schwarzschild-Melvin solution, if the magnetic field is weak, there are two LRs on the spacetime, which were inhered by each one of the separate spacetimes. If we let the magnetic field become strong, the potential's critical points are spoiled [107]. By these two examples, heuristically, it seems that the number of LRs, as well as their respective stabilities, of each spacetime is preserved even after the non-linear superposition, as long as the boundary conditions are not significantly altered. Another example where this summation rule can fail due to boundary conditions is in the Schwarzschild-dilatonic-Melvin BH [108]. But, of course, it is hard to formalize this argument, since GR's field equations are non-linear and, therefore, the associated space of solutions does not constitute a vector space.

We remark that when delving into the study of exact solutions, one typically encounters scenarios where the spacetime is either overly idealized, making it inadequate for describing real physical systems, or it exhibits pathologies that render its existence in the natural world highly unlikely. During the GR7 international conference in 1974, Kinnersley highlighted this issue: *"the study of exact solutions has acquired a rather low reputation in the past, for which there are several explanations. Most of known exact solutions describe situations which are frankly unphysical and these do have a tendency to distract attention from useful ones"* [230].

The SBHSU spacetime, even though it is free of conical singularities and closed timelike curves, does not have much astrophysical appeal, since it is not asymptotically flat. However, there is also a case to be made if the SBHSU can represent, in some regime of approximation, an analytical model for some astrophysical phenomenon. The authors in Ref. [160] conjectured that the SBHSU might be useful to describe the collision of oppositely rotating galaxies. This issue holds the potential for a standalone work if thoroughly explored.

Apart from the phenomenology perspective, there exists a significant value in exploring

[3]For the Melvin universe, due to the translational invariance along the z direction, there exists a light tube instead of a LR.

exact solutions for understanding GR in its fully non-linear regime. Perhaps the most intriguing property of this solution is its north-south asymmetry, which we refer to as an odd $\mathbb{Z}_2$ symmetry (as defined in Appendix A). This asymmetry arises from opposite spinning directions above and below the equator and is closely linked to the off-equatorial LRs and the formation of a twisted shadow—the main results of this chapter. To our knowledge, no other BH solution with a connected horizon produces a shadow with odd symmetry. While not necessarily a fundamental requirement, such features are typically encountered in BBH systems (see Chapter 4).

Since the SBHSU is not asymptotically flat, it cannot be interpreted as a localized gravitating source. The authors of Ref. [160] conjectured that a double-Taub–NUT spacetime with opposite NUT parameters could generate a SU structure when pushed to infinity, which aligns well with the non-asymptotically flat nature of SU.

This immediately raises an interesting question: Is it possible to construct asymptotically flat BH solutions in GR that feature a connected horizon and odd symmetry? Additionally, under what conditions is this odd symmetry imprinted onto the shadow's edge? Breaking the even $\mathbb{Z}_2$ spacetime symmetry alone does not grantee that the same happens with its shadow [215, 231, 232]. It is possible that in Liouville-integrable, shadows tend to retain the even symmetry. Thus, under this hypothesis, the SBHSU solution may only be able to induce this particular spacetime symmetry in its shadow due to its non integrability condition. However, to our knowledge, there is no formal proof establishing a connection between the $\mathbb{Z}_2$ symmetry of spacetime and the corresponding shadow symmetry.

In Chap. 4 we focused on the study of null geodesics over the TW spacetime. We remark that the TW spacetime reported in Ref. [198] chooses the BHs to have equal electric and magnetic charges, which corresponds to the black line displayed in Fig. 4.1, but this is not mandatory. We chose to exhibit the extremal surface of the RL BH to show how much more can be explored. All our analyses are valid just for this black line segment in Fig. 4.1. It is an interesting task to generalize the TW spacetime, and the analysis in this chapter, for arbitrary charge values abiding the extremality constraint.

It has been reported that a quasi-static approach to simulate images for stationary BBHs can serve as a good approximation for a fully dynamical binary system [210]. Although this

method was successfully applied to the double-Schwarzschild case, no implementation for the double-Kerr configuration has been made, due to the complexity of the metric. Given that the TW spacetime exhibits a similar shadow pattern to the double-Kerr but has a simpler metric, it is more likely that the quasi-static method can be effectively applied to this case, offering a useful approximation for the images of a fully dynamical Kerr binary.

We discussed the absence of a rotating generalization of MP in EM. However, we identify a potential approach to constructing such a solution that, to our knowledge, has not yet been explored in the literature. By employing the Ernst formalism (see Subsection 3.2.1), one can generate a non-asymptotically flat magnetized version of RN, known as RN-Melvin, where the interaction between the BH charge and the surrounding magnetic field induces rotation in the spacetime. In principle, the same procedure could be applied to the MP solution, yielding a spinning generalization of MP within pure EM due to the presence of an external magnetic field. However, the main limitation of this approach is its non-asymptotic flatness, which may be an unavoidable feature in pure EM.

Bibliography

[1] M.J. Greenberg. *Euclidean and Non-Euclidean Geometries: Development and History.* W. H. Freeman, 1993.

[2] R.O. Wells. *Differential and Complex Geometry: Origins, Abstractions and Embeddings.* Springer International Publishing, 2017.

[3] Isaac Newton. *The Method of Fluxions and Infinite Series.* Henry Woodfall, London, 1736. Translated by John Colson from Newton's unpublished Latin manuscript (*Methodus Fluxionum et Serierum Infinitarum*, 1671). Download available at `http://www.archive.org/details/methodoffluxions00newt`.

[4] M.P. do Carmo. *Geometria diferencial de curvas e superfícies.* Textos Universitarios: Ciencias médicas. Sociedade Brasileira de Matemática, 2010.

[5] Carl Friedrich Gauss. *General Investigations of Curved Surfaces.* Dover Publications, Mineola, NY, 2005. Edited with an introduction and notes by Peter Pesic.

[6] Bernhard Riemann. *On the Hypotheses Which Lie at the Bases of Geometry.* Classic Texts in the Sciences. Birkhäuser Basel, 2016.

[7] M. Spivak. *A Comprehensive Introduction to Differential Geometry.* Number v. 2 in A Comprehensive Introduction to Differential Geometry. Publish or Perish, Incorporated, 1979.

[8] Albert Einstein. *"Geometry and Experience"*. Crown Publishers, New York, 1933. In Ideas and Opinions, pp. 232–246, Based on *Mein Weltbild*, edited by Carl Seelig and translated by Sonja Bargmann.

[9] Isaac Newton. *Principia, Vol. 1: The Motion of Bodies*. University of California Press, 1966. Translated by Andrew Motte with revisions by Florian Cajori.

[10] D.B. Malament. *Topics in the Foundations of General Relativity and Newtonian Gravitation Theory*. Chicago Lectures in Physics. University of Chicago Press, 2012.

[11] Henri Poincaré. On the dynamics of the electron, 1906. Translated from French and hosted on Wikisource. Original publication: *Rendiconti del Circolo Matematico di Palermo* **21**, 129–176 (1906).

[12] Hendrik Antoon Lorentz. *Beschouwingen over de zwaartekracht*. 1900.

[13] Abraham Pais. *Subtle is the Lord: The Science and the Life of Albert Einstein: The Science and the Life of Albert Einstein*. Oxford University Press, USA, 1982.

[14] Albert Einstein. *"Notes on the Origin of the General Theory of Relativity"*. Crown Publishers, New York, 1933. In Ideas and Opinions, pp. 285–290, Based on *Mein Weltbild*, edited by Carl Seelig and translated by Sonja Bargmann.

[15] Charles W. Misner, K. S. Thorne, and J. A. Wheeler. *Gravitation*. W. H. Freeman, San Francisco, 1973.

[16] R. P. Feynman. *Feynman lectures on gravitation*. 1996.

[17] Robert H. Kraichnan. Special-Relativistic Derivation of Generally Covariant Gravitation Theory. *Phys. Rev.*, 98:1118–1122, 1955.

[18] Suraj N. Gupta. Gravitation and Electromagnetism. *Phys. Rev.*, 96:1683–1685, 1954.

[19] S. N. Gupta. Einstein's and other theories of gravitation. *Reviews of Modern Physics*, 29:337–350, 1957. Referenced in §§7.1, 18.1.

[20] Walter E. Thirring. An alternative approach to the theory of gravitation. *Annals Phys.*, 16:96–117, 1961.

[21] Stanley Deser. Selfinteraction and gauge invariance. *Gen. Rel. Grav.*, 1:9–18, 1970.

[22] Norbert Straumann. Reflections on gravity. 6 2000.

[23] Karl Schwarzschild. On the gravitational field of a mass point according to Einstein's theory. *Sitzungsber. Preuss. Akad. Wiss. Berlin (Math. Phys.)*, 1916:189–196, 1916.

[24] H. Reissner. Über die Eigengravitation des elektrischen Feldes nach der Einsteinschen Theorie. *Annalen Phys.*, 355(9):106–120, 1916.

[25] G. Nordström. On the Energy of the Gravitation field in Einstein's Theory. *Koninklijke Nederlandse Akademie van Wetenschappen Proceedings Series B Physical Sciences*, 20:1238–1245, January 1918.

[26] Roy P. Kerr. Gravitational field of a spinning mass as an example of algebraically special metrics. *Phys. Rev. Lett.*, 11:237–238, 1963.

[27] E. T. Newman and A. I. Janis. Note on the Kerr spinning particle metric. *J. Math. Phys.*, 6:915–917, 1965.

[28] E T. Newman, R. Couch, K. Chinnapared, A. Exton, A. Prakash, and R. Torrence. Metric of a Rotating, Charged Mass. *J. Math. Phys.*, 6:918–919, 1965.

[29] S. Gillessen, F. Eisenhauer, S. Trippe, T. Alexander, R. Genzel, F. Martins, and T. Ott. Monitoring stellar orbits around the Massive Black Hole in the Galactic Center. *Astrophys. J.*, 692:1075–1109, 2009.

[30] M. Kac. Can one hear the shape of a drum? *Am. Math. Mon.*, 73:1–23, 1966.

[31] Carolyn Gordon, David Webb, and Scott Wolpert. Isospectral plane domains and surfaces via riemannian orbifolds. *Inventiones mathematicae*, 110(1):1–22, 1992.

[32] Steve Zelditch. Spectral determination of analytic bi-axisymmetric plane domains. *Geometric & Functional Analysis GAFA*, 10(3):628–677, 2000.

[33] Steve Zelditch. Inverse resonance problem for $\mathbb{Z}_2$-symmetric analytic obstacles in the plane. In *Geometric methods in inverse problems and PDE control*, pages 289–321. Springer, 2004.

[34] Steve Zelditch. Inverse spectral problem for analytic domains i: Balian-bloch trace formula. *Communications in mathematical physics*, 248:357–407, 2004.

[35] Steve Zelditch. Inverse spectral problem for analytic domains, ii: $\mathbb{Z}_2$-symmetric domains. *Annals of mathematics*, pages 205–269, 2009.

[36] Tullio Regge and John A. Wheeler. Stability of a Schwarzschild singularity. *Phys. Rev.*, 108:1063–1069, 1957.

[37] Albert Einstein. Näherungsweise integration der feldgleichungen der gravitation. *Sitzungsberichte der Königlich Preußischen Akademie der Wissenschaften*, pages 688–696, 1916.

[38] Sean Carroll. Mindscape episode 24: Kip thorne on gravitational waves, time travel, and interstellar. Available at `https://www.youtube.com/watch?v=kAr-YR6Mq34&t=733s`.

[39] Frans Pretorius. Evolution of binary black hole spacetimes. *Phys. Rev. Lett.*, 95:121101, 2005.

[40] Manuela Campanelli, C. O. Lousto, P. Marronetti, and Y. Zlochower. Accurate evolutions of orbiting black-hole binaries without excision. *Phys. Rev. Lett.*, 96:111101, 2006.

[41] John G. Baker, Joan Centrella, Dae-Il Choi, Michael Koppitz, and James van Meter. Gravitational wave extraction from an inspiraling configuration of merging black holes. *Phys. Rev. Lett.*, 96:111102, 2006.

[42] F. Echeverria. Gravitational Wave Measurements of the Mass and Angular Momentum of a Black Hole. *Phys. Rev. D*, 40:3194–3203, 1989.

[43] Lee S. Finn. Detection, measurement and gravitational radiation. *Phys. Rev. D*, 46:5236–5249, 1992.

[44] Emanuele Berti, Vitor Cardoso, and Andrei O. Starinets. Quasinormal modes of black holes and black branes. *Class. Quant. Grav.*, 26:163001, 2009.

[45] Sebastian H. Völkel and Kostas D. Kokkotas. Scalar Fields and Parametrized Spherically Symmetric Black Holes: Can one hear the shape of space-time? *Phys. Rev. D*, 100(4):044026, 2019.

[46] B. P. Abbott et al. Observation of Gravitational Waves from a Binary Black Hole Merger. *Phys. Rev. Lett.*, 116(6):061102, 2016.

[47] R. Abbott et al. GWTC-3: Compact Binary Coalescences Observed by LIGO and Virgo during the Second Part of the Third Observing Run. *Phys. Rev. X*, 13(4):041039, 2023.

[48] A. G. Abac et al. Observation of Gravitational Waves from the Coalescence of a 2.5–4.5 M $_\odot$ Compact Object and a Neutron Star. *Astrophys. J. Lett.*, 970(2):L34, 2024.

[49] Kostas D. Kokkotas and Bernd G. Schmidt. Quasinormal modes of stars and black holes. *Living Rev. Rel.*, 2:2, 1999.

[50] N.A. Lemos. *Convite A Fisica Matematica*. LIVRARIA DA FISICA.

[51] Kenichi Konishi and Giampiero Paffuti. *Quantum mechanics: A new introduction*. Oxford Univ. Pr., Oxford, UK, 2009.

[52] Frank J. Zerilli. Effective potential for even parity Regge-Wheeler gravitational perturbation equations. *Phys. Rev. Lett.*, 24:737–738, 1970.

[53] F. J. Zerilli. Gravitational field of a particle falling in a schwarzschild geometry analyzed in tensor harmonics. *Phys. Rev. D*, 2:2141–2160, 1970.

[54] S. Chandrasekhar and Steven L. Detweiler. The quasi-normal modes of the Schwarzschild black hole. *Proc. Roy. Soc. Lond. A*, 344:441–452, 1975.

[55] E. W. Leaver. An Analytic representation for the quasi normal modes of Kerr black holes. *Proc. Roy. Soc. Lond. A*, 402:285–298, 1985.

[56] Mohamed Ould El Hadj and Sam R. Dolan. Conversion of electromagnetic and gravitational waves by a charged black hole. *Phys. Rev. D*, 106(4):044002, 2022.

[57] K. D. Kokkotas and Bernard F. Schutz. Black Hole Normal Modes: A WKB Approach. 3. The Reissner-Nordstrom Black Hole. *Phys. Rev. D*, 37:3378–3387, 1988.

[58] Edward W. Leaver. Quasinormal modes of Reissner-Nordstrom black holes. *Phys. Rev. D*, 41:2986–2997, 1990.

[59] Nils Andersson. Normal-mode frequencies of reissner–nordström black holes. *Proceedings of the Royal Society of London. Series A: Mathematical and Physical Sciences*, 442(1915):427–436, 1993.

[60] Hisashi Onozawa, Takashi Mishima, Takashi Okamura, and Hideki Ishihara. Quasinormal modes of maximally charged black holes. *Phys. Rev. D*, 53:7033–7040, 1996.

[61] Nils Andersson and Hisashi Onozawa. Quasinormal modes of nearly extreme Reissner-Nordstrom black holes. *Phys. Rev. D*, 54:7470–7475, 1996.

[62] Emanuele Berti and Kostas D. Kokkotas. Asymptotic quasinormal modes of Reissner-Nordstrom and Kerr black holes. *Phys. Rev. D*, 68:044027, 2003.

[63] Hisashi Onozawa. A Detailed study of quasinormal frequencies of the Kerr black hole. *Phys. Rev. D*, 55:3593–3602, 1997.

[64] Steven L. Detweiler. BLACK HOLES AND GRAVITATIONAL WAVES. III. THE RESONANT FREQUENCIES OF ROTATING HOLES. *Astrophys. J.*, 239:292–295, 1980.

[65] Ji-liang Jing and Qi-yuan Pan. Dirac quasinormal frequencies of the Kerr-Newman black hole. *Nucl. Phys. B*, 728:109–120, 2005.

[66] Emanuele Berti and Kostas D. Kokkotas. Quasinormal modes of Kerr-Newman black holes: Coupling of electromagnetic and gravitational perturbations. *Phys. Rev. D*, 71:124008, 2005.

[67] Jose Luis Blázquez-Salcedo and Fech Scen Khoo. Quasinormal modes of slowly rotating Kerr-Newman black holes using the double series method. *Phys. Rev. D*, 107(8):084031, 2023.

[68] L. Campbell and W. Garnett. *The Life of James Clerk Maxwell: With a Selection from His Correspondence and Occasional Writings and a Sketch of His Contributions to Science*. Macmillan, 1882.

[69] James Clerk Maxwell. Experiments on colour, as perceived by the eye, with remarks on colour-blindness. *Transactions of the Royal Society of Edinburgh*, 21:275–298, 1857.

[70] Wikimedia Commons. Tartan ribbon, photograph taken by james clerk maxwell in 1861. Available at `https://commons.wikimedia.org/wiki/File:Tartan_Ribbon.jpg`.

[71] B. Mahon. *The Man Who Changed Everything: The Life of James Clerk Maxwell*. Wiley, 2005.

[72] Heino Falcke, Fulvio Melia, and Eric Agol. Viewing the shadow of the black hole at the galactic center. *Astrophys. J. Lett.*, 528:L13, 2000.

[73] Kazunori Akiyama et al. First M87 Event Horizon Telescope Results. I. The Shadow of the Supermassive Black Hole. *Astrophys. J. Lett.*, 875:L1, 2019.

[74] Kazunori Akiyama et al. First Sagittarius A* Event Horizon Telescope Results. I. The Shadow of the Supermassive Black Hole in the Center of the Milky Way. *Astrophys. J. Lett.*, 930(2):L12, 2022.

[75] F. W. Dyson, A. S. Eddington, and C. Davidson. A Determination of the Deflection of Light by the Sun's Gravitational Field, from Observations Made at the Total Eclipse of May 29, 1919. *Phil. Trans. Roy. Soc. Lond. A*, 220:291–333, 1920.

[76] Luís C. B. Crispino and Daniel Kennefick. 100 years of the first experimental test of General Relativity. *Nature Phys.*, 15:416, 2019.

[77] Albert Einstein. Lens-Like Action of a Star by the Deviation of Light in the Gravitational Field. *Science*, 84:506–507, 1936.

[78] Mariusz P. Dabrowski and Franz E. Schunck. Boson stars as gravitational lenses. *Astrophys. J.*, 535:316–324, 2000.

[79] K. S. Virbhadra and George F. R. Ellis. Schwarzschild black hole lensing. *Phys. Rev. D*, 62:084003, 2000.

[80] Ernesto F. Eiroa, Gustavo E. Romero, and Diego F. Torres. Reissner-Nordstrom black hole lensing. *Phys. Rev. D*, 66:024010, 2002.

[81] Mourad Halla and Volker Perlick. Application of the Gauss–Bonnet theorem to lensing in the NUT metric. *Gen. Rel. Grav.*, 52(11):112, 2020. [Erratum: Gen.Rel.Grav. 53, 68 (2021)].

[82] Valerio Bozza. Gravitational Lensing by Black Holes. *Gen. Rel. Grav.*, 42:2269–2300, 2010.

[83] Pedro V. P. Cunha, José A. Font, Carlos Herdeiro, Eugen Radu, Nicolas Sanchis-Gual, and Miguel Zilhão. Lensing and dynamics of ultracompact bosonic stars. *Phys. Rev. D*, 96(10):104040, 2017.

[84] Hector Olivares, Ziri Younsi, Christian M. Fromm, Mariafelicia De Laurentis, Oliver Porth, Yosuke Mizuno, Heino Falcke, Michael Kramer, and Luciano Rezzolla. How to tell an accreting boson star from a black hole. *Mon. Not. Roy. Astron. Soc.*, 497(1):521–535, 2020.

[85] Abhishek Chowdhuri and Arpan Bhattacharyya. Shadow analysis for rotating black holes in the presence of plasma for an expanding universe. *Phys. Rev. D*, 104(6):064039, 2021.

[86] Carlos A. R. Herdeiro, Alexandre M. Pombo, Eugen Radu, Pedro V. P. Cunha, and Nicolas Sanchis-Gual. The imitation game: Proca stars that can mimic the Schwarzschild shadow. *JCAP*, 04:051, 2021.

[87] Misba Afrin, Sunny Vagnozzi, and Sushant G. Ghosh. Tests of Loop Quantum Gravity from the Event Horizon Telescope Results of Sgr A*. *Astrophys. J.*, 944(2):149, 2023.

[88] Javier Badía and Ernesto F. Eiroa. Shadows of rotating Einstein-Maxwell-dilaton black holes surrounded by a plasma. *Phys. Rev. D*, 107(12):124028, 2023.

[89] Sunny Vagnozzi et al. Horizon-scale tests of gravity theories and fundamental physics from the Event Horizon Telescope image of Sagittarius A. *Class. Quant. Grav.*, 40(16):165007, 2023.

[90] João Luís Rosa and Diego Rubiera-Garcia. Shadows of boson and Proca stars with thin accretion disks. *Phys. Rev. D*, 106(8):084004, 2022.

[91] Songbai Chen, Jiliang Jing, Wei-Liang Qian, and Bin Wang. Black hole images: A review. *Sci. China Phys. Mech. Astron.*, 66(6):260401, 2023.

[92] João Luís Rosa, Caio F. B. Macedo, and Diego Rubiera-Garcia. Imaging compact boson stars with hot spots and thin accretion disks. *Phys. Rev. D*, 108(4):044021, 2023.

[93] Xiao-Jun Gao, Tao-Tao Sui, Xiao-Xiong Zeng, Yu-Sen An, and Ya-Peng Hu. Investigating shadow images and rings of the charged Horndeski black hole illuminated by various thin accretions. *Eur. Phys. J. C*, 83:1052, 2023.

[94] Mingzhi Wang, Guanghai Guo, Pengfei Yan, Songbai Chen, and Jiliang Jing. The ring shadow of rotating naked singularity with a complete photon sphere. 7 2023.

[95] Marco A. A. de Paula, Haroldo C. D. Lima Junior, Pedro V. P. Cunha, and Luís C. B. Crispino. Electrically charged regular black holes in nonlinear electrodynamics: Light rings, shadows, and gravitational lensing. *Phys. Rev. D*, 108(8):084029, 2023.

[96] Shangyu Wen, Wei Hong, and Jun Tao. Observational Appearances of Magnetically Charged Black Holes in Born-Infeld Electrodynamics. *Eur. Phys. J. C*, 83:277, 2023.

[97] Farruh Atamurotov, Ibrar Hussain, G. Mustafa, and Kimet Jusufi. Shadow and quasinormal modes of the Kerr–Newman–Kiselev–Letelier black hole. *Eur. Phys. J. C*, 82(9):831, 2022.

[98] Yehui Hou, Zhenyu Zhang, Haopeng Yan, Minyong Guo, and Bin Chen. Image of a Kerr-Melvin black hole with a thin accretion disk. *Phys. Rev. D*, 106(6):064058, 2022.

[99] Merce Guerrero, Gonzalo J. Olmo, Diego Rubiera-Garcia, and Diego Sáez-Chillón Gómez. Multiring images of thin accretion disk of a regular naked compact object. *Phys. Rev. D*, 106(4):044070, 2022.

[100] Xiao-Mei Kuang and Ali Övgün. Strong gravitational lensing and shadow constraint from M87* of slowly rotating Kerr-like black hole. *Annals Phys.*, 447:169147, 2022.

[101] Barbora Bezdekova, Volker Perlick, and Jiri Bicak. Light propagation in a plasma on an axially symmetric and stationary spacetime: Separability of the Hamilton–Jacobi equation and shadow. *J. Math. Phys.*, 63(9):092501, 2022.

[102] A. Belhaj, M. Benali, and Y. Hassouni. Superentropic black hole shadows in arbitrary dimensions. *Eur. Phys. J. C*, 82(7):619, 2022.

[103] Hui-Min Wang and Shao-Wen Wei. Shadow cast by Kerr-like black hole in the presence of plasma in Einstein-bumblebee gravity. *Eur. Phys. J. Plus*, 137(5):571, 2022.

[104] Pedro V. P. Cunha, Emanuele Berti, and Carlos A. R. Herdeiro. Light-Ring Stability for Ultracompact Objects. *Phys. Rev. Lett.*, 119(25):251102, 2017.

[105] Pedro V. P. Cunha and Carlos A. R. Herdeiro. Stationary black holes and light rings. *Phys. Rev. Lett.*, 124(18):181101, 2020.

[106] Shao-Wen Wei. Topological Charge and Black Hole Photon Spheres. *Phys. Rev. D*, 102(6):064039, 2020.

[107] Haroldo C. D. Lima Junior, Pedro V. P. Cunha, Carlos A. R. Herdeiro, and Luís C. B. Crispino. Shadows and lensing of black holes immersed in strong magnetic fields. *Phys. Rev. D*, 104(4):044018, 2021.

[108] Haroldo C. D. Lima Junior, Jian-Zhi Yang, Luís C. B. Crispino, Pedro V. P. Cunha, and Carlos A. R. Herdeiro. Einstein-Maxwell-dilaton neutral black holes in strong magnetic fields: Topological charge, shadows, and lensing. *Phys. Rev. D*, 105(6):064070, 2022.

[109] Shan-Ping Wu and Shao-Wen Wei. Topology of light rings for extremal and nonextremal Kerr-Newman-Taub-NUT black holes without Z2 symmetry. *Phys. Rev. D*, 108(10):104041, 2023.

[110] Pedro V. P. Cunha, Carlos A. R. Herdeiro, and Eugen Radu. Fundamental photon orbits: black hole shadows and spacetime instabilities. *Phys. Rev. D*, 96(2):024039, 2017.

[111] J. L. Synge. The Escape of Photons from Gravitationally Intense Stars. *Mon. Not. Roy. Astron. Soc.*, 131(3):463–466, 1966.

[112] J. M. Bardeen. Timelike and null geodesics in the Kerr metric. *Proceedings, Ecole d'Eté de Physique Théorique: Les Astres Occlus : Les Houches, France, August, 1972, 215-240*, pages 215–240, 1973.

[113] Haroldo C. D. Lima, Junior., Luís C. B. Crispino, Pedro V. P. Cunha, and Carlos A. R. Herdeiro. Can different black holes cast the same shadow? *Phys. Rev. D*, 103(8):084040, 2021.

[114] Brandon Carter. Global structure of the Kerr family of gravitational fields. *Phys. Rev.*, 174:1559–1571, 1968.

[115] Pedro Vieira Pinto da Cunha. Black hole shadows-sombras de buracos negros. Master's thesis, Universidade de Coimbra (Portugal), 2015.

[116] P. V. P. Cunha, J. Grover, C. Herdeiro, E. Radu, H. Runarsson, and A. Wittig. Chaotic lensing around boson stars and Kerr black holes with scalar hair. *Phys. Rev. D*, 94(10):104023, 2016.

[117] Ivo Sengo, Pedro V. P. Cunha, Carlos A. R. Herdeiro, and Eugen Radu. Kerr black holes with synchronised Proca hair: lensing, shadows and EHT constraints. *JCAP*, 01:047, 2023.

[118] R. d'Inverno. *Introducing Einstein's relativity*. 1992.

[119] Clifford M. Will. The Confrontation between General Relativity and Experiment. *Living Rev. Rel.*, 17:4, 2014.

[120] S. W. Hawking and R. Penrose. The Singularities of gravitational collapse and cosmology. *Proc. Roy. Soc. Lond. A*, 314:529–548, 1970.

[121] Roger Penrose. Gravitational collapse and space-time singularities. *Phys. Rev. Lett.*, 14:57–59, 1965.

[122] Bryce S. DeWitt. Quantum Theory of Gravity. 1. The Canonical Theory. *Phys. Rev.*, 160:1113–1148, 1967.

[123] Thomas Thiemann. Introduction to modern canonical quantum general relativity. *arXiv preprint gr-qc/0110034*, 2001.

[124] Amitabha Sen. Gravity as a spin system. *Phys. Lett., B*, 119(1-3):89–91, 1982.

[125] A. Ashtekar. New Variables for Classical and Quantum Gravity. *Phys. Rev. Lett.*, 57:2244–2247, 1986.

[126] J. Fernando Barbero G. Real Ashtekar variables for Lorentzian signature space times. *Phys. Rev. D*, 51:5507–5510, 1995.

[127] Kenneth G. Wilson. Confinement of Quarks. *Phys. Rev. D*, 10:2445–2459, 1974.

[128] Martin Bojowald. Absence of singularity in loop quantum cosmology. *Phys. Rev. Lett.*, 86:5227–5230, 2001.

[129] Rodolfo Gambini and Jorge Pullin. Loop quantization of the Schwarzschild black hole. *Phys. Rev. Lett.*, 110(21):211301, 2013.

[130] A. Ashtekar, J. Baez, A. Corichi, and Kirill Krasnov. Quantum geometry and black hole entropy. *Phys. Rev. Lett.*, 80:904–907, 1998.

[131] Martin Bojowald. Loop quantum cosmology. *Living Rev. Rel.*, 8:11, 2005.

[132] Abhay Ashtekar, Tomasz Pawlowski, and Parampreet Singh. Quantum Nature of the Big Bang: Improved dynamics. *Phys. Rev. D*, 74:084003, 2006.

[133] Babak Vakili. Classical polymerization of the Schwarzschild metric. *Adv. High Energy Phys.*, 2018:3610543, 2018.

[134] Norbert Bodendorfer, Fabio M. Mele, and Johannes Münch. Effective Quantum Extended Spacetime of Polymer Schwarzschild Black Hole. *Class. Quant. Grav.*, 36(19):195015, 2019.

[135] Jibril Ben Achour, Frédéric Lamy, Hongguang Liu, and Karim Noui. Polymer Schwarzschild black hole: An effective metric. *EPL*, 123(2):20006, 2018.

[136] Rakesh Tibrewala. Spherically symmetric Einstein-Maxwell theory and loop quantum gravity corrections. *Class. Quant. Grav.*, 29:235012, 2012.

[137] Asier Alonso-Bardaji, David Brizuela, and Raül Vera. An effective model for the quantum Schwarzschild black hole. *Phys. Lett. B*, 829:137075, 2022.

[138] Asier Alonso-Bardaji, David Brizuela, and Raül Vera. Nonsingular spherically symmetric black-hole model with holonomy corrections. *Phys. Rev. D*, 106(2):024035, 2022.

[139] Charles W. Misner. Gravitational Field Energy and g00. *Phys. Rev.*, 130:1590–1594, 1963.

[140] Sean A. Hayward. Gravitational energy in spherical symmetry. *Phys. Rev. D*, 53:1938–1949, 1996.

[141] Alex Simpson and Matt Visser. Black-bounce to traversable wormhole. *JCAP*, 02:042, 2019.

[142] K. A. Bronnikov. Black bounces, wormholes, and partly phantom scalar fields. *Phys. Rev. D*, 106(6):064029, 2022.

[143] M. S. Churilova and Z. Stuchlik. Ringing of the regular black-hole/wormhole transition. *Class. Quant. Grav.*, 37(7):075014, 2020.

[144] Kirill A. Bronnikov and Roman A. Konoplya. Echoes in brane worlds: ringing at a black hole–wormhole transition. *Phys. Rev. D*, 101(6):064004, 2020.

[145] Yi Yang, Dong Liu, Zhaoyi Xu, Yujia Xing, Shurui Wu, and Zheng-Wen Long. Echoes of novel black-bounce spacetimes. *Phys. Rev. D*, 104(10):104021, 2021.

[146] Bernard F. Schutz and Clifford M. Will. BLACK HOLE NORMAL MODES: A SEMI-ANALYTIC APPROACH. *Astrophys. J. Lett.*, 291:L33–L36, 1985.

[147] Sai Iyer and Clifford M. Will. Black Hole Normal Modes: A WKB Approach. 1. Foundations and Application of a Higher Order WKB Analysis of Potential Barrier Scattering. *Phys. Rev. D*, 35:3621, 1987.

[148] O. B. Zaslavsky. Black hole normal modes and quantum anharmonic oscillator. *Phys. Rev. D*, 43:605–608, 1991.

[149] S.I.U. Slavianov and W. Lay. *Special Functions: A Unified Theory Based on Singularities*. Oxford Science Publications. Oxford University Press, 2000.

[150] Hans-Peter Nollert. Quasinormal modes of Schwarzschild black holes: The determination of quasinormal frequencies with very large imaginary parts. *Phys. Rev. D*, 47:5253–5258, 1993.

[151] Emanuele Berti, Vitor Cardoso, Jose A. Gonzalez, and Ulrich Sperhake. Mining information from binary black hole mergers: A Comparison of estimation methods for complex exponentials in noise. *Phys. Rev. D*, 75:124017, 2007.

[152] Subrahmanyan Chandrasekhar. On algebraically special perturbations of black holes. *Proceedings of the Royal Society of London. A. Mathematical and Physical Sciences*, 392(1802):1–13, 1984.

[153] Lubos Motl. An Analytical computation of asymptotic Schwarzschild quasinormal frequencies. *Adv. Theor. Math. Phys.*, 6:1135–1162, 2003.

[154] Carlos A. R. Herdeiro. Black Holes: On the Universality of the Kerr Hypothesis. *Lect. Notes Phys.*, 1017:315–331, 2023.

[155] Kurt Godel. An Example of a New Type of Cosmological Solutions of Einstein's Field Equations of Gravitation. *Rev. Mod. Phys.*, 21:447–450, 1949.

[156] Stephen W. Hawking and George F. R. Ellis. *The Large Scale Structure of Space-Time*. Cambridge Monographs on Mathematical Physics. Cambridge University Press, 2 2023.

[157] A. H. Taub. Empty space-times admitting a three parameter group of motions. *Annals Math.*, 53:472–490, 1951.

[158] E. Newman, L. Tamburino, and T. Unti. Empty space generalization of the Schwarzschild metric. *J. Math. Phys.*, 4:915, 1963.

[159] Hans Stephani, D. Kramer, Malcolm A. H. MacCallum, Cornelius Hoenselaers, and Eduard Herlt. *Exact solutions of Einstein's field equations*. Cambridge Monographs on Mathematical Physics. Cambridge Univ. Press, Cambridge, 2003.

[160] Marco Astorino, Riccardo Martelli, and Adriano Viganò. Black holes in a swirling universe. *Phys. Rev. D*, 106(6):064014, 2022.

[161] G. W. Gibbons, A. H. Mujtaba, and C. N. Pope. Ergoregions in Magnetised Black Hole Spacetimes. *Class. Quant. Grav.*, 30(12):125008, 2013.

[162] José Barrientos, Adolfo Cisterna, Ivan Kolář, Keanu Müller, Marcelo Oyarzo, and Konstantinos Pallikaris. Mixing Magnetic and Electric Ehlers-Harrison transformations: The Electromagnetic Swirling Spacetime and Novel Type I Backgrounds. 1 2024.

[163] Marco Astorino. Removal of conical singularities from rotating C-metrics and dual CFT entropy. *JHEP*, 10:074, 2022.

[164] Matilde Illy. Accelerated Reissner-Nordstrom black hole in a swirling, magnetic universe. Other thesis, 12 2023.

[165] Pedro V. P. Cunha, Carlos A. R. Herdeiro, and João P. A. Novo. LRs on stationary axisymmetric spacetimes: blind to the topology and able to coexist. 1 2024.

[166] Rajes Ghosh and Sudipta Sarkar. Light rings of stationary spacetimes. *Phys. Rev. D*, 104(4):044019, 2021.

[167] Frederick J. Ernst. New formulation of the axially symmetric gravitational field problem. *Phys. Rev.*, 167:1175–1179, 1968.

[168] Frederick J. Ernst. New Formulation of the Axially Symmetric Gravitational Field Problem. II. *Phys. Rev.*, 168:1415–1417, 1968.

[169] Marco Astorino. Embedding hairy black holes in a magnetic universe. *Phys. Rev. D*, 87(8):084029, 2013.

[170] Robert P. Geroch. A Method for generating solutions of Einstein's equations. *J. Math. Phys.*, 12:918–924, 1971.

[171] W. Kinnersley. Generation of stationary Einstein-Maxwell fields. *J. Math. Phys.*, 14(5):651–653, 1973.

[172] W. Kinnersley. Symmetries of the Stationary Einstein-Maxwell Field Equations. 1. *J. Math. Phys.*, 18:1529–1537, 1977.

[173] Brandon Carter. The commutation property of a stationary, axisymmetric system. *Commun. Math. Phys.*, 17:233–238, 1970.

[174] E. S. Costa Filho. Construction of new solutions of the electro-vacuum einstein equation. Master's thesis, Instituto de Física de São Carlos, University of São Paulo, São Carlos, 2020.

[175] Adriano Viganò. *Black Holes and Solution Generating Techniques*. PhD thesis, Milan U., 2022.

[176] Subrahmanyan Chandrasekhar. *The mathematical theory of black holes*. 1985.

[177] Arthur Komar. Positive-Definite Energy Density and Global Consequences for General Relativity. *Phys. Rev.*, 129(4):1873, 1963.

[178] J.M. Lee. *Introduction to Smooth Manifolds*. Graduate Texts in Mathematics. Springer, 2003.

[179] Rogério Capobianco, Betti Hartmann, and Jutta Kunz. Geodesic Motion in a Swirling Universe: The complete set of solutions. 12 2023.

[180] Manfredo P. Carmo. *Geometria diferencial de curvas e superfícies*. 2005.

[181] Valeri P. Frolov. Embedding of the Kerr-Newman black hole surface in Euclidean space. *Phys. Rev. D*, 73:064021, 2006.

[182] Volker Perlick and Oleg Yu. Tsupko. Light propagation in a plasma on Kerr spacetime. II. Plasma imprint on photon orbits. 11 2023.

[183] Gary L Bunting and Abdul Kasem Muhammad Masood-ul Alam. Nonexistence of multiple black holes in asymptotically euclidean static vacuum space-time. *General relativity and gravitation*, 19:147–154, 1987.

[184] Miguel S. Costa, Carlos A. R. Herdeiro, and Carmen Rebelo. Dynamical and Thermodynamical Aspects of Interacting Kerr Black Holes. *Phys. Rev. D*, 79:123508, 2009.

[185] Gernot Neugebauer and Jorg Hennig. Stationary two-black-hole configurations: A non-existence proof. *J. Geom. Phys.*, 62:613–630, 2012.

[186] Jorg Hennig and Gernot Neugebauer. Non-existence of stationary two-black-hole configurations: The degenerate case. *Gen. Rel. Grav.*, 43:3139–3162, 2011.

[187] Rudolf Bach and H Wevl. Neue lösungen der einsteinschen gravitationsgleichungen: B. explizite aufstellung statischer axialsymmetrischer felder. *Mathematische Zeitschrift*, 13(1):134–145, 1922.

[188] D Kramer and G Neugebauer. The superposition of two kerr solutions. *Physics Letters A*, 75(4):259–261, 1980.

[189] Carlos A. R. Herdeiro and Eugen Radu. Two Schwarzschild-like black holes balanced by their scalar hair. *Phys. Rev. D*, 107(6):064044, 2023.

[190] Carlos A. R. Herdeiro and Eugen Radu. Two Spinning Black Holes Balanced by Their Synchronized Scalar Hair. *Phys. Rev. Lett.*, 131(12):121401, 2023.

[191] Marco Astorino and Adriano Vigano. Binary black hole system at equilibrium. *Phys. Lett. B*, 820:136506, 2021.

[192] Oscar J. C. Dias, Gary W. Gibbons, Jorge E. Santos, and Benson Way. Static Black Binaries in de Sitter Space. *Phys. Rev. Lett.*, 131(13):131401, 2023.

[193] S. D. Majumdar. A class of exact solutions of Einstein's field equations. *Phys. Rev.*, 72:390–398, 1947.

[194] A. Papaetrou. A Static solution of the equations of the gravitational field for an arbitrary charge distribution. *Proc. Roy. Irish Acad. A*, 51:191–204, 1947.

[195] W. Israel and G. A. Wilson. A class of stationary electromagnetic vacuum fields. *J. Math. Phys.*, 13:865–871, 1972.

[196] Zoltan Perjes. Solutions of the coupled Einstein Maxwell equations representing the fields of spinning sources. *Phys. Rev. Lett.*, 27:1668, 1971.

[197] J. B. Hartle and S. W. Hawking. Solutions of the Einstein-Maxwell equations with many black holes. *Commun. Math. Phys.*, 26:87–101, 1972.

[198] Edward Teo and Thomas Wan. Multicentered rotating black holes in Kaluza-Klein theory. *Phys. Rev. D*, 109(4):044054, 2024.

[199] Dean Rasheed. The Rotating dyonic black holes of Kaluza-Klein theory. *Nucl. Phys. B*, 454:379–401, 1995.

[200] Finn Larsen. Rotating Kaluza-Klein black holes. *Nucl. Phys. B*, 575:211–230, 2000.

[201] Marcel Berger. *A panoramic view of Riemannian geometry.* Springer, 2003.

[202] Jorge F. M. Delgado, Carlos A. R. Herdeiro, and Eugen Radu. Violations of the Kerr and Reissner-Nordström bounds: Horizon versus asymptotic quantities. *Phys. Rev. D*, 94(2):024006, 2016.

[203] G. W. Gibbons and C. A. R. Herdeiro. Supersymmetric rotating black holes and causality violation. *Class. Quant. Grav.*, 16:3619–3652, 1999.

[204] G. Clement. Rotating Kaluza-Klein Monopoles and Dyons. *Phys. Lett. A*, 118:11–13, 1986.

[205] Seyedhabibollah Mazharimousavi and Mustafa Halilsoy. Revisiting the dyonic Majumdar-Papapetrou black holes. *Turk. J. Phys.*, 40(2):163–174, 2016.

[206] Sérgio V. M. C. B. Xavier, Carlos A. R. Herdeiro, and Luís C. B. Crispino. Traversable wormholes and light rings. *Phys. Rev. D*, 109(12):124065, 2024.

[207] Jake Shipley and Sam R Dolan. Binary black hole shadows, chaotic scattering and the Cantor set. *Class. Quant. Grav.*, 33(17):175001, 2016.

[208] Zeus S. Moreira, Carlos A. R. Herdeiro, and Luís C. B. Crispino. Twisting shadows: Light rings, lensing, and shadows of black holes in swirling universes. *Phys. Rev. D*, 109(10):104020, 2024.

[209] Pedro V. P. Cunha, Carlos A. R. Herdeiro, and Maria J. Rodriguez. Does the black hole shadow probe the event horizon geometry? *Phys. Rev. D*, 97(8):084020, 2018.

[210] Pedro V. P. Cunha, Carlos A. R. Herdeiro, and Maria J. Rodriguez. Shadows of Exact Binary Black Holes. *Phys. Rev. D*, 98(4):044053, 2018.

[211] Akifumi Yumoto, Daisuke Nitta, Takeshi Chiba, and Naoshi Sugiyama. Shadows of Multi-Black Holes: Analytic Exploration. *Phys. Rev. D*, 86:103001, 2012.

[212] Daisuke Nitta, Takeshi Chiba, and Naoshi Sugiyama. Shadows of Colliding Black Holes. *Phys. Rev. D*, 84:063008, 2011.

[213] N.W. Johnson. *Geometries and Transformations*. Cambridge University Press, 2018.

[214] Pedro V. P. Cunha, Carlos A. R. Herdeiro, and Eugen Radu. Spontaneously Scalarized Kerr Black Holes in Extended Scalar-Tensor–Gauss-Bonnet Gravity. *Phys. Rev. Lett.*, 123(1):011101, 2019.

[215] Che-Yu Chen. Rotating black holes without $\mathbb{Z}_2$ symmetry and their shadow images. *JCAP*, 05:040, 2020.

[216] Sean M. Carroll. *Spacetime and Geometry: An Introduction to General Relativity*. Cambridge University Press, 7 2019.

[217] Barrett O'neill. *Semi-Riemannian geometry with applications to relativity*. Academic press, 1983.

[218] Farook Rahaman. *The General Theory of Relativity: A Mathematical Approach*. Cambridge University Press, 2021.

[219] J. Bardeen. Non-singular general relativistic gravitational collapse. In *Proceedings of the International Conference GR5*, page 174, Tbilisi, Georgia, U.S.S.R., 1968.

[220] Eloy Ayon-Beato and Alberto Garcia. The Bardeen model as a nonlinear magnetic monopole. *Phys. Lett. B*, 493:149–152, 2000.

[221] Eloy Ayon-Beato and Alberto Garcia. Regular black hole in general relativity coupled to nonlinear electrodynamics. *Phys. Rev. Lett.*, 80:5056–5059, 1998.

[222] Kirill A. Bronnikov. Regular magnetic black holes and monopoles from nonlinear electrodynamics. *Phys. Rev. D*, 63:044005, 2001.

[223] Irina Dymnikova. Regular electrically charged structures in nonlinear electrodynamics coupled to general relativity. *Class. Quant. Grav.*, 21:4417–4429, 2004.

[224] Leonardo Balart and Elias C. Vagenas. Regular black holes with a nonlinear electrodynamics source. *Phys. Rev. D*, 90(12):124045, 2014.

[225] H. A. Borges, I. P. R. Baranov, F. C. Sobrinho, and S. Carneiro. Remnant loop quantum black holes. *Class. Quant. Grav.*, 41(5):05LT01, 2024.

[226] Sam R. Dolan, Marco A. A. de Paula, Luiz C. S. Leite, and Luís C. B. Crispino. Superradiant instability of a charged regular black hole. *Phys. Rev. D*, 109(12):124037, 2024.

[227] Marco A. A. de Paula, Luiz C. S. Leite, and Luís C. B. Crispino. Sufficient conditions for unbounded superradiance in black hole spacetimes sourced by nonlinear electrodynamics. 1 2025.

[228] Shahar Hod. Stability of the extremal Reissner-Nordstroem black hole to charged scalar perturbations. *Phys. Lett. B*, 713:505–508, 2012.

[229] Shahar Hod. Stability of highly-charged Reissner-Nordström black holes to charged scalar perturbations. *Phys. Rev. D*, 91(4):044047, 2015.

[230] W. Kinnersley. Recent progress in exact solutions. In *7th International Conference on Gravitation and Relativity*, pages 109–135, 1975.

[231] Pedro V. P. Cunha, Carlos A. R. Herdeiro, and Eugen Radu. Isolated black holes without $\mathbb{Z}_2$ isometry. *Phys. Rev. D*, 98(10):104060, 2018.

[232] Arne Grenzebach, Volker Perlick, and Claus Lämmerzahl. Photon Regions and Shadows of Kerr-Newman-NUT Black Holes with a Cosmological Constant. *Phys. Rev. D*, 89(12):124004, 2014.